HUMBOLDT-UNIVERSITÄT ZU BERLIN

MASTERARBEIT

Ab initio investigation of first-order Raman scattering in gallium oxide

Autor:
Rouven Alexander Koch

Betreuer:
Dr. Pasquale Pavone

Erster Gutachter:
Prof. Dr. Dr. h.c. Claudia Draxl

Zweiter Gutachter:
Prof. Dr. Henning Riechert

Zur Erlangung des akademischen Grades:
Master of Science (M.Sc.)

Mathematisch-Naturwissenschaftliche Fakultät
Institut für Physik

8. Oktober 2019

Selbstständigkeitserklärung

Ich erkläre ausdrücklich, dass es sich bei der von mir eingereichten schriftlichen Arbeit mit dem Titel "*Ab initio* investigation of first-order Raman scattering in gallium oxide" um eine von mir selbstständig verfasste Arbeit handelt und diese nicht bereits für andere Prüfungen eingereicht wurde.

Ich erkläre ausdrücklich, dass ich sämtliche in der oben genannten Arbeit verwendeten fremden Quellen, auch aus dem Internet (einschlielich Tabellen, Grafiken u. Ä.), als solche kenntlich gemacht habe. Insbesondere bestätige ich, dass ich ausnahmslos sowohl bei wörtlich übernommenen Aussagen bzw. unverändert übernommenen Tabellen, Grafiken u. Ä. (Zitaten) als auch bei in eigenen Worten wiedergegebenen Aussagen bzw. von mir abgewandelten Tabellen, Grafiken u. Ä. anderer Autorinnen und Autoren (Paraphrasen) die Quelle angegeben habe.

Unterschrift: _____

Datum: _____

Acknowledgements

First of all, I want to mention how grateful I am for so many people, who supported me on this journey over the last year. I also want to apologize beforehand for the people I will forget to mention in this acknowledgements.

I want to start thanking Prof. Dr. Dr. Claudia Draxl, who gave me the opportunity to write my thesis in her research group, supported me along the road with helpful advice, and being the first advisor of my thesis. In that sense, I would also like to acknowledge the effort of Prof. Dr. Henning Riechert for taking the time to be the second advisor of this work.

By far the biggest gratitude I have to give Dr. Pasquale Pavone, who was not only my direct supervisor but also an inspiring mentor, who taught me much more than just physics. Although we had to spend long days.. and sometimes evenings up to early nights in the office to finish this thesis, we always found the time for nice conservations and having some fun. He invested more time in me and my work than I could ever have imagined.

Another group member I want to mention here is Dimitrii Nabok, who was always willing to help me with a smile on his face, no matter how stupid my question was. He also gave me good advice and suggestions, that helped me a lot to finish this work.

Furthermore, I thank Dr. Fabio Caruso and Olga Turkina for reading parts of this thesis and giving me helpful suggestions for improvements.

I also want to thank Axel Hübner for having good times and nice conversations in our office and for taking a huge amount of coffee breaks with me, which so often saved my day.

I would like to extend my gratitude to my family, especially my parents and my sister. They supported me during my whole studies, no matter if success or failure. Without their advice and support, I would have been very lost several times.

I would like to close this part by acknowledging the contributions of the people I spent most of my free time in Berlin with. Raymond Amador for being one of the best friends someone could ever imagine. I think no more words are needed at this point. I am also grateful to Lisa Koll, Sebastian Bannmann, Matthias Runge, and Tanja Holstein, for making me feel part of their group from my first day of university and making the big foreign Berlin to my new home. Finally, Marcio Merkel, for the mutual motivation in so many areas of life and being a person I can always count on. In the end, many more people have influenced me in this part of my life, but I think for the sake of shortness I will hereby end these acknowledgements.

Contents

0. Introduction

Transparent conducting oxides (TCOs) exhibit promising properties, which can be beneficially used in order to develop novel devices and technologies [1, 2]. Examples for key devices made of TCOs are transparent thin-film transistors and transparent field-effect transistors, which have the possibility to replace amorphous silicon transistors in several applications, due to their ten times higher charge-carrier density [3]. Furthermore, TCOs can be used for the fabrication of transparent displays [4, 5]. Several other flexible devices are also conceivable, which have the potential to affect and improve the everyday life of future generations [6, 7]. In this context, the improvement of performance, reproduction ability, and cost reduction of these materials is necessary and still under investigation [1].

Among other TCOs, gallium oxide (Ga_2O_3) is a very promising material. Recently, Ga_2O_3 crystals with a high degree of purity became available [8]. One of these crystals is exemplarily shown in Figure 1. The characteristic properties, which make Ga_2O_3 a promising candidate for several applications are its wide bandgap of about 4.8-4.9 eV [9, 10], the good transparency from the infrared to the ultraviolet range [9], a high charge-carrier mobility [10, 11], as well as a high breakdown field of around 8 MV/cm [11]. These properties suggest that Ga_2O_3 can play a big role in the development of future technology. In fact, the possibility of applications has already been shown in several studies, as, *e.g.*, in the application as light-emitting diodes [12], transparent field-effect transistors [10, 13], MOSFETs [14, 15, 16], and Shottky barrier diodes [17, 18]. Aside from this wide range of already shown applications, the expectations are high for the usage in (high-voltage) power devices [19]. Especially the low costs and low energy consumption are a big advantage over nowadays established wide-gap semiconductors or insulators as SiC, GaN, and diamond [11].

Despite all these successful examples for many kinds of applications of Ga_2O_3,

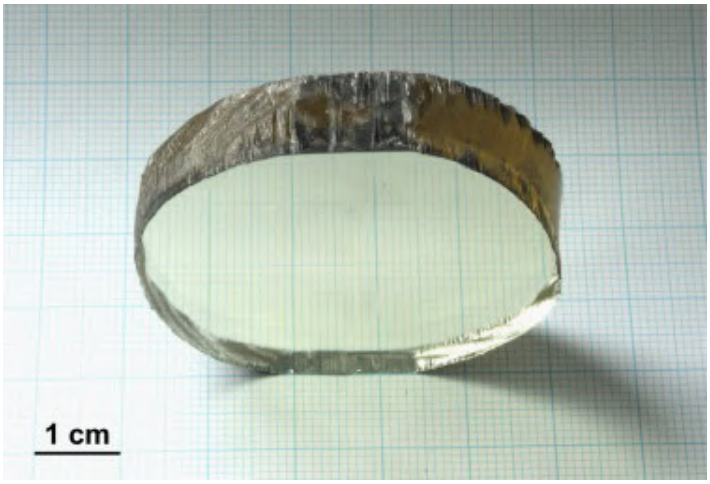

FIGURE 1: Czochralski-grown β-Ga_2O_3 crystal with a diameter of about 5 cm [8]. It also illustrates the transparency of Ga_2O_3 in the visible spectrum.

there are still several open questions about its fundamental properties. The preparation of high-quality single crystals and thin films as well as the pronounced polymorphism are among the most important experimental problems [20]. More precisely, five different phases of Ga_2O_3 have been discovered so far [20, 21]. One of these five phases, namely the β phase, is thermodynamically stable and, therefore, in the center of our investigation. Under sufficiently high pressure (of about 20 GPa), a transition from the stable β to the metastable α phase was reported in Ref. [22]. The metastable phases of Ga_2O_3 did not receive the same attention as the stable β phase, although they are very important in the growth and further processing. In particular, the corundum-like α phase is attractive for technological reasons, can be characterized at ambient pressure and temperature, and its optoelectronic properties may differ drastically from those of the β phase [22, 23, 24]. On the theoretical side, first-principles investigations for this material are challenging, in particular concerning the determination of accurate optical properties and other excitations [25].

A fundamental tool for the characterization of these materials is Raman spectroscopy, which makes use of inelastic light scattering inside the crystal in order to obtain insights in the material properties. Moreover, the extreme sensitivity of Raman scattering facilitates the identification of defects, impurities, and crystal arrangement and gives insights into the polymorphism. An experimental Raman spectrum of Ga_2O_3 nanorods is shown in Figure 2 [26]. In general, polarized spectra enable a direct analysis of the vibrational properties [27]. Besides, Raman scattering can also yield insight into optical excitations and electron-phonon coupling [27].

A full understanding of all Raman-scattering mechanisms in Ga_2O_3 requires a strong interplay between experiment and theory. Only a few works are available in the literature which present measurements of the Raman spectra for β [28, 29, 30] and α [23, 31] phases of Ga_2O_3. Theoretical calculations of the Raman tensors are, to the best of our knowledge, only performed for the β phase [28]. Therefore, it is our purpose to calculate Raman tensors for both phases to fill the gap of missing theoretical

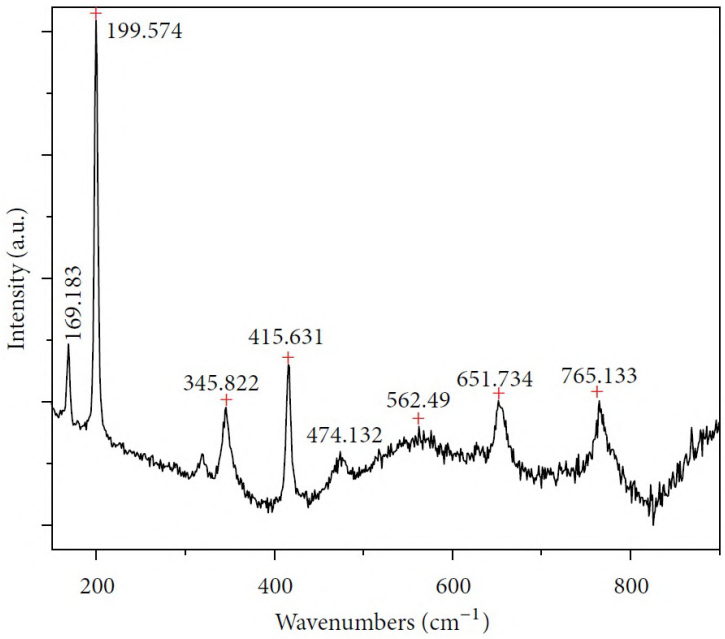

FIGURE 2: An experimental Raman spectrum of β-Ga_2O_3 nanorods [26].

values, to obtain a better understanding of the fundamental properties, and to support the development of Ga_2O_3 for new applications and devices.

More precisely, our goal is the calculation of first-order Raman tensors for the β and α phase of Ga_2O_3, by using the *ab initio* methodology implemented in the software package `exciting` [32]. The knowledge of these tensors allows us to compute Raman spectra in any polarization configuration. Several other properties, which are necessary for the calculation of Raman tensors and spectra, are also investigated. This includes ground-state properties, such as the equilibrium crystal structure, lattice dynamics, as well as properties related to the optical excitations of the crystal, like the frequency-dependent dielectric functions.

This thesis is organized as follows. First, in Chapter 1 we give a short introduction of the Raman scattering including a theoretical background. In Chapter 2, we outline the theoretical concepts which are used in this thesis. This is followed in Chapter 3 by an introduction of the computational methodology underlying our *ab initio* calculations. In Chapter 4, we present the results of the investigated properties of β- and α-Ga_2O_3. Finally, this thesis is closed in Chapter 5 by presenting our conclusions and by giving an outlook on further topics of investigation.

1. Raman Scattering

The first chapter of this thesis focuses on the framework of Raman scattering, which is one of the fundamental tools for the investigation of solid-state materials. After a short general and historical introduction of the Raman effect in Section 1.1, the macroscopic and microscopic theory are summarized in Sections 1.2 and 1.3, respectively. Finally, the role of the dielectric function for Raman scattering is highlighted in Section 1.4.

1.1 Introduction to the Raman effect

Light scattering spectroscopy, either elastic or inelastic, gives insights in several properties of a crystal. When a light beam, *e.g.*, a laser in a laboratory, travels through a crystal, most photons are absorbed or transmitted, depending on the reflectivity and refraction properties of the specific crystal. Additionally, inhomogeneities can cause scatterings of photons inside the crystal. These inhomogeneities can be classified into dynamical or static ones, such as defects. In this work, we focus on the dynamical case, which can be related to collective time-dependent atomic vibrations. The effect of inelastic scattering of light due to coherent atomic vibrations, called *phonons*, is named after its discoverer *Chandrasekhara Venkata Raman*, who won the Nobel prize for this topic in 1930. These inelastic light scattering events inside the crystal change the energy of the incident electromagnetic wave. Nowadays, *Raman spectroscopy* is one of the mostly used tools to investigate lattice and electronic-structure properties of semiconductors and insulators [33]. A schematic representation of a Raman scattering process is depicted in Figure 1.1.

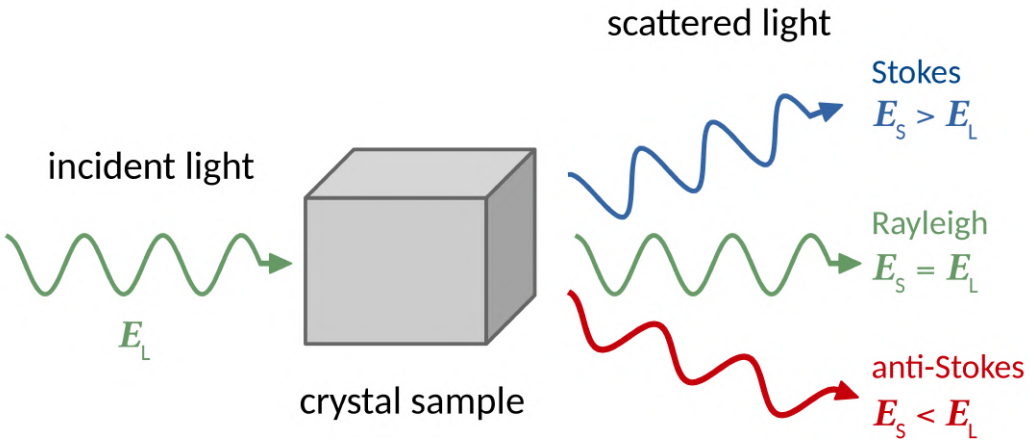

FIGURE 1.1: Schematic illustration of photon scattering on a crystal sample. Three different effects are shown (Rayleigh, Stokes, and anti-Stokes). Absorption effects are neglected.

A change of the wavelength is induced due to interactions with phonons and, consequently, the light energy is either increased (decreased) by absorbing (emitting) a phonon. In that case, one refers to a *Stokes* (*anti-Stokes*) shift, which is in general referred as *Raman effect* [33]. This macroscopic point of view is described in detail in the next section.

Measuring the difference of incident, ω_L, and scattered, ω_S, light frequencies, yields to the observation of peaks in the intensity in the vicinity of phonon frequencies ω_{ph}. The *Raman-scattering efficiency*, S, can simply be written in terms of the differential cross-section in a scattering volume V_S as follows [33]

$$S = \frac{1}{V_S}\frac{d\sigma}{d\Omega}\,, \tag{1.1.1}$$

and can be derived by different approaches. The scattering efficiency can be directly measured by Raman spectroscopy and characterizes the ratio between the scattered and incident electromagnetic waves, which crosses a specified area per defined time interval and angle. The connection to theoretical approaches, introducing the concept of *Raman tensors*, is presented in the next sections.

1.2 Macroscopic theory

This section is following the derivation and partly the notation of Ref. [33] and deals with the theory of Raman scattering from the macroscopic perspective, *i.e.*, how an electromagnetic wave is affected by (dynamical) inhomogeneities of a crystal. The origin of dynamical inhomogeneities is the finite temperature, which causes thermally-excited lattice vibrations. These quasi-particle-like excitations are called *phonons*. For the derivation of the scattering efficiency, and, therefore, of the Raman tensors, we assume the electromagnetic field to be a sinusoidal plane wave, which has the

form

$$\boldsymbol{E}(\boldsymbol{r},t) = \widetilde{\boldsymbol{E}}(\boldsymbol{k}_{\mathrm{L}},\omega_{\mathrm{L}})\cos(\boldsymbol{k}_{\mathrm{L}}\cdot\boldsymbol{r}-\omega_{\mathrm{L}}t)\ , \tag{1.2.1}$$

with frequency ω_{L}, wave vector $\boldsymbol{k}_{\mathrm{L}}$, and amplitude $\widetilde{\boldsymbol{E}}(\boldsymbol{k}_{\mathrm{L}},\omega_{\mathrm{L}})$. This electromagnetic field generates a sinusoidal polarization with the same frequency and wave vector

$$\boldsymbol{P}(\boldsymbol{r},t) = \widetilde{\boldsymbol{P}}(\boldsymbol{k}_{\mathrm{L}},\omega_{\mathrm{L}})\cos(\boldsymbol{k}_{\mathrm{L}}\cdot\boldsymbol{r}-\omega_{\mathrm{L}}t)\ , \tag{1.2.2}$$

where the polarization amplitude is defined as

$$\widetilde{\boldsymbol{P}}(\boldsymbol{k}_{\mathrm{L}},\omega_{\mathrm{L}}) = \boldsymbol{\chi}(\boldsymbol{k}_{\mathrm{L}},\omega_{\mathrm{L}})\cdot\widetilde{\boldsymbol{E}}(\boldsymbol{k}_{\mathrm{L}},\omega_{\mathrm{L}})\ . \tag{1.2.3}$$

The $\boldsymbol{\chi}$ appearing in Eq. (1.2.3) is the *electric susceptibility*, which is a complex second-rank tensor and is affected by the phonons or, in other words, by the time-dependent atomic displacements. To compare theoretical and experimental results, the *dielectric tensor* $\boldsymbol{\epsilon}(\boldsymbol{k},\omega)$ is introduced. The dielectric tensor is, as well as $\boldsymbol{\chi}$, a complex second-rank tensor and is connected to the susceptibility by the following relation (see Section 6.1 in Ref. [33])

$$\boldsymbol{\epsilon}(\boldsymbol{k},\omega) = 1 + 4\pi\,\boldsymbol{\chi}(\boldsymbol{k},\omega)\ . \tag{1.2.4}$$

In a simple continuous model,[1] the phonon displacement can be written as

$$\boldsymbol{u}(\boldsymbol{r},t) = \boldsymbol{w}(\boldsymbol{q},\omega_{\mathrm{ph}})\cos(\boldsymbol{q}\cdot\boldsymbol{r}-\omega_{\mathrm{ph}}t)\ , \tag{1.2.5}$$

where $\boldsymbol{q}$ is the wave vector, $\boldsymbol{w}(\boldsymbol{q},\omega_{\mathrm{ph}})$ the phonon-mode amplitude, and ω_{ph} the corresponding phonon frequency. Within the *quasi-static / adiabatic approximation*, which relies on the fact that the electronic frequencies of $\boldsymbol{\chi}$ are much larger than the phonon frequencies, the susceptibility can be expanded in terms of the amplitude $\boldsymbol{w}(\boldsymbol{q},\omega_{\mathrm{ph}})$. The expansion of $\boldsymbol{\chi}$ around the equilibrium configuration, $\boldsymbol{w}=0$, labeled with the index 0, can then be written as

$$\boldsymbol{\chi}(\boldsymbol{k}_{\mathrm{L}},\omega_{\mathrm{L}},\boldsymbol{w}) \approx \boldsymbol{\chi}_0(\boldsymbol{k}_{\mathrm{L}},\omega_{\mathrm{L}}) + \left.\frac{\partial\boldsymbol{\chi}}{\partial\boldsymbol{w}}\right|_0\cdot\boldsymbol{w}(\boldsymbol{q},\omega_{\mathrm{ph}})\ , \tag{1.2.6}$$

using the definition

$$\left.\frac{\partial\boldsymbol{\chi}}{\partial\boldsymbol{w}}\right|_0 = \int d\boldsymbol{r}\ \nabla\boldsymbol{\chi}|_0\cos(\boldsymbol{r}\cdot\boldsymbol{q}-\omega t)\ . \tag{1.2.7}$$

[1] For the sake of simplicity, we consider here a model including only one phonon mode in the continuous-media approximation. This framework, however, is easily extendible to realistic systems as shown in the next sections and chapters of this thesis.

This approximation is reasonable if the wavelength of the incident laser is much larger than the lattice constant and, therefore, if the phonon wave vector can be assumed to be negligible. Inserting the expansion in Eq. (1.2.6) into the general expression for the polarization, Eq. (1.2.2), leads to

$$\begin{aligned} \boldsymbol{P}(\boldsymbol{r},t,\boldsymbol{w}) &= \left[\,\boldsymbol{\chi}_0(\boldsymbol{k}_{\mathrm{L}},\omega_{\mathrm{L}})\cdot\widetilde{\boldsymbol{E}}(\boldsymbol{k}_{\mathrm{L}},\omega_{\mathrm{L}})\cos(\boldsymbol{k}_{\mathrm{L}}\cdot\boldsymbol{r}-\omega_{\mathrm{L}}t)\,\right] \\ &\quad+\left[\left.\frac{\partial\boldsymbol{\chi}}{\partial\boldsymbol{w}}\right|_0\cdot\boldsymbol{w}(\boldsymbol{q},\omega_{\mathrm{ph}})\cdot\widetilde{\boldsymbol{E}}(\boldsymbol{k}_{\mathrm{L}},\omega_{\mathrm{L}})\cos(\boldsymbol{k}_{\mathrm{L}}\cdot\boldsymbol{r}-\omega_{\mathrm{L}}t)\right] \\ &= \boldsymbol{P}_0(\boldsymbol{r},t)+\boldsymbol{P}_{\mathrm{ind}}(\boldsymbol{r},t,\boldsymbol{w})\;, \end{aligned} \tag{1.2.8}$$

where the polarization $\boldsymbol{P}$ is separated into an unperturbed part $\boldsymbol{P}_0$ and a phonon-induced part $\boldsymbol{P}_{\mathrm{ind}}$. Another way of generating *polarization waves* in polar crystals is discussed in more detail in Section 2.3.2.

The Raman-scattering efficiency, $S(\omega_{\mathrm{S}})$, can be evaluated as follows. Generally, the intensity of the scattered light, I_{S}, depends on the phonon-induced polarization $\boldsymbol{P}_{\mathrm{ind}}$ as well as on the polarization of the incident, $\boldsymbol{e}_{\mathrm{L}}$, and scattered light, $\boldsymbol{e}_{\mathrm{S}}$, by the relation

$$I_{\mathrm{S}} \;\propto\; \left|\boldsymbol{e}_{\mathrm{L}}\cdot\boldsymbol{P}_{\mathrm{ind}}\cdot\boldsymbol{e}_{\mathrm{S}}\right|^2 \;\propto\; \left|\boldsymbol{e}_{\mathrm{L}}\cdot\left.\frac{\partial\boldsymbol{\chi}}{\partial\boldsymbol{w}}\right|_0\cdot\boldsymbol{w}(\boldsymbol{q},\omega_{\mathrm{ph}})\cdot\boldsymbol{e}_{\mathrm{S}}\right|^2 \;\propto\; \left|\boldsymbol{e}_{\mathrm{L}}\cdot\mathscr{B}\cdot\boldsymbol{e}_{\mathrm{S}}\right|^2 \tag{1.2.9}$$

where, in the linear regime defined by Eq. (1.2.6), the Raman tensor, $\mathscr{B}$, has been introduced as

$$\mathscr{B} = \left.\frac{\partial\boldsymbol{\chi}}{\partial\boldsymbol{w}}\right|_0\cdot\widetilde{\boldsymbol{w}} \;=\; \frac{1}{4\pi}\left.\frac{\partial\boldsymbol{\epsilon}}{\partial\boldsymbol{w}}\right|_0\cdot\widetilde{\boldsymbol{w}}\;, \tag{1.2.10}$$

using the notation $\widetilde{\boldsymbol{w}} \equiv \boldsymbol{w}(\boldsymbol{q},\omega_{\mathrm{ph}})/|\boldsymbol{w}(\boldsymbol{q},\omega_{\mathrm{ph}})|$.

The general expression of the Raman efficiency in Eq. (1.1.1) can now be rewritten in terms of the variation of the dielectric function at a certain laser frequency ω_{L}. For a transition between an initial state $|i\rangle$, describing the system before the interaction with the incident light wave, and a final state $|f\rangle$, describing the system after the scattering, S reads [34]

$$S_{i\to f}(\omega_{\mathrm{S}}) = \frac{V_{\mathrm{S}}\,\omega_{\mathrm{L}}\,\omega_{\mathrm{S}}^3}{(4\pi)^2c^4}\;\left|\boldsymbol{e}_{\mathrm{L}}\cdot\left[\delta\boldsymbol{\epsilon}_{i\to f}\right]_{\omega_{\mathrm{S}}}\cdot\boldsymbol{e}_{\mathrm{S}}\right|^2\;, \tag{1.2.11}$$

where ω_{S} is the frequency of the scattered light. A quantum-mechanical approach for the transition matrix element $\delta\boldsymbol{\epsilon}_{i\to f} = \langle f|\,\delta\boldsymbol{\epsilon}_{\omega_{\mathrm{L}}}|i\rangle$ is discussed in detail in the next section.

1.3 Formal microscopic theory

This section outlines the formal microscopic way to calculate the matrix element $\delta\boldsymbol{\epsilon}_{i\to f}$, introduced in the previous section. The interaction of photons with lattice vibrations

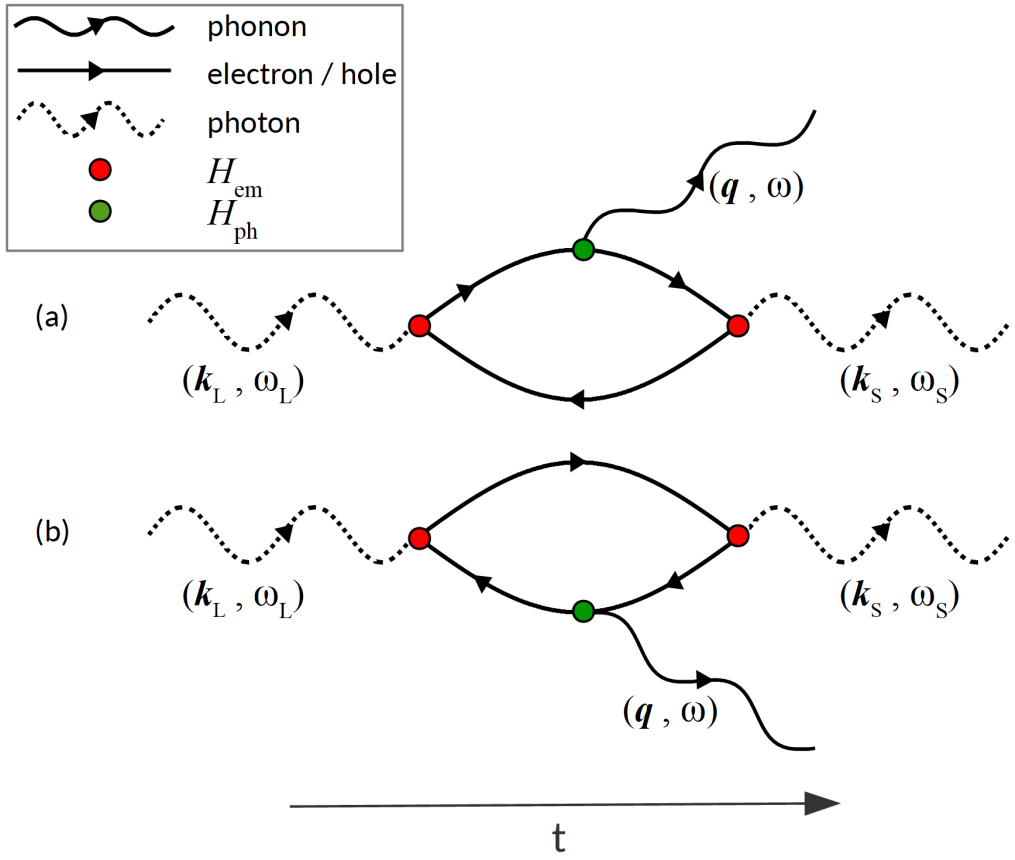

FIGURE 1.2: Diagrammatic representation of first-order Raman scattering (3rd order perturbation theory) for the electron-phonon (a) and hole-phonon contribution (b). Two different Hamiltonians, H_{em} for the photon-eh interaction and H_{ph} for the eh-phonon interaction, are included.

is mediated by excited electron-hole (eh) pairs, which are in virtual energy states in the case of *off-resonant* Raman scattering.[2]

The Raman tensor introduced in Eq. (1.2.10) describes the relation between incident and scattered photons, or electric fields, and is physically spoken the susceptibility for the transition [33]. Considering only off-resonant laser energies for phonon scattering, the Raman tensor is symmetric and real [27], as it is the case for the systems studied in this work. Only in the case of resonance or near-resonance Raman scattering, antisymmetric elements appear. Furthermore, the induced excitations in the solid yield to a change in the electric polarizability.

In the microscopic theory of *first-order* Raman scattering, for which only one phonon scattering event is involved, the transition between state $|i\rangle$ and $|f\rangle$ can be split up into three different matrix elements. First, the creation of an eh pair induced by the incident photons; second, an interaction of an electron or hole with one phonon;

[2] In the case of Raman scattering, the off-resonant condition implies that only virtual electronic states are excited, *i.e.*, that the exciting energies are below the fundamental gap for semiconductors and insulators.

and, finally, the recombination of the eh pair and the along going transmission of a Stokes shifted photon.[3] Therefore, we have to deal with a problem including *third-order perturbation theory*,[4] whose process can be described in the formalism of Feynman diagrams, as shown in Figure 1.2. In particular, Figure 1.2.a is the diagrammatic representation of the electron-phonon and Figure 1.2.b the representation of the hole-phonon interaction, respectively. Two different Hamiltonians, H_{em} for the photon-eh interaction and H_{ph} for the eh-phonon interaction, are involved. The incident photon possesses the momentum $\boldsymbol{k}_{\text{L}}$ and frequency ω_{L}, whereas the scattered photons have the momentum $\boldsymbol{k}_{\text{S}}$ and frequency ω_{S}. Moreover, energy conservation requires $\omega_{\text{S}}(\boldsymbol{k}_{\text{S}}) = \omega_{\text{L}}(\boldsymbol{k}_{\text{L}}) \pm \omega(\boldsymbol{q})$, where $\omega(\boldsymbol{q})$ defines the dispersion of the phonon. Concerning momentum conservation, $\boldsymbol{k}_{\text{S}} = \boldsymbol{k}_{\text{L}} + \mathbf{q}$, the involved phonon must have a momentum of $\boldsymbol{q} \approx 0$ in the case of a single phonon scattering process. The annihilation of this phonon causes an energy increase of the incident photon, for the Stokes process, which is called from now on *Raman shift*.

The transition matrix element can also be written, for the electron-phonon or hole-phonon interaction, as [35]

$$\langle f | \, \delta\boldsymbol{\epsilon}_{\omega_{\text{L}}} \, | i \rangle \propto \sum_{s_1, s_2} \frac{\langle f | \hat{H}_{\text{em}} | s_2 \rangle \, \langle s_2 | \hat{H}_{\text{ph}} | s_1 \rangle \, \langle s_1 | \hat{H}_{\text{em}} | i \rangle}{(\hbar\omega_{\text{L}} - E_2 + \mathrm{i}\,\Gamma_2/2)\,(\hbar\omega_{\text{L}} - E_1 + \mathrm{i}\,\Gamma_1/2)}\,, \tag{1.3.1}$$

where s_i $(i = 1, 2)$ is an intermediate vibrational state with decay rate Γ_i and energy E_i.

An important remark at this point is, that this microscopic approach is not the way how the calculations of the Raman tensors are performed in this thesis and implemented in the software package `exciting` [32]. It illustrates, however, the microscopic physical processes in the crystal. The next section works out a methodology based on the calculation of $\mathscr{B}$ in terms of the gradients $\partial\boldsymbol{\epsilon}/\partial\boldsymbol{Q}$. This second approach is the one used in this thesis.

1.4 The dielectric function in Raman scattering

This section follows the derivation of Ref. [36] for the calculation of the Raman tensors in terms of derivatives of the dielectric function. A quantum-mechanical approach for the scattering efficiency S, which includes *Fermi's golden rule* for the transition between the initial state $|i\rangle$ and the final state $|f\rangle$, is given by Eq. (1.2.11). In particular, the

[3] We focus only on the Stokes process and set aside the anti-Stokes shift, which is, nevertheless, very similar to the Stokes process.

[4] Assuming the electron-radiation Hamiltonian, H_{em}, and electron-phonon Hamiltonian, H_{ph}, to be small, both interactions can then be treated as perturbations of the unperturbed system. The three vertices lead to a perturbation process of the third order [27].

transition matrix element $\delta\boldsymbol{\epsilon}_{i\to f}$ for a chosen ω_{S} has the following form

$$[\delta\boldsymbol{\epsilon}_{i\to f}]_{\omega_{\mathrm{S}}} = \langle f|\,\delta\boldsymbol{\epsilon}(\omega_{\mathrm{L}},\omega_{\mathrm{S}})\,|i\rangle = \langle a\sigma|\,\delta\boldsymbol{\epsilon}(\omega_{\mathrm{L}},\omega_{\mathrm{S}})\,|a\rho\rangle\,, \tag{1.4.1}$$

where we made use of the decomposition of the states $|i\rangle$ and $|f\rangle$ into electronic, $|a\rangle_{\mathrm{el}}$, and vibrational, $|\rho\rangle_{\mathrm{ph}}$ and $|\sigma\rangle_{\mathrm{ph}}$, contributions. In this case, the electronic state $|a\rangle_{\mathrm{el}}$ remains unchanged, because we are still using the adiabatic approximation.

The dielectric tensor $\boldsymbol{\epsilon}(\omega_{\mathrm{L}},\omega_{\mathrm{S}})\equiv\boldsymbol{\epsilon}$ can be expanded in terms of the phonon normal coordinates $Q_{q\mu}\equiv Q_{\xi}$, where $\xi\equiv(\boldsymbol{q},\mu)$ with the index $\mu=1,...,3N_{\mathrm{atom}}$ labeling the phonon frequencies at a given wave vector $\boldsymbol{q}$. For a specific laser frequency ω_{L} the expansion of $\boldsymbol{\epsilon}$ up to order n can be written as

$$\boldsymbol{\epsilon}(\{Q_{\xi}\}) = \sum_{n=1}\frac{1}{n!}\sum_{\xi_1}\cdots\sum_{\xi_n}\frac{\partial^n\boldsymbol{\epsilon}}{\partial Q_{\xi_1}\cdots\partial Q_{\xi_n}}\bigg|_0 Q_{\xi_1}\cdots Q_{\xi_n}\,. \tag{1.4.2}$$

Equation (1.4.2) can be inserted into Eq. (1.4.1) which leads to

$$[\delta\boldsymbol{\epsilon}_{i\to f}]_{\omega_{\mathrm{S}}} = \sum_{n=1}\frac{1}{n!}\sum_{\xi_1}\cdots\sum_{\xi_n}\langle f|\frac{\partial^n\boldsymbol{\epsilon}}{\partial Q_{\xi_1}\cdots\partial Q_{\xi_n}}\hat{Q}_{\xi_1}\cdots\hat{Q}_{\xi_n}|i\rangle_{\omega_{\mathrm{S}}}\,. \tag{1.4.3}$$

At this point, a separation of the electronic and vibrational contributions of the final and initial state to $|a\rho\rangle$ and $|a\sigma\rangle$ is used. This approximation simplifies Eq. (1.4.3) to

$$\begin{aligned}
[\delta\boldsymbol{\epsilon}_{a\rho\to a\sigma}]_{\omega_{\mathrm{S}}} &= \sum_{n=1}\frac{1}{n!}\sum_{\xi_1}\cdots\sum_{\xi_n}\langle a\,\sigma|\frac{\partial^n\boldsymbol{\epsilon}}{\partial Q_{\xi_1}\cdots\partial Q_{\xi_n}}\hat{Q}_{\xi_1}\cdots\hat{Q}_{\xi_n}|a\,\rho\rangle \\
&\propto \sum_{n=1}\frac{1}{n!}\sum_{\xi_1}\cdots\sum_{\xi_n}\langle a|\frac{\partial^n\boldsymbol{\epsilon}}{\partial Q_{\xi_1}\cdots\partial Q_{\xi_n}}|a\rangle_{\mathrm{el}}\cdot\langle\sigma|\hat{Q}_{\xi_1}\cdots\hat{Q}_{\xi_n}|\rho\rangle_{\mathrm{ph}} \\
&\propto \sum_{n=1}\frac{1}{n!}\sum_{\xi_1}\cdots\sum_{\xi_n}\frac{\partial^n\boldsymbol{\epsilon}}{\partial Q_{\xi_1}\cdots\partial Q_{\xi_n}}\bigg|_0\cdot\langle\sigma|\hat{Q}_{\xi_1}\cdots\hat{Q}_{\xi_n}|\rho\rangle_{\mathrm{ph}}\,.
\end{aligned} \tag{1.4.4}$$

The order of a Raman-scattering process is defined by the number of included phonons.

In this thesis, only first-order Raman scattering is considered. This means that Γ point phonons with momentum $\boldsymbol{q}=0$ have to be taken into account. The general expression in Eq. (1.4.4) simplifies in the first-order to

$$[\delta\boldsymbol{\epsilon}_{a\rho\to a\sigma}]^{(1)}_{\omega_{\mathrm{S}}} = \frac{\partial\boldsymbol{\epsilon}}{\partial Q_{\mu}}\langle\sigma|\hat{Q}_{\mu}\,|\rho\rangle + \frac{\partial^2\boldsymbol{\epsilon}}{2\,\partial Q_{\mu}^2}\langle\sigma|\hat{Q}_{\mu}^2\,|\rho\rangle + \mathscr{O}(\hat{Q}_{\mu}^3)\,, \tag{1.4.5}$$

where $\xi=(\boldsymbol{q}=0,\mu)\equiv\mu$ and $\hat{Q}_{\mu}$ is the normal coordinate of the μ-th phonon at Γ. Finally, the total first-order Raman scattering efficiency for a specific ω_{S}, at a certain temperature T, and laser energy ω_{L} is expressed as [34]

$$S(\omega_{\mathrm{S}}) = \frac{N_{\mathrm{cell}}\,\Omega}{(4\pi)^2c^4}\cdot\frac{\omega_{\mathrm{L}}\,\omega_{\mathrm{S}}^3\,\sum_{\mu}\exp\left(-E_{\mu}/k_{\mathrm{B}}T\right)\,\sum_{\sigma}\left|\,[\delta\boldsymbol{\epsilon}_{a\rho\to a\sigma}]^{(1)}_{\omega_{\mathrm{S}}}\,\right|^2}{\sum_{\mu}\exp\left(-E_{\mu}/k_{\mathrm{B}}T\right)}\,, \tag{1.4.6}$$

where Ω is the unit cell volume, N_{cell} the number of considered cells, k_{B} the Boltzmann constant, the first sum runs over all phonon modes μ and the second sum runs over all final vibrational states $|\sigma\rangle_{\text{ph}}$.

2. Theoretical Background

In this chapter, we give a short description of the theoretical aspects on which this thesis is based. The starting point is the quantum-mechanical treatment of the system of nuclei and electrons in a solid, which is discussed in Section 2.1. After that, we focus on the electronic system for a fixed nuclear configuration in Section 2.2, underlying the role played by the ground-state electron density. In Section 2.3, we come back to the nuclear system regarding lattice vibrations and the peculiar properties of polar crystals. Finally, the state-of-the-art methodology for the calculation of optical properties is outlined in Section 2.4.

2.1 Total Hamiltonian and adiabatic approximation

This section follows the guideline of Chapter 3 of Ref. [37] and partially adopts its notation.[1] First of all, the total stationary Schrödinger equation for a solid-state many-body system, consisting of N_e electrons and N_n nuclei, reads

$$\hat{H}(\mathscr{r},\mathscr{R})\,\Psi(\mathscr{r},\mathscr{R}) = \mathscr{E}\,\Psi(\mathscr{r},\mathscr{R})\ , \tag{2.1.1}$$

where $\mathscr{E}$ is the energy of the system, the total wave function is indicated as $\Psi(\mathscr{r},\mathscr{R})$, $\mathscr{r} = \{\boldsymbol{r}_i\,;\, i = 1,...,N_e\}$ and $\mathscr{R} = \{\boldsymbol{R}_I\,;\, I = 1,...,N_n\}$ are the configurations of electrons

[1] In contrast to Ref. [37], we use from now on atomic units, for which we set $e^2 = m_e = \hbar = 1$.

and nuclei, respectively. Furthermore, the full Hamiltonian reads

$$\begin{aligned}\hat{H}(\mathscr{r},\mathscr{R}) = &-\sum_{I}^{N_n}\frac{\nabla_{\boldsymbol{R}_I}^2}{2M_I} - \sum_{i}^{N_e}\frac{\nabla_{\boldsymbol{r}_i}^2}{2} + \frac{1}{2}\sum_{I<J} v_{n\text{-}n}(\boldsymbol{R}_J - \boldsymbol{R}_I) \\ &+ \frac{1}{2}\sum_{i<j} v_{e\text{-}e}(\boldsymbol{r}_j - \boldsymbol{r}_i) + \sum_{i,I} v_{n\text{-}e}(\boldsymbol{R}_I - \boldsymbol{r}_i) \\ = &\hat{T}_n(\mathscr{R}) + \hat{T}_e(\mathscr{r}) + \hat{V}_{n\text{-}n}(\mathscr{R}) + \hat{V}_{e\text{-}e}(\mathscr{r}) + \hat{V}_{n\text{-}e}(\mathscr{r},\mathscr{R}) \,,\end{aligned} \tag{2.1.2}$$

where M_I is the mass of atom I. The total Hamiltonian consists of kinetic-energy ($\hat{T}$) and Coulomb-interaction ($\hat{V}$) operators of electrons and nuclei, specified with the indices e and n, respectively. In practice, Eq. (2.1.1) is not solvable since the number of atoms of a macroscopic solid is very huge, *i.e.*, in the order of 10^{23}. This is the reason why physicists are investigating and developing different approaches to handle the total electrons-nuclei system of a solid.

To simplify Eq. (2.1.1), the motion of electrons and nuclei can be decoupled. This widespread procedure is called *adiabatic* or *Born-Oppenheimer approximation* and is motivated by the perception that electrons adapt instantaneously and adiabatically to the motion of the nuclei. This approximation is justifiable by the large mass difference between electrons and nuclei, but only exact in the limit $M_I \to \infty$. Within the adiabatic approximation, the full wave function can be factorized as

$$\Psi(\mathscr{r},\mathscr{R}) = \phi(\mathscr{r};\mathscr{R})\,\Xi(\mathscr{R}) \,, \tag{2.1.3}$$

where $\phi(\mathscr{r};\mathscr{R})$ is the electronic wave function, which only has a parametric dependence on all nuclear positions $\mathscr{R}$, and $\Xi(\mathscr{R})$ defines the separated nuclear (or vibrational) wave function. The electronic and nuclear wave functions satisfy thus two different "effective" Schrödinger equations, which read

$$\left[\hat{T}_e(\mathscr{r}) + \hat{V}_{e\text{-}e}(\mathscr{r}) + \hat{V}_{n\text{-}e}(\mathscr{r};\mathscr{R})\right]\,\phi(\mathscr{r};\mathscr{R}) = E(\mathscr{R})\,\phi(\mathscr{r};\mathscr{R}) \tag{2.1.4}$$

for the electronic part, where $E(\mathscr{R})$ is the total electronic energy,[2] and

$$\left[\hat{T}_n(\mathscr{R}) + \hat{\mathscr{V}}(\mathscr{R})\right]\Xi(\mathscr{R}) = \mathscr{E}\,\Xi(\mathscr{R}) \tag{2.1.5}$$

for the nuclear contribution. Special attention deserves the adiabatic potential

$$\hat{\mathscr{V}}(\mathscr{R}) = \hat{V}_{n\text{-}n}(\mathscr{R}) + E(\mathscr{R}) \,, \tag{2.1.6}$$

which represents the connection between Eqs. (2.1.4) and (2.1.5). In the next section, we focus on the electronic problem at a given nuclear configuration.

[2] The operator $\hat{V}_{n\text{-}n}(\mathscr{R})$ is sometimes included in the electronic Hamiltonian. In this case, $E(\mathscr{R})$ coincides with the adiabatic potential $\hat{\mathscr{V}}(\mathscr{R})$.

2.2 Density-functional theory

In this section, we introduce an approach of handling the $N \equiv N_e$ electrons problem for a fixed nuclear configuration. Solving the full electrons Schrödinger equation, Eq. (2.1.4), is one of the main goals of solid-state physics. Unfortunately, it is only possible for small systems with a few degrees of freedom. In general, electronic systems are completely determined by the full electronic wave function, which has $3N$ degrees of freedom and becomes a very complex object for even a relative small number of particles. The approach given by the *density-functional theory* (DFT) relies on the reduction of the complexity of the main descriptor function. In this context, instead of the total electronic wave function, DFT uses the ground-state (GS) electron density $n_{\text{GS}}(\boldsymbol{r})$ as main quantity. This yields a function dependent on only 3 instead of $3N$ variables.

The mathematical basis of DFT was given in 1964 by Pierre Hohenberg and Walter Kohn, who demonstrated that every quantum-mechanical observable is determined by the ground-state density $n_{\text{GS}}(\boldsymbol{r})$ of the corresponding system alone [38]. In particular, the functional describing the GS total electronic energy $E_{\text{GS}}[n]$ can be written in dependence of the density as

$$E_{\text{GS}}[n] \equiv E[n] = T_0[n] + E_{\text{H}}[n] + E_{\text{ext}}[n] + E_{\text{xc}}[n] \,. \tag{2.2.1}$$

The first functional appearing in the expression of $E[n]$ is the kinetic-energy functional $T_0[n]$ of a non-interacting electrons system at density $n(\boldsymbol{r})$. The peculiarity of $T_0[n]$ is that it can be defined as expectation value of the kinetic-energy operator $\hat{T}_e$ in a state described by a Slater determinant (SD) of single-particle wave functions as $\langle \phi_{\text{SD}} | \hat{T}_e | \phi_{\text{SD}} \rangle$. The remaining functionals are the classical Hartree energy $E_{\text{H}}[n]$, which describes the repulsive Coulomb interaction between the electrons and is defined as

$$E_{\text{H}}[n] = \frac{1}{2} \int d\boldsymbol{r} \int d\boldsymbol{r}' \, \frac{n(\boldsymbol{r})\, n(\boldsymbol{r}')}{|\boldsymbol{r} - \boldsymbol{r}'|} \equiv \frac{1}{2} \int d\boldsymbol{r} \, v_{\text{H}}(\boldsymbol{r})\, n(\boldsymbol{r}) \,, \tag{2.2.2}$$

the external energy functional

$$E_{\text{ext}}[n] = \int d\boldsymbol{r} \, v(\boldsymbol{r})\, n(\boldsymbol{r}) \,, \tag{2.2.3}$$

which is in direct correspondence with the external potential, which in our case is defined as $v(\boldsymbol{r}) = \sum_I v_{n\text{-}e}(\boldsymbol{R}_I - \boldsymbol{r})$, and, finally, the so-called exchange-correlation energy $E_{\text{xc}}[n]$. The exchange-correlation energy functional is in principle not known and describes the quantum-mechanical contribution that is not included in the three other terms, including, *e.g.*, the difference between the kinetic-energy functionals $T[n]$ and $T_0[n]$. The Hartree and external energy are known as functionals of the density, via Eqs. (2.2.2) and (2.2.3).

The goal of DFT is to calculate the GS density $n_{\text{GS}}(\boldsymbol{r})$ of an interacting-electrons system. In the Kohn-Sham (KS) approach, this is accomplished by introducing a fictitious, auxiliary system of non-interacting electrons. This system is constrained to

have the same GS density as for interacting electrons, as shown in Ref. [39]. Using the properties of non-interacting electron systems, one founds that the exact GS electronic density, *i.e.*, the one which minimizes the functional $E[n]$ [38], can be written as

$$n_{\mathrm{GS}}(\boldsymbol{r}) = \sum_{\nu=1}^{N} |\psi_{\nu}^{\mathrm{KS}}(\boldsymbol{r})|^2 \ , \tag{2.2.4}$$

where the single-particle wave functions $\psi_{\nu}^{\mathrm{KS}}(\boldsymbol{r})$ are the solution of the single-particle KS equations

$$\left[-\frac{\nabla^2}{2} + v(\boldsymbol{r}) + v_{\mathrm{H}}(\boldsymbol{r},[n]) + v_{\mathrm{xc}}(\boldsymbol{r},[n])\right] \psi_{\nu}^{\mathrm{KS}}(\boldsymbol{r}) = \varepsilon_{\nu}^{\mathrm{KS}}\, \psi_{\nu}^{\mathrm{KS}}(\boldsymbol{r}) \ , \tag{2.2.5}$$

where the potentials $v(\boldsymbol{r})$, $v_{\mathrm{H}}(\boldsymbol{r},[n])$, and $v_{\mathrm{xc}}(\boldsymbol{r},[n])$ are obtained by the density functional derivatives of the corresponding energy functional of Eq. (2.2.1). The different terms can be summarized to an effective KS potential $v_{\mathrm{KS}}(\boldsymbol{r},[n]) = v(\boldsymbol{r}) + v_{\mathrm{H}}(\boldsymbol{r},[n]) + v_{\mathrm{xc}}(\boldsymbol{r},[n])$. Furthermore, $\varepsilon_{\nu}^{\mathrm{KS}}$ are the KS energies.

Equation (2.2.5) looks like an ordinary single-particle Schrödinger equation. However, a closer look reveals a dependence of $v_{\mathrm{KS}}(\boldsymbol{r},[n])$ on the KS wave functions and, therefore, Eq. (2.2.5) has to be solved self-consistently. Furthermore, approximations for the generally unknown exchange-correlation potential $v_{\mathrm{xc}}[n]$ become indispensable.[3] The self-consistent solution of the KS equations is generally performed numerically. More details on this are given in Chapter 3. Now, regarding the many-electrons problem for the GS as solved, we can come back to the vibrational aspects of the nuclear motion in the next section.

2.3 Phonons in solids

In this section, we discuss the theoretical background of phonons in solids. The starting point is the introduction of the harmonic approximation in Section 2.3.1, where we also discuss the concept of the dynamical matrix. Then, we deal with the peculiarity of phonons in polar crystals and investigate the influences of Γ-point phonons on the reflectivity of the crystal in Section 2.3.2.

[3] The approximation we used in this work for $v_{\mathrm{xc}}[n]$ or, equivalently, $E_{\mathrm{xc}}[n]$ is reported in Ref [40].

2.3.1 Harmonic approximation and dynamical matrix

For the description of lattice vibrations in solids, we follow Chapter 3 of Ref. [37]. As discussed before, the effective nuclear Hamiltonian has the form[4]

$$\hat{H}_n(\mathscr{R}) = \hat{T}_n(\mathscr{R}) + \mathscr{V}(\mathscr{R}) \,. \tag{2.3.1}$$

Now, the periodicity of the system is used to divide the crystal into (irreducible and periodic) unit cells, which are labeled with the index l. The position of each unit cell is determined by the corresponding Bravais lattice vector $\boldsymbol{R}_l$. In the most general case we have N_{atom} atoms in each unit cell. The equilibrium position of each of these atoms is given by the vector $\boldsymbol{\tau}_i$, with $i = 1, ..., N_{\text{atom}}$. Accordingly, we indicate with $\boldsymbol{U}_{li}$ the displacement from equilibrium of atom i in the unit cell l. Thus, the general nuclear position $\boldsymbol{R}_I$[5] can be specified as

$$\boldsymbol{R}_I \equiv \boldsymbol{R}_{li} = \boldsymbol{R}_l + \boldsymbol{\tau}_i + \boldsymbol{U}_{li} = \boldsymbol{R}_{li}^{(0)} + \boldsymbol{U}_{li} \,, \tag{2.3.2}$$

where the equilibrium positions, $\boldsymbol{R}_{li}^{(0)} = \boldsymbol{R}_l + \boldsymbol{\tau}_i$, minimize the effective potential $\mathscr{V}(\mathscr{R})$.

In order to simplify the notation, a "super"-index $\mu \equiv (\alpha, i)$ is introduced, where α indicates the Cartesian component. Expanding the effective potential up to the second order in the displacements yields

$$\mathscr{V}(\mathscr{R}) \approx \mathscr{V}^{(0)} + \sum_{l,\mu} \left.\frac{\partial \mathscr{V}}{\partial R_{l\mu}}\right|_0 U_{l\mu} + \frac{1}{2} \sum_{l,\mu} \sum_{l',\mu'} \left.\frac{\partial^2 \mathscr{V}}{\partial R_{l\mu}\, \partial R_{l'\mu'}}\right|_0 U_{l\mu}\, U_{l'\mu'} \,, \tag{2.3.3}$$

where the derivatives are taken at equilibrium configuration $\mathscr{R}^{(0)}$. The partial derivatives in the linear term vanish

$$\left.\frac{\partial \mathscr{V}}{\partial R_{l\mu}}\right|_0 = -F_{l\mu}\big|_0 = 0 \,, \tag{2.3.4}$$

because they describe the forces acting on the atoms in equilibrium position. The second-order partial derivatives

$$\left.\frac{\partial^2 \mathscr{V}}{\partial R_{l\mu}\, \partial R_{l'\mu'}}\right|_0 \equiv \Phi_{l\mu,l'\mu'} \tag{2.3.5}$$

define the interatomic harmonic force constants $\Phi_{l\mu,l'\mu'}$. The insertion of Eq. (2.3.3) into Eq. (2.3.1) yields the expression of the Hamiltonian in the *harmonic approximation*. Furthermore, the introduction of the force constants leads directly to the dynamical matrix, which is defined in reciprocal space as Fourier transformation of $\Phi_{l\mu,l'\mu'}$ and

[4] We omit from now on the operator hat in the adiabatic potential.

[5] To be consistent with our previous notation, we introduce $I \equiv (l, i)$ to describe the position of all nuclei in the crystal.

can be written as[6]

$$D_{\mu,\mu'}(\boldsymbol{q}) = \frac{1}{\sqrt{M_i M_{i'}}} \sum_{l'} \Phi_{0\mu,l'\mu'}\, e^{\mathrm{i}\,\boldsymbol{q}\cdot\boldsymbol{R}_{l'}} \,. \tag{2.3.6}$$

In real crystals, time-dependent lattice vibrations have to be considered and, therefore, time-dependent $\boldsymbol{R}_{li}(t)$ and $\boldsymbol{U}_{li}(t)$. The (classical) equation of motion for the time-dependent lattice vibrations $\boldsymbol{U}_{li}(t)$, derived by the Euler-Lagrange equations, reads

$$M_i\, \ddot{U}_{l\mu}(t) = -\sum_{l'\mu'} \Phi_{l\mu,l'\mu'}\, U_{l'\mu'}(t) \,. \tag{2.3.7}$$

The standard solution of these equations of motions is given at a fixed $\boldsymbol{q}$ by the *ansatz* [41]

$$U_{l\mu}(t) = \frac{1}{\sqrt{M_i}}\, w_\mu(\boldsymbol{q})\, e^{\mathrm{i}\,(\boldsymbol{q}\cdot\boldsymbol{R}_l - \omega t)} \,. \tag{2.3.8}$$

Inserting Eq. (2.3.8) into Eq. (2.3.7) results in the eigenvalue equation for the dynamical matrix

$$\sum_{\mu'} D_{\mu\mu'}(\boldsymbol{q})\, w^j_{\mu'}(\boldsymbol{q}) = \left[\omega^j(\boldsymbol{q})\right]^2 w^j_\mu(\boldsymbol{q}) \,, \tag{2.3.9}$$

where $w^j_\mu(\boldsymbol{q})$ are the phonon eigenvectors for a specific $\boldsymbol{q}$ with corresponding eigenfrequencies $\omega^j(\boldsymbol{q})$. This solution represents the $j = 1, ..., 3\,N_{\mathrm{atom}}$ phonon normal modes of the system for each phonon wave vector $\boldsymbol{q}$. In the next subsection, we focus on phonons at vanishing wave vector (Γ point in the Brillouin zone of the crystal), which are the only relevant ones for the description of first-order Raman scattering.

As seen in Chapter 1, further necessary ingredients for calculating the Raman cross section are transition elements in the form $\langle\sigma|\hat{Q}_q\,|\rho\rangle$, where $|\rho\rangle$ and $|\sigma\rangle$ are eigenstates of the harmonic Hamiltonian in second quantization. In this case, the phonon normal coordinate operator $\hat{Q}_q$ is defined as

$$\hat{Q}_q = \frac{1}{\sqrt{2\,\omega(\boldsymbol{q})}} \left(\hat{b}_q + \hat{b}^\dagger_{-q}\right) \,, \tag{2.3.10}$$

where $\hat{b}_q$ and $\hat{b}^\dagger_q$ are the phonon (bosonic) annihilation and creation operators, respectively. The transition matrix element between two phonon states, $|\rho\rangle$ and $|\sigma\rangle$, with wave vector $\boldsymbol{q}=0$, reads[7]

$$\langle\sigma|\hat{Q}_0\,|\rho\rangle = \frac{1}{\sqrt{2\,\omega(0)}} \left[\sqrt{\rho}\,\delta_{\rho,\sigma-1} + \sqrt{\rho+1}\,\delta_{\rho,\sigma+1}\right] \,. \tag{2.3.11}$$

[6] Here, we made use of the translational symmetry of the interatomic force constants, which are only dependent on $|\mathbf{R}_l - \mathbf{R}_{l'}|$.

[7] More details about the derivation are given Chapter 3 of Ref. [37].

2.3.2 Γ-point phonons in polar crystals

In this section, the peculiarity of Γ-point ($\boldsymbol{q}=0$) phonons in polar crystals is addressed. In order to sketch the relevant aspects of Γ phonons in polar systems, we consider, as a prototype case, a crystal with two non-identical atoms in the unit cell. The six phonon modes of this system at $\boldsymbol{q}=0$ are classified as *acoustic* modes, corresponding thus to the three independent translations, and the three remaining so-called *optical* modes. In the latter modes, the two ionic sub-lattices oscillate against each other, which may give origin to a macroscopic electric field, due the opposite movement of contrary charges. This field would induce long-range restoring forces. Further analysing the optical modes, one can distinguish between the longitudinal-optical (LO) modes, which are defined by the vanishing vector product $\boldsymbol{q}\times\boldsymbol{w}=0$, where $\boldsymbol{w}$ is the phonon-polarization vector, introduced in Eq. (2.3.8), and transversal-optical (TO) modes, which are characterized by $\boldsymbol{q}\cdot\boldsymbol{w}=0$. A macroscopic electric field, however, only occurs in the case of LO phonons [37], and results in a splitting of the LO and TO modes for $\boldsymbol{q}\approx 0$, which is called *LO-TO splitting*.[8]

In the general case, this splitting is anisotropic. In order to deal with this effect, an extension to the dynamical matrix at the Γ point is necessary.[9] More precisely, the dynamical matrix can be divided into an analytical and a non-analytical part as follows

$$\boldsymbol{D}(\boldsymbol{q}\to 0)=\boldsymbol{D}^{\text{an}}(\boldsymbol{q}=0)+\boldsymbol{D}^{\text{non-an}}(\boldsymbol{q}\to 0)\,, \tag{2.3.12}$$

where $\boldsymbol{D}^{\text{an}}(\boldsymbol{q}=0)$ is the matrix in absence of macroscopic electric fields. On the other hand, the value of the non-analytic part $\boldsymbol{D}^{\text{non-an}}(\boldsymbol{q}\to 0)$ depends on the direction along which $\boldsymbol{q}$ vanishes. The formal expression for this contribution is [42]

$$D^{\text{non-an}}_{\mu\,\mu'}(\boldsymbol{q}\to 0)=\frac{4\pi}{\Omega}\frac{1}{\sqrt{M_i\,M_{i'}}}\frac{\left(\hat{\boldsymbol{q}}\cdot\boldsymbol{Z}^{*\,\mathrm{T}}_i\right)_\alpha\cdot\left(\boldsymbol{Z}^{*\,\mathrm{T}}_{i'}\cdot\hat{\boldsymbol{q}}\right)_{\alpha'}}{\hat{\boldsymbol{q}}^{\mathrm{T}}\cdot\boldsymbol{\epsilon}^{\infty}\cdot\hat{\boldsymbol{q}}}\,. \tag{2.3.13}$$

This expression includes the tensors of the *Born effective charges* $\boldsymbol{Z}^*$, the *dielectric-constant tensor* in the long wavelength limit $\boldsymbol{\epsilon}^{\infty}$, and the normalized $\boldsymbol{q}$-direction vector $\hat{\boldsymbol{q}}\equiv\boldsymbol{q}/|\boldsymbol{q}|$. The Born effective-charge tensor elements $Z^*_{i,\alpha\beta}$ of atom i are related to the macroscopic polarization $\boldsymbol{P}$ by

$$Z^*_{i,\alpha\beta}=\Omega\left.\frac{\partial P_\alpha}{\partial U_{i\beta}(\Gamma)}\right|_0\,, \tag{2.3.14}$$

where α defines the direction of polarization and β the direction of the displacement $U_{i\beta}(\Gamma)$. In addition, the Born effective charges have to satisfy the sum rule [42]

[8] For a more detailed description of the LO-TO splitting see Chapter 3 of Ref. [37].

[9] Periodic boundary conditions (PBC), which are used in most of the codes, do not allow for the presence of any macroscopic electric field. Therefore, calculations using PBC yield an analytical dynamical matrix, which does not include any LO-TO splitting.

$$\sum_{i}^{N_{\text{atom}}} \boldsymbol{Z}_i^* = 0 \,, \tag{2.3.15}$$

to preserve the charge neutrality of the unit cell. The polarization of the general j-th phonon mode at Γ can be described by the *mode-related effective-charge* vector $\widetilde{\boldsymbol{Z}}_j^*$, which is defined as [42]

$$\widetilde{Z}_{j,\alpha}^* = \frac{1}{L_j} \sum_{i,\beta} Z_{i,\alpha\beta}^* \, u_{i,\beta}^j(\Gamma) = \frac{1}{L_j} \sum_i \boldsymbol{Z}_i^* \cdot \boldsymbol{u}_i^j(\Gamma) \,, \tag{2.3.16}$$

where $\boldsymbol{u}_i^j(\Gamma)$ is the eigendisplacement of the j-th phonon mode, normalized as $\sum_i M_i |\boldsymbol{u}_i^j(\Gamma)|^2 = 1$ and with length $L_j = \sqrt{\sum_i |\, \boldsymbol{u}_i^j(\Gamma)|^2}$.

The quantities described in the previous paragraphs can be used to calculate the *reflectivity* $\mathrm{R}(\omega, \hat{\boldsymbol{q}})$ of a solid, which determines the amount of incident light that gets reflected,[10] and is defined along the direction $\hat{\boldsymbol{q}}$ as

$$\mathrm{R}(\omega, \hat{\boldsymbol{q}}) = \left| \frac{\epsilon^{1/2}(\omega, \hat{\boldsymbol{q}}) - 1}{\epsilon^{1/2}(\omega, \hat{\boldsymbol{q}}) + 1} \right|^2 \,, \tag{2.3.17}$$

where we introduced the low-frequency (infrared) dielectric function $\epsilon(\omega, \boldsymbol{q})$. This function specifies the *infrared response* of the material and can be written as [42]

$$\epsilon(\omega, \hat{\boldsymbol{q}}) = \hat{\boldsymbol{q}}^{\mathrm{T}} \cdot \boldsymbol{\epsilon}^{\infty} \cdot \hat{\boldsymbol{q}} + \frac{4\pi}{\Omega} \sum_j \frac{L_j^2}{\omega^j(\Gamma) - \omega} \left| \widetilde{\boldsymbol{Z}}_j^* \cdot \hat{\boldsymbol{q}} \right|^2 \,, \tag{2.3.18}$$

where the first summand is the electronic contribution and the frequencies $\omega^j(\Gamma)$ are the square root of the eigenvalues of $\boldsymbol{D}^{\mathrm{an}}(\boldsymbol{q} = 0)$.

2.4 Optical properties

In this section, we deal with the optical properties of solids, including two approaches for obtaining the dielectric function and its variations due to phonons, as required for the (macroscopic) Raman-scattering approach illustrated in Chapter 1. In particular, Section 2.4.1 deals with the theoretical framework of time-dependent density-functional theory, whereas Section 2.4.2 introduces the basics of many-body perturbation theory. Both sections mainly follow the guidelines of Ref. [43]. Then, we dedicate Section 2.4.3 to the general definition of the high-frequency dielectric tensor $\boldsymbol{\epsilon}^{\infty}$. Finally, some issues about the fundamental bandgap are discussed in Section 2.4.4 .

[10] The allowed values for $\mathrm{R}(\omega, \hat{\boldsymbol{q}})$ range between 0% and 100% of reflection.

2.4.1 Time-dependent density-functional theory

The standard DFT-KS formalism, outlined in Section 2.2, only gives insights to ground-state properties. Therefore, a different theoretical approach is required when it comes to describing excitations in solids, as in the case of the optical properties. In this context, a first approach is the *time-dependent density-functional theory* (TDDFT), which implies the time-dependent electron density as main descriptor quantity. The theoretical ground of TDDFT relies on the Runge-Gross theorem [44], which is the time-dependent counterpart to the Hohenberg-Kohn theorem mentioned in Section 2.2. The Runge-Gross theorem states that the (time-dependent) external potential of a many-body system (of electrons) $v(\boldsymbol{r},t)$ is completely determined by its time-dependent (TD) density $n(\boldsymbol{r},t)$ at a fixed initial state $|\phi_0\rangle$ at t_0. From this follows that every observable is a functional of the time-dependent density [44].

Similar to the static KS system, we introduce a fictitious TD-KS system, which reproduces the electron density $n(\boldsymbol{r},t)$ of an interacting-electron system. The general TD-KS equations have the form

$$\mathrm{i}\,\frac{\partial}{\partial t}\psi_\nu^{\mathrm{KS}}(\boldsymbol{r},t) = \left[-\frac{\nabla^2}{2} + v_{\mathrm{KS}}(\boldsymbol{r},t,[n])\right]\psi_\nu^{\mathrm{KS}}(\boldsymbol{r},t)\,, \tag{2.4.1}$$

where

$$\begin{aligned} v_{\mathrm{KS}}(\boldsymbol{r},t,[n]) &= v(\boldsymbol{r},t) + \int d\boldsymbol{r}'\,\frac{n(\boldsymbol{r}',t)}{|\boldsymbol{r}-\boldsymbol{r}'|} + v_{\mathrm{xc}}(\boldsymbol{r},t,[n])\ , \\ n(\boldsymbol{r},t) &= \sum_\nu |\psi_\nu^{\mathrm{KS}}(\boldsymbol{r},t)|^2\ , \end{aligned} \tag{2.4.2}$$

define the TD effective potential and density, respectively, described in terms of the single particle orbitals $\psi_\nu^{\mathrm{KS}}(\boldsymbol{r},t)$. Furthermore, the potentials are defined in close analogy to $v_{\mathrm{KS}}(\boldsymbol{r},[n])$, introduced in the time-independent KS equations of Section 2.2. Equation (2.4.1) is formally exact. However, to proceed further approximations of the exchange-correlation potential $v_{\mathrm{xc}}(\boldsymbol{r},t,[n])$ become necessary.

If the system underlies a weak time-dependent perturbation, the use of a *linear-response theory* is possible.[11] In this framework, as it is implemented in the software package `exciting`, an important quantity is the linear susceptibility (or polarizability) χ, defined as[12]

$$\chi(\boldsymbol{r},\boldsymbol{r}',t-t') = \left.\frac{\partial n_(\boldsymbol{r},t)}{\partial v(\boldsymbol{r}',t')}\right|_{v(\boldsymbol{r},t_0)} \equiv \chi\ , \tag{2.4.3}$$

[11] In our case, we investigate the density response δn with respect to a modification of the potential δv.
[12] It is only known for the KS system, not for the system of interacting electrons.

which can be evaluated for the system of interacting electrons and also for the KS-system of non-interacting electrons as

$$\chi_{\mathrm{KS}}(\boldsymbol{r},\boldsymbol{r}',t-t') = \left.\frac{\partial n(\boldsymbol{r},t)}{\partial v_{\mathrm{KS}}(\boldsymbol{r}',t')}\right|_{v(\boldsymbol{r},t_0)} \equiv \chi_{\mathrm{KS}} \,, \tag{2.4.4}$$

considering the potential $v_{\mathrm{KS}}(\boldsymbol{r},t)$ instead. Further reshaping of the definition of χ yields a Dyson equation in $\boldsymbol{q}$ space, including both response functions χ and χ_{KS}, which can be written as

$$\chi(\boldsymbol{q},\omega) = \chi_{\mathrm{KS}}(\boldsymbol{q},\omega) + \chi_{\mathrm{KS}}(\boldsymbol{q},\omega)\,\left[f_{\mathrm{H}}(\boldsymbol{q}) + f_{\mathrm{xc}}(\boldsymbol{q},\omega)\right]\,\chi(\boldsymbol{q},\omega)\,. \tag{2.4.5}$$

The quantities f_{H} and f_{xc} are the Hartree and exchange-correlation kernel, which are defined in real-space as

$$\begin{aligned} f_{\mathrm{H}}(\boldsymbol{r},\boldsymbol{r}',t-t') &= \left.\frac{\partial v_{\mathrm{H}}(\boldsymbol{r},t)}{\partial n(\boldsymbol{r}',t')}\right|_{v(\boldsymbol{r},t_0)} = \hat{w}(\boldsymbol{r},\boldsymbol{r}')\,\delta(t'-t)\,, \\ f_{\mathrm{xc}}(\boldsymbol{r},\boldsymbol{r}',t-t') &= \left.\frac{\partial v_{\mathrm{xc}}(\boldsymbol{r},t)}{\partial n(\boldsymbol{r}',t')}\right|_{v(\boldsymbol{r},t_0)}\,, \end{aligned} \tag{2.4.6}$$

where $\hat{w}(\boldsymbol{r},\boldsymbol{r}') = 1/|\boldsymbol{r}-\boldsymbol{r}'|$ is the bare Coulomb potential. f_{xc} is an unique-determined functional of the density $n(\boldsymbol{r},t)$ and requires an approximation for v_{xc} in order to solve Eq. (2.4.5) self-consistently. The approximation that we used in this work, is the so-called *random-phase approximation* (RPA), which is defined by setting $f_{\mathrm{xc}}^{\mathrm{RPA}} = 0$. In particular, this approximation includes *local-field effects*,[13] but no electron-hole pairs.

The macroscopic dielectric function can be obtained in this approach by

$$\begin{aligned} \epsilon_{\mathrm{M}}(\boldsymbol{q},\omega) &= \frac{1}{\epsilon_{00}^{-1}(\boldsymbol{q},\omega)}\,, \\ \epsilon^{-1}(\boldsymbol{q},\omega) &= 1 + f_{\mathrm{H}}(\boldsymbol{q})\,\chi(\boldsymbol{q},\omega)\,. \end{aligned} \tag{2.4.7}$$

2.4.2 Many-body perturbation theory

The optical properties of a solid can also be obtained using the alternative framework given by *many-body perturbation theory* (MBPT). Concerning this, the concept of *quasi-particles* (QPs) has to be introduced. QPs only appear in many-body systems and represent collective excitations, which, however, possess similar properties as "normal" particles. In this picture for many-body systems, excitations in the crystal only involve transitions between QP states.

The main mathematical description of QPs in the framework of MBPT relies on

[13] The slowly varying (macroscopic) external potential of a crystal yields variations of the total effective potential on a microscopic scale. These aberrations on the small scale of the effective potential are referred as local-field effects.

Green's functions (GFs), the poles of which give insights into QP energies, in the case of the single-particle (1P) GF, and excitation energies, in the case of higher-order GFs.[14] The calculation of the 1P GF, however, requires the solution of a set of coupled equations, which are known as *Hedin equations* [46] of MBPT. These self-consistent equations include relations among quantities such as the GF G, the *self-energy* Σ, the *vertex function* Γ, the polarization P, and the screened Coulomb potential W.[15] A great simplification of the Hedin equations is given by the *GW-approximation*, which sets the self-energy to $\Sigma \approx \mathrm{i}WG$. Within this approximation, the solution of the Dyson equation for the 1P GF is feasible and yields the QP energies $\varepsilon^{\mathrm{QP}}$ of an independent quasi-electron or quasi-hole [47].

Beyond the non-interacting QP picture are excitation energies, which include the interaction of two (or more) QPs. The two-particles (2P) GF characterizes the time evolution of two QPs and its poles determine the corresponding excitation energy. Therefore, the 2P GF can be used to describe *excitons*, which are bound states of a quasi-electron and a quasi-hole. The 2P GF also satisfies a Dyson equation [47]. More technically, the solution of the Dyson equation for the 2P GF can be turned into the solution of an eigenvalue problem for an effective Hamiltonian operator in a two-particles Hilbert space. A general two-particles (electron and hole) quantum state for optical transitions ($\boldsymbol{k}$=$\boldsymbol{k}'$) can be written as[16]

$$\psi^{\mathrm{2P}}(\boldsymbol{r}_{\mathrm{e}}, \boldsymbol{r}_{\mathrm{h}}) = \sum_{vc\boldsymbol{k}} A_{vc\boldsymbol{k}}\, \psi_{c\boldsymbol{k}}(\boldsymbol{r}_{\mathrm{e}})\, \psi^{*}_{v\boldsymbol{k}}(\boldsymbol{r}_{\mathrm{h}}) \,, \tag{2.4.8}$$

which implies a superposition of (QP-)states, made up by a (quasi-)electron and (quasi-)hole with wave functions $\psi_{c\boldsymbol{k}}(\boldsymbol{r}_{\mathrm{e}})$ and $\psi^{*}_{v\boldsymbol{k}}(\boldsymbol{r}_{\mathrm{h}})$, respectively. Using the representation in Eq. (2.4.8) formally leads to the *Bethe-Salpeter equation* (BSE) [46]

$$\hat{H}^{\mathrm{BSE}}\, \boldsymbol{A}_{\kappa} = E^{\mathrm{BSE}}_{\kappa}\, \boldsymbol{A}_{\kappa} \,, \tag{2.4.9}$$

including the effective 2P Hamiltonian $\hat{H}^{\mathrm{BSE}}$, the total excitation energy of the system $E^{\mathrm{BSE}}_{\kappa}$, and the eigenvectors $\boldsymbol{A}_{\kappa}$, which contain all coefficients $A^{\kappa}_{vc\boldsymbol{k}}$ and diagonalize the effective Hamiltonian. The Hamiltonian operator in Eq. (2.4.9) is defined in the Hilbert space of product states of a (quasi-)electron and a (quasi-)hole. Furthermore, $\hat{H}^{\mathrm{BSE}}$ can be divided into three contributions as

$$\hat{H}^{\mathrm{BSE}} = \hat{H}^{\mathrm{diag}} + 2\gamma_{\mathrm{x}}\hat{H}^{\mathrm{x}} + \gamma_{\mathrm{c}}\hat{H}^{\mathrm{c}} \,. \tag{2.4.10}$$

[14] For detailed descriptions and explicit definitions of the Green's functions see Ref. [45].

[15] A detailed description of these quantities is beyond the scope of this thesis. For further details we refer to Ref. [46].

[16] At this point, a dependence on the starting point of the calculation has to be considered. The starting point determines if single particle or quasi-particle wave functions have to be included into Eq. (2.4.9), which then yield different excitation energies.

In the matrix representation, which is defined by the expansion in Eq. (2.4.8), the matrix elements of the three individual terms of Eq. (2.4.11) are given as

$$\begin{aligned}
\hat{H}^{\text{diag}}_{vc\boldsymbol{k},\,v'c'\boldsymbol{k}'} &= (\varepsilon_{c\boldsymbol{k}} - \varepsilon_{v\boldsymbol{k}})\,\delta_{v,v'}\,\delta_{c,c'}\,\delta_{\boldsymbol{k},\boldsymbol{k}'}\,, \\
\hat{H}^{\text{x}}_{vc\boldsymbol{k},\,v'c'\boldsymbol{k}'} &= \int d\boldsymbol{r}' \int d\boldsymbol{r}'\; \psi_{v\boldsymbol{k}}(\boldsymbol{r})\; \psi^*_{c\boldsymbol{k}}(\boldsymbol{r})\; \bar{v}_{\text{c}}(\boldsymbol{r},\boldsymbol{r}')\; \psi_{v'\boldsymbol{k}'}(\boldsymbol{r}')\; \psi^*_{c'\boldsymbol{k}'}(\boldsymbol{r}')\,, \\
\hat{H}^{\text{c}}_{vc\boldsymbol{k},\,v'c'\boldsymbol{k}'} &= -\int d\mathbf{r} \int d\boldsymbol{r}'\; \psi_{v\boldsymbol{k}}(\boldsymbol{r}')\; \psi^*_{c\boldsymbol{k}}(\boldsymbol{r})\, W(\boldsymbol{r},\boldsymbol{r}')\, \psi_{v'\boldsymbol{k}'}(\boldsymbol{r})\, \psi^*_{c'\boldsymbol{k}'}(\boldsymbol{r}')\,.
\end{aligned} \tag{2.4.11}$$

The different terms in Eq. (2.4.11) characterize the independent QP transitions ($\hat{H}^{\text{diag}}$), the exchange interaction ($\hat{H}^{\text{x}}$), and the direct screening interaction ($\hat{H}^{\text{c}}$). In addition, the coefficients γ_{x} and γ_{c} define the level of approximation of the BSE.[17]

The physical quantity we are interested in is the macroscopic dielectric function, which can be defined in the framework of MBPT in the Cartesian direction α as

$$\epsilon^{\alpha}_{\text{M}}(\omega) = 1 - \frac{8\pi^2}{V} \sum_{\kappa} \left|t^{\alpha}_{\kappa}\right|^2 \left[\frac{1}{\omega - E^{\text{BSE}}_{\kappa} + \text{i}\,\eta} + \frac{1}{-\omega - E^{\text{BSE}}_{\kappa} - \text{i}\,\eta}\right]\,, \tag{2.4.12}$$

where V is the crystal volume, η the Lorentzian broadening, and

$$t^{\alpha}_{\kappa} = \sum_{vc\boldsymbol{k}} A^{\kappa}_{vc\boldsymbol{k}}\, \frac{\langle v\boldsymbol{k}|\hat{p}_{\alpha}|c\boldsymbol{k}\rangle}{\varepsilon_{c\boldsymbol{k}} - \varepsilon_{v\boldsymbol{k}}} \tag{2.4.13}$$

is the oscillator strength in the direction α, including the matrix elements of the momentum operator $\hat{p}_{\alpha}$. The macroscopic dielectric tensor $\boldsymbol{\epsilon}_{\text{M}}(\omega)$ is, as shown in Chapter 1, a key ingredient for the calculation of the Raman tensor of any order.

2.4.3 The high-frequency dielectric tensor

For the calculation of the reflectivity and the non-analytical correction to the dynamical matrix, the high-frequency dielectric tensor $\boldsymbol{\epsilon}^{\infty}$ is required. This tensor can be obtained from the frequency-dependent macroscopic dielectric function introduced in Eqs. (2.4.7) and (2.4.12)[18] in the static limit, $\omega \to 0$. Within this limit, the result which is obtained is [48]

$$\boldsymbol{\epsilon}^{-1}(\omega = 0) = \boldsymbol{\epsilon}_0^{-1} = (\boldsymbol{\epsilon}^{\infty})^{-1} + \boldsymbol{\epsilon}^{-1}_{\text{pol}}\,, \tag{2.4.14}$$

where we include the pure electronic contribution in $\boldsymbol{\epsilon}^{\infty}$ and all further polarizations effects (*e.g.*, caused by phonons) in $\boldsymbol{\epsilon}_{\text{pol}}$. Since our calculations only capture the electronic contribution, the dielectric tensor in the zero-frequency limit gives exactly $\boldsymbol{\epsilon}^{\infty}$, which is generally referred in the literature as *high-frequency* dielectric tensor. This

[17] More details about the coefficients γ_{x} and γ_{c} and about the three terms of the Hamiltonian can be found in Ref. [43].

[18] In fact, the frequency-dependent dielectric function has a tensorial character.

notation can appear misleading. In fact, ϵ^{∞} indicates the tensor $\epsilon(\omega)$ at a frequency which is higher than all phonon excitations and lower than any electronic transitions.

2.4.4 Fundamental bandgap

For of a semiconductor such as gallium oxide, the fundamental bandgap is an important property, which can be determined by the knowledge of the frequency-dependent dielectric function. In particular, the fundamental bandgap determines the onset of the imaginary part of the dielectric function. A correct theoretical treatment of the bandgap required methodologies that are beyond the density-functional theory [49]. In this work, we use the so-called *scissor-operator* approximation, which consists in imposing a constant shift to all KS conduction bands so that the KS bandgap nears the real one. Within this approximation, the effect on the dielectric function is a constant shift of the theoretical onset towards the experimental one.

3. Computational Methodology

This chapter is dedicated to the description of the computational methodology used in this thesis. Section 3.1 deals with the numerical solution of the Kohn-Sham equations, which is needed for the determination of the relevant ground-state properties. Then the frozen-phonon approach is introduced in Section 3.2. Finally, the workflow of a Raman calculation is presented in Section 3.3. Sections 3.1 and 3.2 follow the structure outlined in Ref. [32].

3.1 Numerical solution of the Kohn-Sham equations

This section illustrates how the Kohn-Sham (KS) equations, outlined in Section 2.2, can be solved numerically. In order to treat the KS equations efficiently, an accurate representation of the single-particle KS wave functions $\psi^{\mathrm{KS}}_{\nu\boldsymbol{k}}(\boldsymbol{r})$ in terms of a set of known "basis" functions is needed. As already mentioned in the previous chapter, all calculations in this thesis are done with the software package `exciting` [32], which uses *(linearized) argumented plane waves* (L)(APW) as basis-function set.

A general problem concerning the expansion in a basis set is that the behaviour of the KS wave functions $\psi^{\mathrm{KS}}_{\nu\boldsymbol{k}}(\boldsymbol{r})$ differs tremendously in the interatomic region, where they can be treated as slowly varying plane waves, and in the vicinity of atoms, where, due to electron localizations, very strong oscillations are present. Keeping this in mind, a first approach is to divide the full space into an *interstitial* (I) and a *muffin-tin* (MT) region, where the latter is a set of spheres localized around the atoms with a radius R^i_{MT}, which depends on the corresponding atomic species. The full KS wave function can be written as linear combination of *argumented plane waves* (APW)

$$\psi^{\mathrm{KS}}_{\nu\boldsymbol{k}}(\boldsymbol{r}) = \sum_{\boldsymbol{G}} C^{\boldsymbol{G}}_{\nu\boldsymbol{k}}\, \phi^{\mathrm{APW}}_{\boldsymbol{G}+\boldsymbol{k}}(\boldsymbol{r}) \,, \tag{3.1.1}$$

where $C_{\nu k}^{G}$ are the expansion coefficients and $\{\boldsymbol{G}\}$ is the set of reciprocal lattice vectors. The functions $\phi_{\boldsymbol{G+k}}^{\mathrm{APW}}(\boldsymbol{r})$ represent the APWs, which are defined as

$$\phi_{\boldsymbol{G+k}}^{\mathrm{APW}}(\boldsymbol{r}) = \begin{cases} \sum_{lm} A_{lmi}^{\boldsymbol{G+k}}\, u_{li}(r_i,\varepsilon)\, Y_{lm}(\hat{\boldsymbol{r}}_i) & \text{for } r_i \leq R_{\mathrm{MT}}^{i} \\ \dfrac{1}{\sqrt{\Omega}} \exp[\mathrm{i}\,(\boldsymbol{G+k})\cdot\boldsymbol{r}\,] & \text{for } \boldsymbol{r}\,\epsilon\,\mathrm{I}\,, \end{cases} \tag{3.1.2}$$

where i labels the atoms and $\boldsymbol{r}_i$ is the position relative to the atom i.[1] The first line in the equation above defines the MT region, where the wave function (WF) is expanded in the product of radial functions $u_{li}(r_i,\varepsilon)$ and spherical harmonics $Y_{lm}(\hat{\boldsymbol{r}}_i)$. Furthermore, the coefficients $A_{lmi}^{\boldsymbol{G+k}}$ arrange for continuous boundary-conditions between both areas. Solving the radial KS equation for $u_{li}(r_i,\varepsilon)$ and inserting in Eq. (3.1.2) yields the coefficients $A_{lmi}^{\boldsymbol{G+k}}$. Then, the original KS equations, Eq. (2.2.5), can be written in this basis as a generalized eigenvalue problem as

$$\boldsymbol{H}^{\boldsymbol{k}}\cdot\boldsymbol{C}^{\boldsymbol{k}} = \varepsilon\,\boldsymbol{S}^{\boldsymbol{k}}\cdot\boldsymbol{C}^{\boldsymbol{k}}\,, \tag{3.1.3}$$

where the elements of the matrices $\boldsymbol{H}^{\boldsymbol{k}}$ and $\boldsymbol{S}^{\boldsymbol{k}}$ are defined as follows

$$\begin{aligned} H_{\boldsymbol{GG'}}^{\boldsymbol{k}} &= \langle \phi_{\boldsymbol{G+k}} \,|-\tfrac{1}{2}\nabla^2 + v_{\mathrm{KS}}|\, \phi_{\boldsymbol{G'+k}}\rangle \\ S_{\boldsymbol{GG'}}^{\boldsymbol{k}} &= \langle \phi_{\boldsymbol{G+k}} \,|\, \phi_{\boldsymbol{G'+k}}\rangle\,, \end{aligned} \tag{3.1.4}$$

and $\boldsymbol{C}^{\boldsymbol{k}}$ is an eigenvector containing the coefficients from Eq. (3.1.1). Furthermore, a plane-wave cutoff $G_{\max}$ is introduced, such that the constraint $G_{\max} > |\boldsymbol{G}+\boldsymbol{k}|$ makes the matrices $\boldsymbol{H}^{\boldsymbol{k}}$ and $\boldsymbol{S}^{\boldsymbol{k}}$ finite. This is crucial for a numerical treatment and, therefore, an important parameter for the computation. In particular, a more adequate cutoff parameter is the dimensionless product $G_{\max}R_{\mathrm{MT}}$.[2]

Unfortunately, Eq. (3.1.3) is non-linear in the energy ε, since $\boldsymbol{H}^{\boldsymbol{k}}$ and $\boldsymbol{S}^{\boldsymbol{k}}$ are energy dependent as well. One approach to overcome the non-linearity problem is to keep fixed the energy values appearing in the radial functions u_{li} to some energy parameters ε_{li}. These fixed energy values have to be chosen to be almost equal to the real eigenenergies of the radial Schrödinger equation. Using the energy derivatives, $\dot{u}_{li}$, of the radial function and applying a Taylor-like expansion up the first order

$$u_{li}(r_i;\varepsilon) \simeq u_{li}(r_i;\varepsilon_{li}) + \dot{u}_{li}(r_i;\varepsilon_{li})\,(\varepsilon_{li}-\varepsilon)\,, \tag{3.1.5}$$

[1] The Bravais-lattice index is omitted in this section for the sake of simplicity.

[2] A reduction of R_{MT} requires an increase of $G_{\max}$ to maintain the same accuracy, wherefore it makes sense to use the product as cutoff parameter.

leads to the linearized APW (LAPW) basis functions, which have inside the MT the form

$$\phi^{\mathrm{LAPW}}_{\boldsymbol{G}+\boldsymbol{k}}(\boldsymbol{r}) = \sum_{lm} \left[A^{\boldsymbol{G}+\boldsymbol{k}}_{lmi}\; u_{li}(r_i;\varepsilon_{li}) + B^{\boldsymbol{G}+\boldsymbol{k}}_{lmi}\; \dot{u}_{li}(r_i;\varepsilon_{li}) \right] Y_{lm}(\hat{\boldsymbol{r}}_i)\ . \tag{3.1.6}$$

The LAPW basis functions fix therefore the non-linearity problem and make Eq. (3.1.3) linear solvable, due to the fact that the basis functions and hence the matrices $\boldsymbol{H}^{\boldsymbol{k}}$ and $\boldsymbol{S}^{\boldsymbol{k}}$ are not ε-dependent any more.

To solve the non-linearity problem, an alternative approach consists in expanding the KS wave functions using the APW+(lo) basis, where APW functions with fixed energy parameters ε_{li} are chosen. In this basis, in addition to the APWs, *local orbitals* (lo), $\phi^{\mathrm{lo}}_{\eta}(\boldsymbol{r})$, are included and defined to be non-zero only inside the MT spheres. Therefore, the wave functions within the APW+(lo) basis have the following form inside the MT region

$$\begin{aligned} \psi^{\mathrm{KS}}_{\nu\boldsymbol{k}}(\boldsymbol{r}) &= \sum_{\boldsymbol{G}} C^{\boldsymbol{G}}_{\nu\boldsymbol{k}}\, \phi^{\mathrm{APW}}_{\boldsymbol{G}+\boldsymbol{k}}(\boldsymbol{r}) \;+\; \sum_{\eta} C^{\eta}_{\nu\boldsymbol{k}}\, \phi^{\mathrm{lo}}_{\eta}(\boldsymbol{r}) \\ &= \sum_{lm} \left[c^{\boldsymbol{k}}_{lm}\, u_{li}(r_i;\varepsilon_{li}) + d^{\boldsymbol{k}}_{lm}\, \dot{u}_{li}(r_i;\varepsilon_{li}) \right] Y_{lm}(\boldsymbol{r}_i)\ . \end{aligned} \tag{3.1.7}$$

The APW+(lo) basis is an improvement over the LAPW one, because it allows for a higher flexibility and additionally includes smoothness of the basis functions.

There are several other possibilities to change or improve the APW basis, as, *e.g.*, including higher orders in the Taylor-like expansion of Eq. (3.1.5). However, they are not used in this thesis [32]. The appropriate choice of the expansion parameters enables the self-consistent solution of the KS equations up to the required accuracy.

3.2 Frozen-phonon approach to lattice dynamics

This section outlines the methodology implemented in `exciting` to obtain insights into lattice dynamics and phonon properties of crystals, namely the so-called *frozen-phonon* or *supercell approach*. Within this approach, the dynamical matrix $\boldsymbol{D}(\boldsymbol{q})$ and the corresponding phonon frequencies $\omega(\boldsymbol{q})$ for a specific wave vector $\boldsymbol{q}$ are achieved by performing total energy and force calculations for a given set of atomic configurations. The latter are obtained by displacing the atoms from their equilibrium positions according to a phonon-like displacement pattern. In order to do so, supercells, containing an appropriate number of unit cells, are considered (see, *e.g.*, a schematic representation in Figure 3.1). For a general wave vector $\boldsymbol{q}$, the phonon-like atomic displacements are given as

$$\boldsymbol{u}_{\boldsymbol{R},i}(Q_{\boldsymbol{q}}) = \frac{1}{\sqrt{M_i}}\, \boldsymbol{w}_i(\boldsymbol{q})\, e^{\,\mathrm{i}\boldsymbol{q}\cdot\boldsymbol{R}}\, Q_{\boldsymbol{q}}\ , \tag{3.2.1}$$

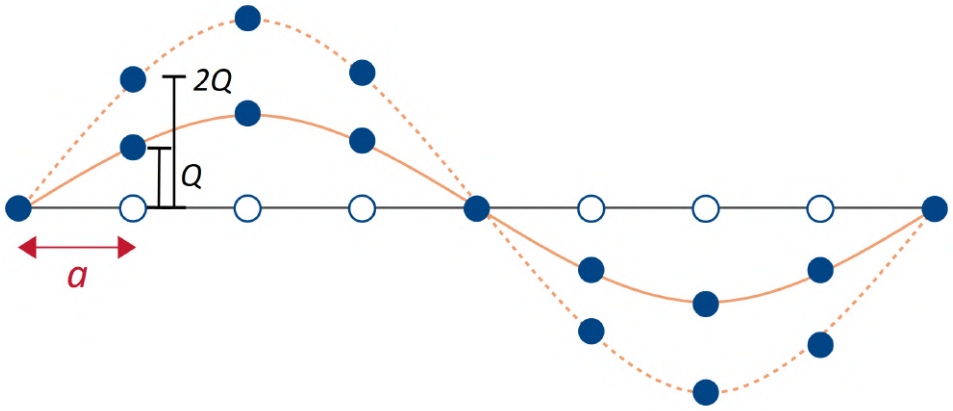

FIGURE 3.1: Schematic illustration of the frozen-phonon approach for a one-dimensional mono-atomic system with lattice constant a. A supercell that is 8 times larger than the unit cell is displayed. This supercell allows for periodic displacement of the atoms (blue circles) corresponding to the wave vector $q = 2\pi/\lambda$, with $\lambda = 8a$. Two displacement patterns with magnitudes Q and $2Q$ are shown.

where $\boldsymbol{R}$ is a lattice vector, $\boldsymbol{w}_i(\boldsymbol{q})$ a normalized polarization vector at $\boldsymbol{q}$, and $Q_{\boldsymbol{q}}$ the corresponding phonon normal coordinate, which specifies the maximum amplitude of the phonon displacement pattern.

Considering first-order Raman scattering, only Γ-point ($\boldsymbol{q} = 0$) phonons are relevant. In this case, the eigendisplacements $\boldsymbol{u}_{\boldsymbol{R},i}$ are real and reduce to

$$\boldsymbol{u}_{\boldsymbol{R},i}(Q_0) = \frac{1}{\sqrt{M_i}}\, \boldsymbol{w}_i(\Gamma)\, Q_0 \,. \tag{3.2.2}$$

For each displaced configuration, the forces acting on the atoms are calculated. Extracting the linear contribution to the force as a function of the atomic displacements, the relevant combinations of interatomic force constants are obtained, which fully determine the dynamical matrix at the Γ point. $\boldsymbol{D}(\Gamma)$ is then diagonalized to achieve the phonon frequencies $\omega(\Gamma)$.

3.3 Workflow of Raman calculations in `exciting`

The workflow of a first-order Raman calculation in **`exciting`** is schematically illustrated in Figure 3.2. The first requirement is the calculation of the dynamical matrix at the Γ point, which yields phonon eigenvectors and the corresponding frequencies. Then, all phonon modes are checked for their symmetry to distinguish between Raman-active, infrared-active, and silent modes.

To proceed further, one specific phonon mode has to be chosen. Along this mode several distorted geometries are created. For each of these geometries, ground-state (including the total energy, forces on atoms, *etc.*) and optical properties are obtained, particularly the dielectric function. The purpose of these calculations is to extract the

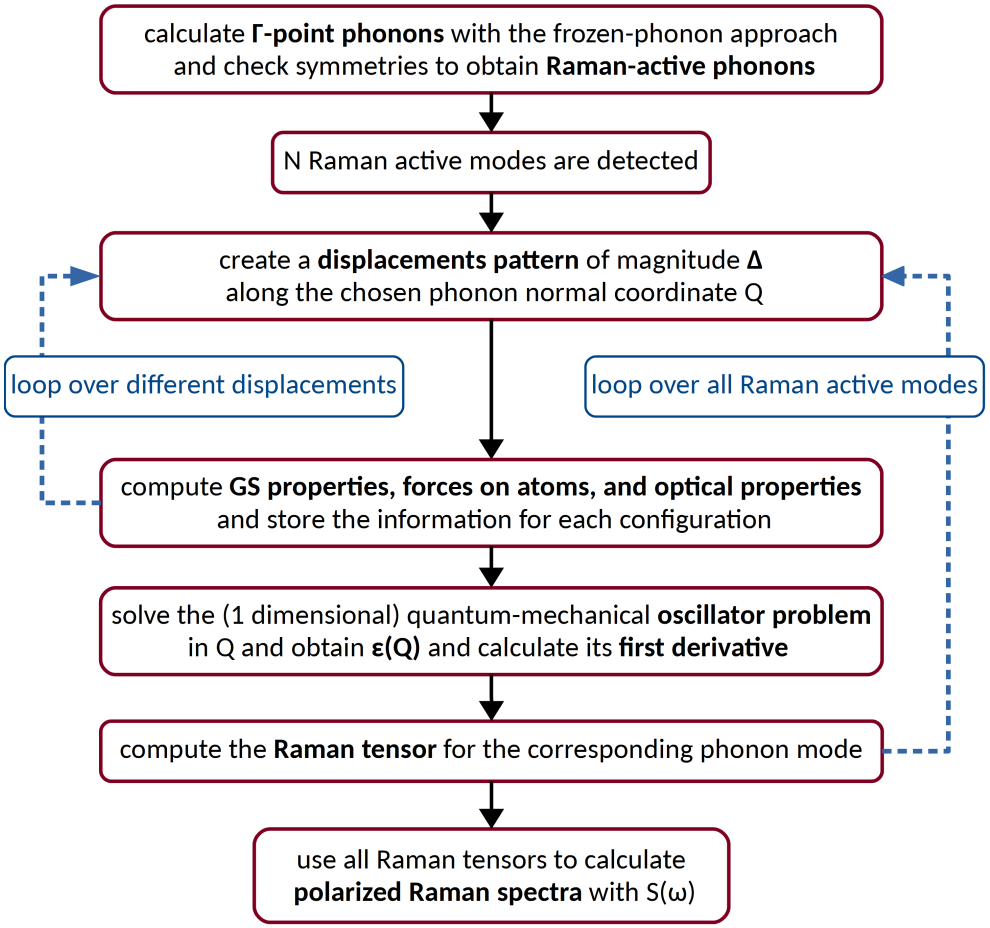

FIGURE 3.2: Workflow-diagram for Raman-scattering calculations in exciting.

dependence of the dielectric function on the phonon normal coordinates Q_0. Once all distorted geometries are completely calculated, the quantum-mechanical oscillator problem in the displacement amplitude u (which is proportional to Q_0) is solved and the numerical derivative $\partial\epsilon(\omega)/\partial u$ is calculated. Finally, the results of the previous calculations are used to calculate the Raman tensor and Raman-scattering efficiency. This procedure can be repeated for all desired Raman-active modes, to enable the calculation of a full-polarized Raman spectrum.

4. Results

As we mentioned in the introduction of this thesis, our goal is an accurate *ab initio* investigation of several relevant properties of gallium oxide. This chapter is dedicated to the presentation of our results. In particular, we focus on the only thermodynamically stable phase, the β phase, and additionally on the meta-stable α phase, which, however, can be stabilized under high pressure [22]. The structural properties of both phases are presented in Section 4.1, followed by lattice-dynamical and optical properties in Sections 4.2 and 4.3, respectively. Results of the Raman-scattering calculations are outlined and discussed in Section 4.4.

4.1 Structural properties

As a starting point, we give a short description of the crystal structure of the β and α phase in Section 4.1.1, including the spacegroup, unit cell, and lattice constants. Then, the results of the *ab initio* calculation of the lattice parameters including atomic relaxation are shown in Section 4.1.2.

4.1.1 Crystal structure

The stable β phase of Ga_2O_3 has a monoclinic crystal structure with the spacegroup C2/m or C_{2h}^3 in Schoenflies notation. Its primitive unit cell consists of 10 atoms, including four gallium and six oxygen atoms. Two inequivalent Ga atoms are surrounded by O atoms either in a tetrahedral or octahedral structure, as shown in Figure 4.1. The conventional monoclinic crystal structure is defined by three vectors $\boldsymbol{a}$, $\boldsymbol{b}$, and $\boldsymbol{c}$ as shown in Figure 4.1 . On the other hand, the parameters a, b, c, and the angle β define

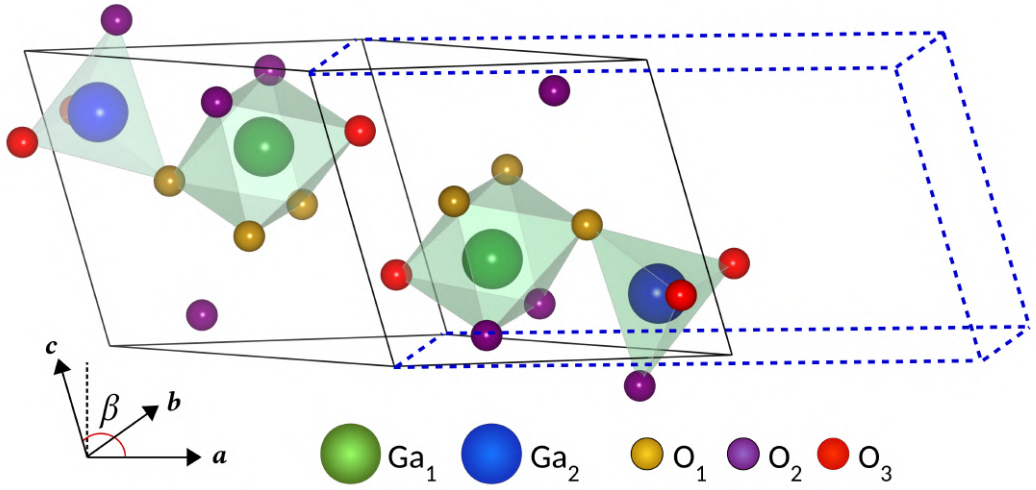

FIGURE 4.1: The primitive monoclinic unit cell of β-Ga_2O_3 (black solid line) contains 4 Ga and 6 O atoms. Different colors mark the 2 inequivalent Ga (Ga_1 = green, Ga_2 = blue) and 3 inequivalent O (O_1 = orange, O_2 = violet, and O_3 = red) atoms. The monoclinic cell is defined by the 4 parameters a, b, c, and β. The conventional cell (blue dashed line) has twice the size of the primitive cell and is defined by the lattice vectors $\boldsymbol{a}$, $\boldsymbol{b}$, and $\boldsymbol{c}$. The figure shows more than the 10 atoms of the unit cell in order to point out the tetrahedral and octahedral arrangement of O atoms around the inequivalent Ga atoms.

also the primitive (p) cell, with basis lattice vectors given by

$$\boldsymbol{a}_1^{(\mathrm{p})} = \tfrac{1}{2}\,(a,\,-b,\,0)\,, \qquad \boldsymbol{a}_2^{(\mathrm{p})} = \tfrac{1}{2}\,(a,\,b,\,0)\,, \qquad \boldsymbol{a}_3^{(\mathrm{p})} = c\,(\cos\beta,\,0,\,\sin\beta)\,, \tag{4.1.1}$$

with the corresponding conventional-cell volume $\Omega = abc\,|\sin\beta|$.

The α phase of Ga_2O_3 has the spacegroup $R\bar{3}c$ (D_{3d}^6) [23, 50] and, as well as for the β phase, the primitive (rhombohedral) unit cell consists of ten atoms, four Ga and six O atoms as illustrated in Figure 4.2. In this case, the primitive cell has a rhombohedral structure, whereas the conventional unit cell exhibits a hexagonal (h) structure. Two lattice parameters are required to describe the exact shape of either the primitive unit cell or the conventional hexagonal cell. The lattice vectors of the conventional structure are defined as

$$\boldsymbol{a}^{(\mathrm{h})} = (a_\mathrm{h},\,0,\,0)\,, \qquad \boldsymbol{b}^{(\mathrm{h})} = \tfrac{1}{2}\left(-a_\mathrm{h},\,\sqrt{3}\,a_\mathrm{h},\,0\right), \qquad \boldsymbol{c}^{(\mathrm{h})} = (0,\,0,\,c_\mathrm{h})\,, \tag{4.1.2}$$

with the conventional-cell volume $\Omega = a_\mathrm{h}^2 c_\mathrm{h}\,|\sin 60^\circ|$. In the hexagonal crystal structure there are only two inequivalent atoms in the unit cell, one Ga and one O atom.

The choice of representing the crystal in either the primitive or conventional structure does not affect its physical properties. However, the definition of the basis vectors and the Cartesian reference system have an impact on, *e.g.*, the symmetry of the dielectric and Raman tensors (see Sections 4.3 and 4.4), which has to be taken into account when comparing the results for different crystal representations.

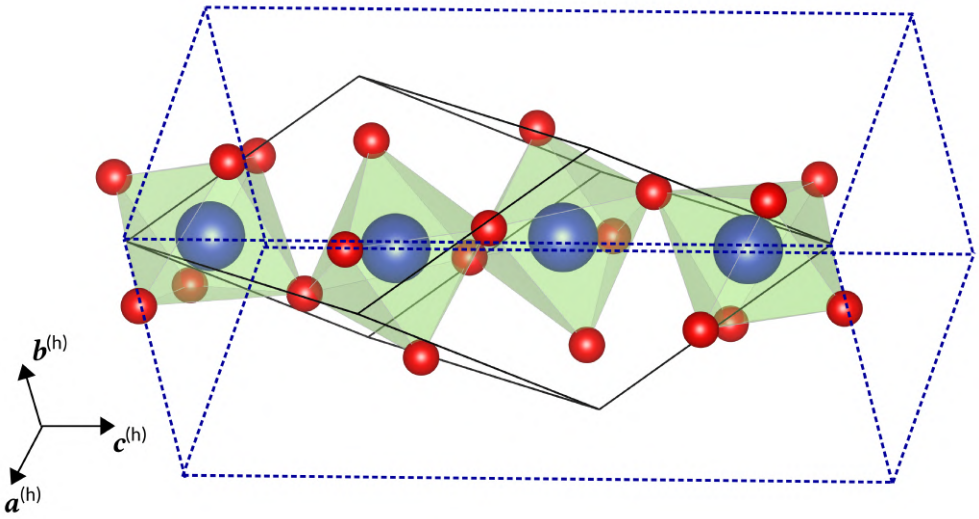

FIGURE 4.2: The primitive rhombohedral unit cell (black solid line) of α-Ga_2O_3 contains 4 Ga (blue) and 6 O (red) atoms. The (conventional) hexagonal cell is indicated by the dashed blue lines and corresponding basis lattice vectors.

4.1.2 Calculation of equilibrium parameters

For both phases, ground-state *ab initio* calculations have been performed using the formalism of density-functional theory as implemented in the software package **exciting** [32]. For the β phase, we used the PBEsol functional [40] of the generalized gradient approximation for the exchange-correlation energy.[1] Numerical integration in reciprocal space was performed using a 6×6×6 $\boldsymbol{k}$-grid and the number of basis functions was set by the value of the parameter `rgkmax` to 9.0.[2] For the α phase, the ground-state optimized structure used in this work has been taken from the calculations reported in Ref. [51], which also employed the PBEsol functional.

The volume optimization procedure leads to the lattice parameters illustrated in Tables 4.1 and 4.2, for the β and α phase, respectively. For the β phase, the values of the lattice parameter b and c as well as the angle β are in good agreement with the available results displayed in Table 4.1 and of Refs. [21, 52, 53]. Our calculated values for the lattice parameter a and the conventional-cell volume are, nevertheless, slightly larger than in the experiment of Ref. [54]. The experimental and theoretical parameters for the α phase shown in Table 4.2 and of Refs. [21, 52, 53] are generally very similar among them.

[1] Explicit examples of the input files for **exciting** calculations of structure optimizations are given in Appendix A.1. The species files defining the basis-function type used in all calculations can be found in Appendix A.2.

[2] The parameter `rgkmax` is defined as the product $R_{\mathrm{MT}}\, G_{\mathrm{max}}$ and discussed in Section 3.1.

TABLE 4.1: Optimized lattice parameters a, b, c, β, and conventional-cell volume Ω for the monoclinic structure of β-Ga_2O_3 in comparison with available experimental and theoretical data. In the brackets, we specify the type of the exchange-correlation functional, which was used in the theoretical works.

		`exciting` (PBEsol)	Expt. [54]	Theor. [55] (PBE)	Theor. [56] (LDA)	Theor. [25] (AM05)
a	[Å]	12.29	12.21	12.31	12.23	12.29
b	[Å]	3.05	3.04	3.08	3.04	3.05
c	[Å]	5.82	5.80	5.89	5.80	5.81
β	[°]	103.7	103.8	103.9	103.7	103.8
Ω	[Å^3]	211.92	208.85	216.80	209.50	210.44

TABLE 4.2: Optimized lattice parameters, a_h and c_h, and conventional-cell volume Ω for the hexagonal structure of α-Ga_2O_3 of Ref. [51] in comparison with available experimental and theoretical data. In the brackets, we specify the type of the exchange-correlation functional, which was used in the theoretical works.

		Theor. [51] (PBEsol)	Expt. [31]	Theor. [24] (LDA)	Theor. [23] (LDA)	Theor. [25] (AM05)
a_h	[Å]	5.01	4.98	5.00	5.01	5.00
c_h	[Å]	13.47	13.43	13.41	13.41	13.45
Ω	[Å^3]	292.85	288.45	290.34	291.50	291.20

4.2 Lattice-dynamical properties

In this section, we focus on results for the lattice-dynamical properties of the two investigated phases of Ga_2O_3. A symmetry analysis of Γ-point phonon modes is presented in Section 4.2.1, followed by the results for the Γ phonons of β- and α-Ga_2O_3 in Section 4.2.2 and 4.2.3, respectively.

4.2.1 Symmetry analysis of Γ-point phonon modes

As mentioned in Section 4.1.1, the space group of β-Ga_2O_3 is C2/m (C^3_{2h}). Considering this geometry, group-theoretical methods allow us to classify the 27 optical phonon modes at the Γ point according to their irreducible representation as [57]

$$\Gamma^{(\beta)}_{\text{optical}} = 10\,A_g + 5\,B_g + 4\,A_u + 8\,B_u\ . \tag{4.2.1}$$

The modes with even parity (g) are Raman active and non-polar, whereas the phonon modes with odd parity (u) are infrared active and polar. It follows that in total 15 phonon modes are Raman active and, additionally, are not affected by the LO-TO

splitting introduced in Section 2.3.2. None of these phonon modes possess degeneracy, as it is predicted by group theory. This is a consequence of the strong present anisotropy of this crystal structure. At this point, it is also worth to discuss the result of a group-theoretical analysis of the general symmetry of the Raman tensors of the modes A_g and B_g. For the β phase , these Raman tensors have the following form

$$\mathscr{B}(A_g) = \begin{bmatrix} a & d & 0 \\ d & b & 0 \\ 0 & 0 & c \end{bmatrix} \quad \text{and} \quad \mathscr{B}(B_g) = \begin{bmatrix} 0 & 0 & e \\ 0 & 0 & f \\ e & f & 0 \end{bmatrix}, \tag{4.2.2}$$

where $\{a, b, ..., f\}$ are the parameters to be determined.

The application of group theory to the symmetry of α-Ga_2O_3 yields the irreducible representation of the 27 optical phonon modes at Γ for this phase [23, 50]

$$\Gamma^{(\alpha)}_{\text{optical}} = 2A_{1g} + 2A_{1u} + 3A_{2g} + 2A_{2u} + 5E_g + 4E_u \,, \tag{4.2.3}$$

where only the A_{1g} and E_g modes are Raman active. Furthermore, the modes E_g and E_u are double degenerate. Similar to the β phase, the Raman active modes are non-polar and, therefore, no effects of LO-TO splitting have to be taken into account in the Raman calculations. The predicted symmetries for the Raman tensors for both mode types are [23, 57]

$$\mathscr{B}(A_{1g}) = \begin{bmatrix} a & 0 & 0 \\ 0 & a & 0 \\ 0 & 0 & b \end{bmatrix} \quad \text{and} \quad \mathscr{B}(E_g) = \begin{bmatrix} c & 0 & 0 \\ 0 & -c & d \\ 0 & d & 0 \end{bmatrix}, \begin{bmatrix} 0 & -c & -d \\ -c & 0 & 0 \\ -d & 0 & 0 \end{bmatrix}. \tag{4.2.4}$$

Here, we notice the two different representations for the two degenerate E_g modes.

4.2.2 Γ phonons of β-Ga_2O_3

For the *ab initio* calculations of the Γ phonons of β-Ga_2O_3, we used a $1\times1\times1$ supercell and the same computational parameters as for the ground-state relaxation in Section 4.1.2.[3] The resulting phonon frequencies are shown in Tables 4.3 and 4.4 for the Raman-active and polar phonon modes, respectively. The optical phonon frequencies are in a range between 100 and 735 cm^{-1}. In general, our calculated frequencies of the Raman-active modes are in good agreement with other theoretical values, as well as with experimental data. The frequency differences for most of the modes amount to less than 12 cm^{-1}, except for the modes $A_g^{(7)}$ and $A_g^{(10)}$, for which the experimental results, as well as some calculations (Ref. [22, 55]), show significant deviations of about

[3] An explicit example of the input file for an `exciting` calculation of Γ-point phonons is given in Appendix A.1. This setup of numerical parameters guarantees an accuracy of about 1 cm^{-1} of the calculated phonon frequencies.

TABLE 4.3: The 15 optical Raman-active (and non-polar) phonon modes of β-Ga_2O_3 in comparison with other theoretical and eperimental values. All frequencies are given in units of cm^{-1} and the numerical values are rounded to an integer value. In the experimental data of Ref. [22] not all modes have been determined or observed. In the brackets we specify the type of the exchange-correlation functional, which was used in the theoretical works.

	`exciting` (PBEsol)	Expt.* [28]	Expt. [22]	Theor. [22] (LDA)	Theor. [58] (PBE)	Theor. [55] (LDA)
$A_g^{(1)}$	105	111	110	104	104	105
$A_g^{(2)}$	159	170	169	165	160	164
$A_g^{(3)}$	187	200	200	205	186	202
$A_g^{(4)}$	305	320	319	317	311	316
$A_g^{(5)}$	331	347	346	346	344	340
$A_g^{(6)}$	381	416	416	418	376	420
$A_g^{(7)}$	446	475	-	467	456	459
$A_g^{(8)}$	602	630	-	600	620	607
$A_g^{(9)}$	632	658	629	626	644	656
$A_g^{(10)}$	733	767	764	732	745	758
$B_g^{(1)}$	108	115	114	113	105	112
$B_g^{(2)}$	140	145	145	149	145	141
$B_g^{(3)}$	337	353	-	356	351	348
$B_g^{(4)}$	463	475	474	474	473	473
$B_g^{(5)}$	638	652	653	637	645	627

* The data of Ref. [28] are assumed as reference in the discussion in Section 4.4.1.

35 - 40 cm^{-1}. Moreover, most of the experimental values are slightly higher than the calculated frequencies. A possible explanation for this discrepancy is the difference of the value of the conventional-cell volume (see Table 4.1) obtained by our calculations and the experimental one. Differences with other calculations could be due to the choice of different approximations for the exchange-correlation functional. In some cases, the PBEsol functional can lead to an overestimation of the bond lengths. This overestimation leads to a weakening of the interatomic force constants and, therefore, to a reduction of the vibrational energies [30].

The determination of the Raman-active modes shown in Table 4.3 is one of the fundamental ingredients for the Raman calculations described in Section 4.4. In addition to these Raman-active modes, we also investigated the polar zone-center modes of β-Ga_2O_3. These 12 modes are shown in Table 4.4 and are also in good agreement with the other presented values. The frequency values shown in Table 4.4 belong to the transverse-optical (TO) modes at $\boldsymbol{q} = 0$. In order to obtain longitudinal-optical (LO)

TABLE 4.4: Same as Table 4.3 for the 12 polar transverse-optical phonon modes (A_u and B_u) of β-Ga_2O_3. In the brackets we specify the type of the exchange-correlation functional, which was used in the theoretical works.

	`exciting` (PBEsol)	Theor. [51] (PBE)	Theor. [58] (LDA)	Theor. [55] (PBE)	Expt. [59]
$A_u^{(1)}$	147	148	146	142	155
$A_u^{(2)}$	287	296	303	296	297
$A_u^{(3)}$	440	439	448	385	449
$A_u^{(4)}$	648	643	653	647	663
$B_u^{(1)}$	188	187	176	188	214
$B_u^{(2)}$	245	246	244	252	262
$B_u^{(3)}$	268	269	272	265	279
$B_u^{(4)}$	343	345	347	344	357
$B_u^{(5)}$	407	415	423	411	433
$B_u^{(6)}$	549	551	567	574	573
$B_u^{(7)}$	661	663	676	673	692
$B_u^{(8)}$	714	715	726	742	744

phonons, polarization effects have to be taken into account. This leads to the inclusion of the non-analytical correction of Eq. (2.3.13), which requires the knowledge of the Born effective charge (BEC) and high-frequency dielectric tensors. For the β phase, the calculated BEC tensors of the five inequivalent atoms are the following

$$
\begin{aligned}
Z_{\mathrm{Ga1}} &= \begin{bmatrix} 3.24 & 0.00 & 0.34 \\ 0.00 & 3.44 & 0.00 \\ 0.18 & 0.00 & 3.12 \end{bmatrix}, \qquad Z_{\mathrm{Ga2}} = \begin{bmatrix} 2.74 & 0.00 & -0.28 \\ 0.00 & 2.89 & 0.00 \\ -0.16 & 0.00 & 3.07 \end{bmatrix}, \\
Z_{\mathrm{O1}} &= \begin{bmatrix} -2.24 & 0.00 & 0.21 \\ 0.00 & -1.97 & 0.00 \\ 0.24 & 0.00 & -2.30 \end{bmatrix}, \qquad Z_{\mathrm{O2}} = \begin{bmatrix} -1.44 & 0.00 & -0.06 \\ 0.00 & -2.10 & 0.00 \\ -0.03 & 0.00 & -2.50 \end{bmatrix}, \\
Z_{\mathrm{O3}} &= \begin{bmatrix} -2.29 & 0.00 & -0.21 \\ 0.00 & -2.27 & 0.00 \\ -0.23 & 0.00 & -1.38 \end{bmatrix}.
\end{aligned}
\tag{4.2.5}
$$

These values of the effective-charge tensors have been calculated by S. Tillack [60] using the Berry-phase method described in Chapter 3 of Ref. [61]. This calculation has been performed with the same computational parameters used along this thesis. All tensors in Eq. (4.2.5) possess off-diagonal elements, which are, however, small

compared to the diagonal ones. The BEC tensors are neither diagonal nor symmetric, which reflects the strong anisotropy of the crystal structure. The inequivalent Ga atoms, which are located either in a tetrahedral or octahedral coordination (see Figure 4.1), have pronounced differences in the magnitude of the diagonal elements of the BEC tensor. The difference between the BEC tensors for the inequivalent O atoms is less pronounced as for the Ga atoms.

In order to calculate the LO phonon modes, the high-frequency dielectric tensor $\boldsymbol{\epsilon}^{\infty}$ is also required, see Eq. (2.3.13). For the monoclinic crystal structure of the β phase, the dielectric tensor possesses four inequivalent non-zero tensor elements ($\epsilon_{xx} \neq \epsilon_{yy} \neq \epsilon_{zz} \neq \epsilon_{xy} = \epsilon_{yx}$) [59]. The tensor which we used for the calculation of the LO phonons is

$$\epsilon^{\infty}_{(\mathrm{RPA})} = \begin{bmatrix} 3.315 & 0.100 & 0.000 \\ 0.100 & 3.235 & 0.000 \\ 0.000 & 0.000 & 3.340 \end{bmatrix}. \tag{4.2.6}$$

The explicit calculation of $\epsilon^{\infty}_{(\mathrm{RPA})}$ is discussed in detail in Section 4.3.1.

The calculated values of the LO phonons for the direction of $\boldsymbol{q}$ parallel to $\boldsymbol{a}$, $\boldsymbol{b}$, and $\boldsymbol{c}$ are shown in Table 4.5 and compared with the theoretical values of Ref. [58]. The corresponding TO modes were already shown in Table 4.4. For the analysis of the LO phonons, we, first, discuss the calculated values of our work for the three $\boldsymbol{q}$ directions and, second, compare our results with the calculated values of Ref. [58]. According to our calculation, the behaviour of the LO-TO splitting for the $\boldsymbol{q} \parallel \boldsymbol{b}$ direction differs clearly from the results along the vectors $\boldsymbol{a}$ and $\boldsymbol{c}$. In this case, only the four A_u modes contribute to the splitting and the eight B_u modes remain unchanged. For $\boldsymbol{q}$ along the $\boldsymbol{a}$ and $\boldsymbol{c}$ directions the opposite happens. This behaviour is explained in the next paragraph in terms of the mode-related effective charges. The comparison with Ref. [58] shows generally good agreement for the $\boldsymbol{b}$ and $\boldsymbol{c}$ direction. However, it reveals a discrepancy for the direction $\boldsymbol{q} \parallel \boldsymbol{a}$, for which in Ref. [58] all modes exhibit a LO-TO splitting, whereas in our calculations this holds only for the the B_u modes. This is confirmed by a direct analysis of the LO-TO splitting defined as $\Delta\omega_{\text{LO-TO}} = \omega_{\text{LO}} - \omega_{\text{TO}}$, shown in Table 4.6. Only the splitting of mode $B_u^{(8)}$ for $\boldsymbol{q} \parallel \boldsymbol{c}$ is significantly larger. The small abberations for the $\boldsymbol{b}$ and $\boldsymbol{c}$ directions can be possibly explained by the use of different codes and exchange-correlation functionals, whereas the major discrepancy along the $\boldsymbol{a}$ direction is most-likely related to an unintended wrong choice of the $\boldsymbol{q}$ direction in the calculations of Ref. [58].

Before proceeding to the optical properties, the mode-related effective charges and the reflectivity $R(\omega)$, which were introduced in Eqs. (2.3.16) and (2.3.17), respectively, are calculated for the $\boldsymbol{q}$-direction along the three basis lattice vectors. The obtained values of the mode-related effective charges are shown in Table 4.7. According to Eqs. (2.3.13) and (2.1.16), only those phonon modes participate in the LO-TO splitting, which have a non-zero scalar product between the mode effective-charge vector

TABLE 4.5: Optical polar phonon modes of β-Ga_2O_3 including the frequency values of the TO and corresponding LO modes for the directions of $\boldsymbol{q}$ along the three basis lattice vectors of the conventional cell. All frequencies are given in units of cm^{-1}.

Mode	exciting				Theor. [58]			
	TO	LO			TO	LO		
	$\boldsymbol{q}=0$	$\boldsymbol{q}\parallel\boldsymbol{a}$	$\boldsymbol{q}\parallel\boldsymbol{b}$	$\boldsymbol{q}\parallel\boldsymbol{c}$	$\boldsymbol{q}=0$	$\boldsymbol{q}\parallel\boldsymbol{a}$	$\boldsymbol{q}\parallel\boldsymbol{b}$	$\boldsymbol{q}\parallel\boldsymbol{c}$
$A_u^{(1)}$	147	-	148	-	146	146*	146*	-
$A_u^{(2)}$	287	-	333	-	303	307	343	-
$A_u^{(3)}$	440	-	553	-	448	487	547	-
$A_u^{(4)}$	648	-	770	-	653	655	742	-
$B_u^{(1)}$	188	191	-	240	176	178	-	230
$B_u^{(2)}$	245	265	-	259	244	265	-	252
$B_u^{(3)}$	268	281	-	268	272	277	-	272*
$B_u^{(4)}$	343	358	-	347	347	359	-	353
$B_u^{(5)}$	407	471	-	438	423	445	-	448
$B_u^{(6)}$	549	614	-	654	567	617	-	667
$B_u^{(7)}$	661	711	-	680	676	721	-	687
$B_u^{(8)}$	714	761	-	785	726	747	-	764

* The values only differ in the decimal place.

and the $\boldsymbol{q}$-direction vector. This explains the behaviour of the modes A_u along the direction $\boldsymbol{b}$ and also the change of the modes B_u along the directions $\boldsymbol{a}$ and $\boldsymbol{c}$.

The calculated reflectivity spectra are shown in Figure 4.3. The spectra for $\boldsymbol{q}\|\boldsymbol{b}$ and $\boldsymbol{q}\|\boldsymbol{c}$ are in good agreement with the experimental data of Ref. [62]. The calculated reflectivity never reaches 100%, due to the included damping. The spectrum for $\boldsymbol{q}\|\boldsymbol{a}$ shows strong increases in the reflectivity at the TO frequencies of the B_u modes and decreases at the corresponding LO frequencies. Therefore, the extension of the *plateaus* of high reflectivity (*i.e.*, the flat regions around the maxima) beyond the corresponding TO frequency peaks depends on the magnitude of $\Delta\omega_{\text{LO-TO}}$. In particular, a small LO-TO splitting yields a small plateau, as it is for the modes $B_u^{(1)}$, $B_u^{(3)}$, $B_u^{(4)}$, and $B_u^{(8)}$, while the opposite happens for larger phonon-mode splittings. The results of Tables 4.5 and 4.6 confirm these findings. The same argumentation holds for the reflectivity spectra of for $\boldsymbol{q}\|\boldsymbol{b}$ and $\boldsymbol{q}\|\boldsymbol{c}$. For $\boldsymbol{q}\|\boldsymbol{b}$, we identify four *plateaus* of high reflectivity, produced by the A_u modes, while there are eight *plateaus* due to the B_u modes in the direction for which $\boldsymbol{q}$ is parallel to $\boldsymbol{c}$.[4]

[4] Actually, only 7 *plateaus* appear in the spectrum, because the modes $B_u^{(1)}$ and $B_u^{(2)}$ overlap and contribute both to the first plateau.

TABLE 4.6: Absolute values of the LO-TO splitting, $\Delta\omega_{\text{LO-TO}}$, of the optical polar phonon modes of β-Ga_2O_3 for the directions of $\boldsymbol{q}$ along the three basis lattice vectors of the conventional cell. All frequencies are given in units of cm^{-1}.

$\Delta\omega_{\text{LO-TO}}$	`exciting`			Theor. [58]		
	$\boldsymbol{q} \parallel \boldsymbol{a}$	$\boldsymbol{q} \parallel \boldsymbol{b}$	$\boldsymbol{q} \parallel \boldsymbol{c}$	$\boldsymbol{q} \parallel \boldsymbol{a}$	$\boldsymbol{q} \parallel \boldsymbol{b}$	$\boldsymbol{q} \parallel \boldsymbol{c}$
$A_u^{(1)}$	-	1	-	<1	<1	-
$A_u^{(2)}$	-	46	-	4	40	-
$A_u^{(3)}$	-	113	-	39	99	-
$A_u^{(4)}$	-	122	-	2	89	-
$B_u^{(1)}$	3	-	52	2	-	54
$B_u^{(2)}$	20	-	14	21	-	8
$B_u^{(3)}$	13	-	<1	5	-	<1
$B_u^{(4)}$	15	-	4	12	-	6
$B_u^{(5)}$	64	-	24	22	-	25
$B_u^{(6)}$	65	-	105	50	-	100
$B_u^{(7)}$	50	-	19	45	-	11
$B_u^{(8)}$	47	-	71	21	-	38

TABLE 4.7: Mode-related effective-charge vectors for the optical polar phonon modes at the Γ point of β-Ga_2O_3, without including LO-TO splitting. We remind that, according to Eq. (4.1.1), the basis lattice vector $\boldsymbol{a}$ ($\boldsymbol{b}$) is parallel to the x (y) direction.

	A_u				B_u							
	1	2	3	4	1	2	3	4	5	6	7	8
$\tilde{Z}_x$	-	-	-	-	0.79	3.08	0.82	-2.92	3.23	-3.10	2.23	0.48
$\tilde{Z}_y$	0.57	-3.26	-4.36	-3.19	-	-	-	-	-	-	-	-
$\tilde{Z}_z$	-	-	-	-	-2.86	0.17	0.31	0.63	3.41	3.88	1.21	1.80

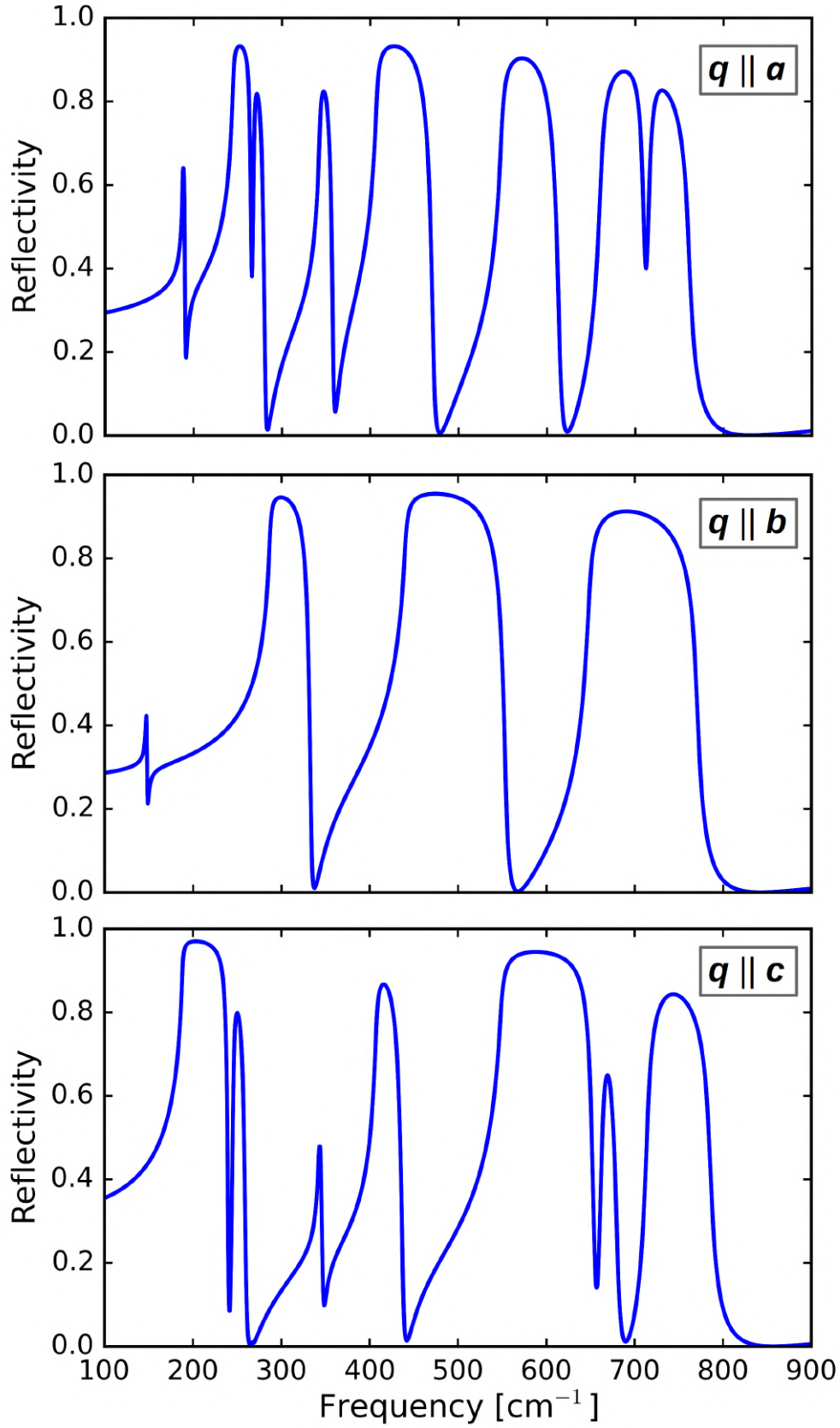

FIGURE 4.3: Reflectivity spectra for the $q \parallel a$, $q \parallel b$, and $q \parallel c$ direction in the frequency range between 100 and 900 cm^{-1}. The reflectivity is calculated using Eq. (2.3.17). For a better comparison with the experimental spectra, a damping is included in the theoretical curves.

TABLE 4.8: Optical, Raman-active, and non-polar phonon modes of α-Ga_2O_3 in comparison with available experimental and theoretical values. All frequencies are given in units of cm^{-1} and rounded to an integer value. In the brackets we specify the type of the exchange-correlation functional, which was used in the theoretical works.

	`exciting` (PBEsol)	Theor. [22] (LDA)	Theor. [23] (LDA)	Expt. [23]	Expt. [22]	Expt. [31]
$A_{1g}^{(1)}$	210	215	211	218	217	218
$A_{1g}^{(2)}$	544	551	551	570	573	574
$E_g^{(1)}$	228	239	233	241	241	242
$E_g^{(2)}$	281	281	281	285	286	287
$E_g^{(3)}$	323	344	314	329	329	328
$E_g^{(4)}$	410	410	426	431	432	431
$E_g^{(5)}$	650	680	667	687	688	688

4.2.3 Γ phonons of α-Ga_2O_3

For the α phase, we only focus on the Raman-active modes A_{1g} and E_g. Results for the polar phonon modes can be found in Ref. [51]. For the calculations of the Γ phonons, we used the same computational parameters as in Ref. [51]. The resulting phonon frequencies are in the range of 200 to 650 cm^{-1} and, thus, slightly lower than the phonon modes of the β phase. Moreover, the E_g modes are double degenerate, which is also a novelty towards the β phase.

The calculated values, presented in Table 4.8, are generally in good agreement with the other available theoretical and experimental results, besides a light underestimation of some modes. In particular, this can be seen for the $A_{1g}^{(2)}$, $E_g^{(4)}$, and $E_g^{(5)}$ modes, which exhibit a larger difference to the experimental values. These differences are possibly related to the slightly larger conventional-cell volume in Table 4.2 in comparison to the experimental values of Refs. [31, 23].

4.3 Optical properties

This section deals with the optical properties of Ga_2O_3, more precisely with the calculation of the frequency-dependent dielectric function, which is a key ingredient to calculate Raman spectra. We start with the dielectric tensor of the β phase in Section 4.3.1, followed by the α phase in Section 4.3.2. Finally, we discuss the impact of excitonic effects in Section 4.3.3.

4.3.1 Dielectric tensor of β-Ga_2O_3

The frequency-dependent dielectric tensor of β-Ga_2O_3 is calculated here using the random-phase approximation (RPA) in the framework of time-dependent density-functional theory (TDDFT) as presented in Section 2.4.1. Our computations[5] are performed using $8\times8\times8$ $\boldsymbol{k}$- and $\boldsymbol{q}$-point grids, including 65 empty states, limiting the number of basis functions by setting the value of `rgkmax` to 7.0, and setting the value of the cutoff parameter `gqmax`[6] to 3.0. We fixed the value of the scissor shift[7] to 2.6 eV in order to approach the experimental bandgap of about 4.9 eV [9, 10].

The calculated high-frequency dielectric tensor, $\boldsymbol{\epsilon}^{\infty}_{(\mathrm{RPA})}$, was already shown in Eq. (4.3.1) and used in order to compute the LO phonons and the reflectivity in Section 4.2.1. The tensor $\boldsymbol{\epsilon}^{\infty}_{(\mathrm{RPA})}$ shows the expected symmetry for a monoclinic crystal structure. Its off-diagonal elements are about one order of magnitude smaller than the diagonal ones. The pronounced difference between the tensor elements is related to the monoclinic crystal structure and its resulting anisotropy. For a better comparison with previous experimental and theoretical works, we introduce the averaged high-frequency dielectric constant, which is defined as $\bar{\epsilon}^{\infty} = 1/3\,\mathrm{Tr}\,\boldsymbol{\epsilon}^{\infty}$. Available theoretical values for $\bar{\epsilon}^{\infty}$ are 3.91 [55], 3.50 [52], and 3.55 [25]. These results are slightly larger but, nonetheless, in satisfactory agreement with our value of $\bar{\epsilon}^{\infty}_{(\mathrm{RPA})} = 3.30$. Moreover, the experimental values, 3.57 [63] and 3.53 [59], are also quite close to ours.

As concerns the results for the frequency-dependent dielectric function, we focus our attention on the region of frequencies which lie below up to slightly above the fundamental gap.[8] Figure 4.4 shows the imaginary part of the dielectric tensor in an energy window between 4.4 and 6.0 eV. Notice, here, that in this and the following figures of this section, the frequency dependence is expressed through the corresponding energy dependence (with the energy given in eV). In the literature, this is the standard procedure used in for presenting optical spectra. As can be seen in Figure 4.4, the absorption onsets in the xx, yy, and zz polarization can be found at 4.7, 4.8, and 5.3 eV, respectively. Similar behaviour is also reported in available theoretical investigations computed at different levels of approximation; the Bethe-Salpether equation and *independent-particle* (IP) approximation[9] in Ref. [25, 64], the IP calculations of Ref. [65], and the *electric-dipole* approximation in Ref. [56]. Despite a different choice of the reference Cartesian coordinate system in those works, where the diagonal tensor elements are in a different order ($xx \to yy$, $yy \to zz$, and $zz \to xx$), the spectra show the same main features as our calculations.

[5] An `exciting` input file for a TDDFT calculation can be found in Appendix A.1. This setup of numerical parameters guarantees an accuracy of about 1% of the high-frequency dielectric tensor.

[6] The cutoff parameter `gqmax` sets the maximum value of the quantity $|\boldsymbol{G}+\boldsymbol{q}|$. This establishes a constraint for the Kohn-Sham response function, the screening, and the Coulomb potential.

[7] The scissor-operator approximation is introduced in Section 4.2.4.

[8] In this frequency range are the laser energies used in typical Raman experiments.

[9] This approximation neglects electron interactions and, therefore, no local-field effects are included.

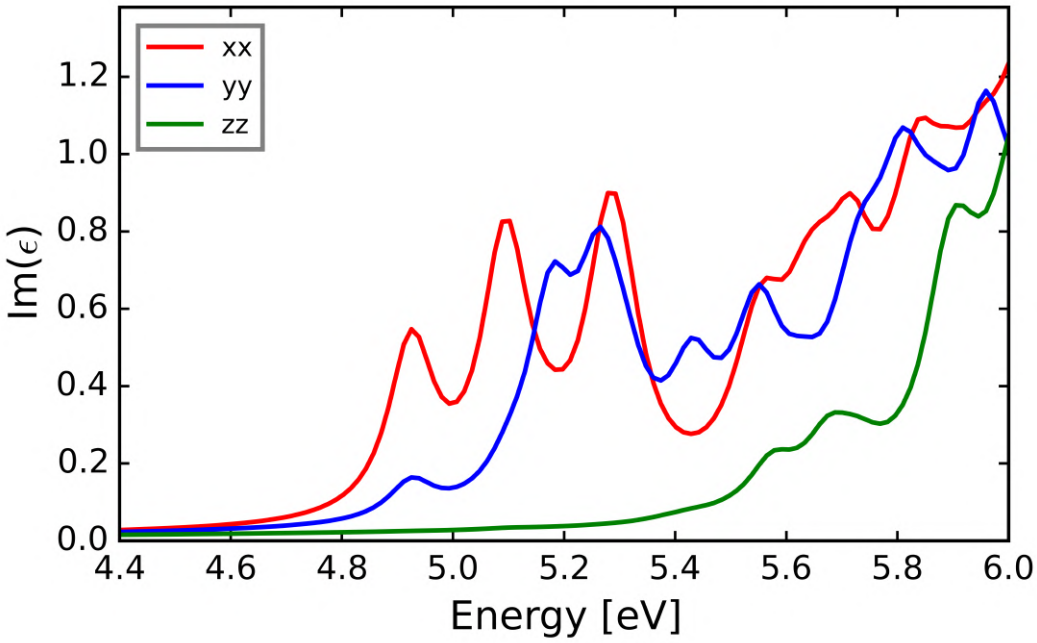

FIGURE 4.4: Results of RPA calculations of the imaginary part of the dielectric tensor of β-Ga_2O_3 in the vicinity of the absorption edge for the xx, yy, and zz polarization.

4.3.2 Dielectric tensor of α-Ga_2O_3

For α-Ga_2O_3 in the hexagonal representation, $\boldsymbol{\epsilon}(\omega)$ is a diagonal tensor and contains the tensor elements $\epsilon_{xx} = \epsilon_{yy} \neq \epsilon_{zz}$. Similar to β-Ga_2O_3, the dielectric tensor is computed within the random-phase approximation. The calculations are performed using $10\times10\times10$ $\boldsymbol{k}$- and $\boldsymbol{q}$-point grids, including 100 empty states, and setting the parameters `rgkmax` to 8.0 and `gqmax` to 2.0. We fixed the value of the scissor shift to 2.16 eV. The static limit yields the high-frequency dielectric tensor

$$\epsilon^{\infty}_{(\mathrm{RPA})} = \begin{bmatrix} 3.731 & 0.000 & 0.000 \\ 0.000 & 3.731 & 0.000 \\ 0.000 & 0.000 & 3.628 \end{bmatrix}, \tag{4.3.1}$$

which exhibits the expected symmetry for the α phase. Our averaged value of $\bar{\epsilon}^{\infty}_{(\mathrm{RPA})} = 3.70$ is in good agreement with the theoretical values of 3.71 [24], 3.80 [25], and 3.81 [52]. The experimental value of 3.69 [65] compares well with our calculation, too. In general, the high-frequency dielectric tensor of the α phase is supposed to be larger than the one of the β phase [65], as a consequence of the higher bandgap value of α-Ga_2O_3 of approximately 5.61 eV [24].

The imaginary part of $\boldsymbol{\epsilon}(\omega)$ in the energy window between 4.2 and 5.8 eV is shown in Figure 4.5. In this region, the fundamental absorption edge can be found. The spectra of the xx and yy polarization are identical by symmetry. This is a result of the hexagonal structure of the α phase. Only in the zz polarization, the dielectric functions exhibit small differences. The absorption onsets show a marginal difference

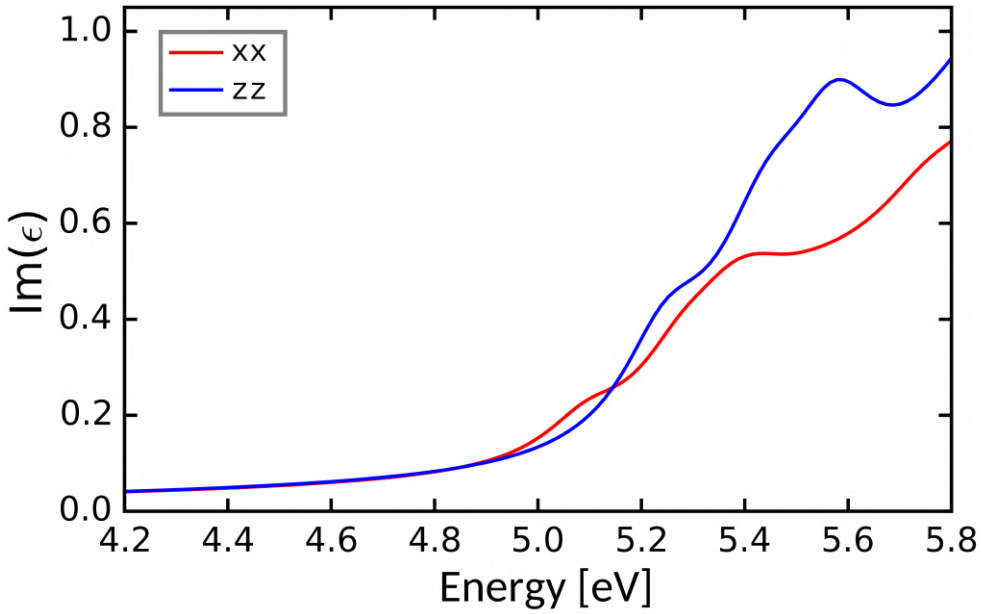

FIGURE 4.5: Results of RPA calculations of the imaginary part of the dielectric tensor of α-Ga_2O_3 in the vicinity of the bandgap for the xx and zz polarization.

of less than 100 meV between the xx and zz polarization. In contrast to β-Ga_2O_3, the two spectra of Figure 4.5 are very similar, which is directly related to the different crystal structures of the two phases. Our results for the onset behaviour of the dielectric tensor of α-Ga_2O_3 are also in good accordance with experimental [24] and theoretical references [24, 65].

4.3.3 Impact of excitonic effects

All results presented above are calculated within the RPA approximation, which does not include effects of the electron-hole coupling. In gallium oxide, excitonic effects are known to play an important role in the optical absorption, as it was discussed in Refs. [66, 67, 48]. To study the influence of excitonic effects on Raman spectra, we calculate the dielectric function by solving the Bethe-Salpether equation (BSE) in the framework of many-body perturbation theory as outlined in Section 2.4.2. For the calculation of the β phase, we used a $8\times8\times8$ $\boldsymbol{k}$-point and $\boldsymbol{q}$-point grid, included 100 empty states, and set the value of the parameters `rgkmax` to 7.0 and `gqmax` to 1.0. The BSE Hamiltonian is constructed by involving transitions between 10 occupied and 2 unoccupied states. The resulting BSE spectra of the real and imaginary part are presented in Figure 4.6 in comparison with our RPA spectra. As seen in both the imaginary and real part, excitonic effects are leading to the overall changes in the shape of the dielectric function, shifting the peaks, and moving the intensity distribution to lower energies.

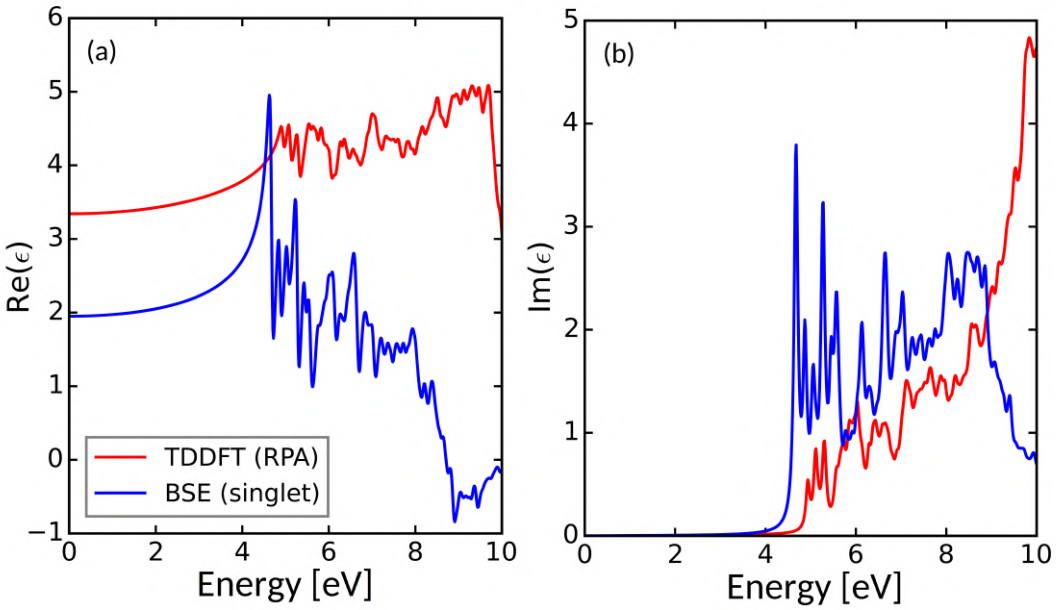

FIGURE 4.6: Results of RPA and BSE calculations of the real (a) and imaginary (b) part of the dielectric function of β-Ga_2O_3 in the xx polarization.

The high-frequency dielectric tensor of β-Ga_2O_3 from BSE calculations is

$$\epsilon^{\infty}_{(\mathrm{BSE})} = \begin{bmatrix} 1.945 & 0.265 & 0.000 \\ 0.265 & 1.883 & 0.000 \\ 0.000 & 0.000 & 1.746 \end{bmatrix}. \tag{4.3.2}$$

The averaged value of $\bar{\epsilon}^{\infty}_{(\mathrm{BSE})} = 1.858$ is about half of the RPA and experimental values discussed in Section 4.3.1. The reason for this large deviation is that our choice of the computational parameters is not accurate enough to get convergence for a BSE calculation of the dielectric function. In particular, to get a converged value of the real part, one has to include more unoccupied states in the construction of the BSE Hamiltonian. However, this enormously increases the computational costs, taken into account that we have to calculate the dielectric tensor for several deformed configurations and for each Raman-active phonon. This task could not be carried out in reasonable time. On the other hand, it was shown in Ref. [25] that the converged BSE dielectric functions in the low-energy region are in reasonable agreement with RPA calculations. That was the motivation for us, to use the RPA dielectric tensor in order to calculate the Raman tensors and spectra. As it will be discussed in Section 4.4, the agreement between the computed and measured Raman intensities suggests that excitonic effects do not play a significant role. A detailed investigation of excitonic effects on Raman spectra is beyond the scope of this thesis and could be topic of further investigation.

4.4 Raman tensors and polarized Raman spectra

Our results of the Raman tensors and polarized spectra for β- and α-Ga_2O_3 are presented in the Sections 4.4.1 and 4.4.2, respectively. In order to calculate the Raman tensors, we follow the approach given in Section 1.4, using five displaced configurations for obtaining the numerical derivative of $\epsilon(\omega)$ with respect to the normal coordinate Q_0.[10]

4.4.1 β-Ga_2O_3

For the calculation of the 15 Raman-active modes of β-Ga_2O_3, we fixed the applied laser energy to 2.33 eV (532 nm) and the temperature to 298.15 K. These values have been chosen in order to mimic the experimental off-resonant conditions of Ref. [28], which is, to the best of our knowledge, the only available work in the literature where the Raman tensors of β-Ga_2O_3 were investigated. The calculated tensor elements for the phonon modes A_g and B_g are presented in Tables 4.9 and 4.10, respectively, where they are compared with the experimental and theoretical data from Ref. [28]. The tensor elements of Tables 4.9 and 4.10 are normalized in such a way that the element a of

TABLE 4.9: Calculated Raman-tensor elements of β-Ga_2O_3 for the 10 A_g modes of β-Ga_2O_3 in comparison with the experimental and theoretical data of Ref. [28]. The tensor elements are normalized in such a way that the element a of the mode $A_g^{(10)}$ is set to 1000 and the other elements are accordingly scaled. The notation for the tensor elements is specified in Eq. (4.2.2).

	exciting				Expt. [28]				Theor. [28]			
A_g	a	b	c	d	a	b	$\lvert c \rvert$	d	a	b	c	d
1	36	-131	-25	15	19	-59	14	13	79	-70	21	9
2	211	229	-182	-7	100	146	119	0	142	214	150	-34
3	233	480	338	7	187	445	311	27	154	431	272	-16
4	185	229	145	145	111	147	135	128	124	113	154	146
5	527	164	371	15	441	111	320	-5	479	12	349	-18
6	280	182	265	160	357	289	338	158	320	358	293	146
7	153	-444	-324	-33	47	-300	327	-52	31	-369	-241	9
8	262	531	247	-138	59	393	240	-135	55	414	53	-164
9	425	87	65	284	408	77	118	325	468	61	21	364
10	1000	396	22	-298	1000	353	0	-283	1000	248	-191	-409

[10] In Appendix A.1, we give a typical input file for Raman-scattering calculations. This setup of numerical parameters guarantees a maximum absolute deviation of the values of the Raman-tensor elements of about 10 in the units used in Table 4.9.

TABLE 4.10: Calculated Raman-tensor elements of β-Ga_2O_3 for the 5 B_g modes of β-Ga_2O_3 in comparison with experimental and theoretical data of Ref. [28]. The tensor elements are normalized as specified in Table 4.9.

	`exciting`		Expt. [28]		Theor. [28]	
B_g	*e*	*f*	*e*	*f*	*e*	*f*
1	44	73	32	31	46	56
2	167	127	106	70	148	88
3	164	-105	-	-	238	-92
4	7	-240	-	-	12	-291
5	116	313	162	326	147	335

the mode $A_g^{(10)}$ mode is set to 1000 and the other elements are accordingly scaled. The overall agreement with the experiment for the A_g modes in Table 4.9 is quite good. Notice that in the experiment, it was not possible to determine the sign of the tensor element *c*, therefore, all experimental elements *c* are set to positive values. The comparison with the calculated Raman tensors of Ref. [28] shows a few noticeable differences, in particular, concerning the sign of the tensor elements *c* for the modes $A_g^{(1)}$, $A_g^{(2)}$, and $A_g^{(10)}$. When comparing these results, one should take into account that, at variance with the many-body TDDFT/RPA approach used in this work, the calculations of Ref. [28] employ the *coupled perturbed Hartree-Fock/Kohn-Sham* method [68], which is a purely DFT-KS approach at the independent-particle level.

The tensor elements *e* and *f* of the five B_g modes are presented in Table 4.10. For these modes, the agreement with the experiment and the calculations of Ref. [28] is similar to the case of phonon modes with the A_g symmetry. The modes $B_g^{(3)}$ and $B_g^{(4)}$ are not observed in the experiment, because the features in the spectra, which are related to these modes, are very weak and in most scattering setups too close to the overshadowing $A_g^{(5)}$ and $A_g^{(7)}$ peaks.

The knowledge of the Raman tensors enables the calculation of the Raman spectra for any configuration of polarizations. The Raman spectra which are presented here are obtained by inserting the calculated Raman tensors into Eq. (1.4.6) and by including a Lorentzian broadening for the sake of a better comparison with experiments. We calculated Raman spectra for two different light polarization configurations, in order to enable a comparison with the experimental setup and results of Ref. [28].[11] The spectra of the yy and x′y′ polarization are presented in Figure 4.7. The yy configuration is defined by the polarization vectors $\boldsymbol{e}_L = (0,1,0)$ and $\boldsymbol{e}_S = (0,1,0)$ of the incident and scattered light polarization, respectively. For this configuration, only Raman tensors with a non-zero yy element can contribute to the spectrum. Therefore,

[11] The two chosen polarizations do not include the tensor element *c* and, therefore, the experimental values of Ref. [28] can be also used to compute the Raman spectra.

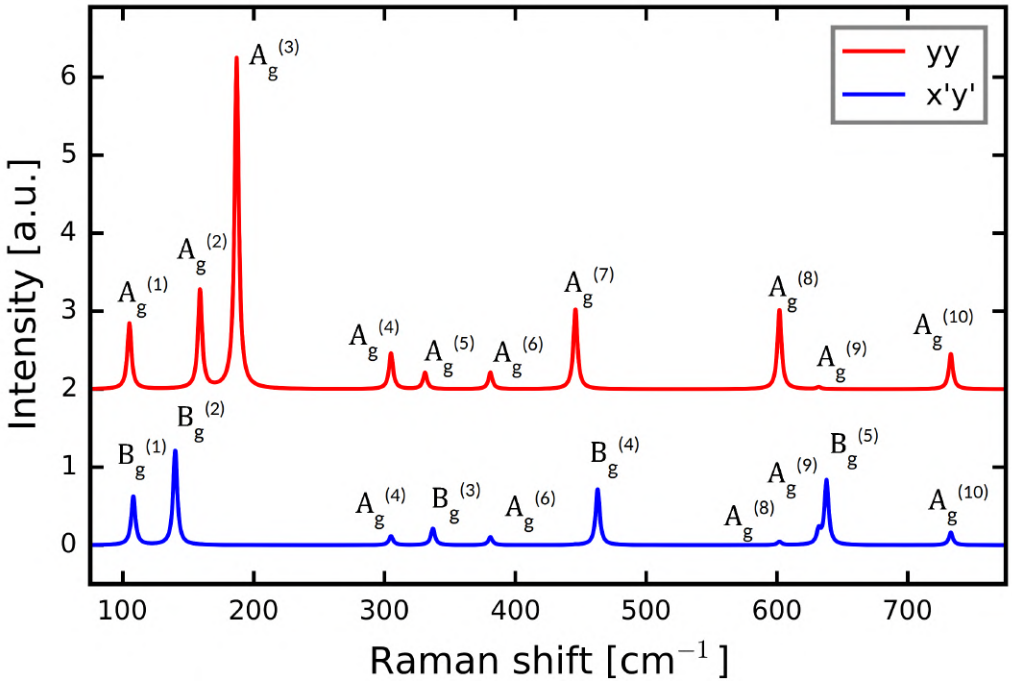

FIGURE 4.7: Calculated Raman spectra of β-Ga_2O_3 for the yy (red) and x′y′ (blue) polarization, with the corresponding polarization vectors e_L and e_S. See text for further details.

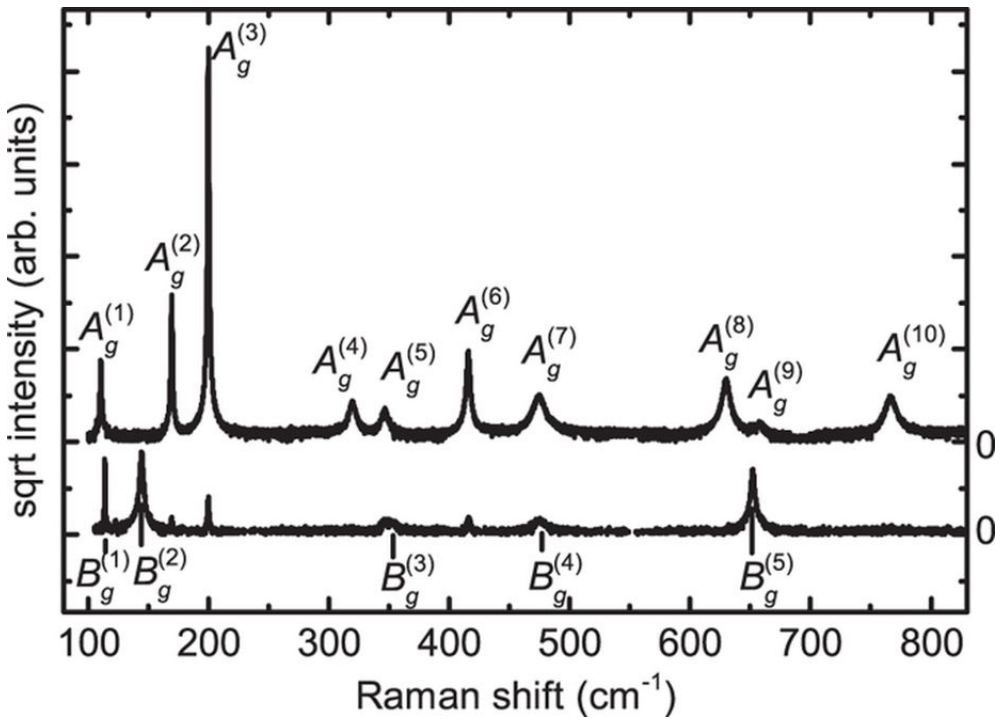

FIGURE 4.8: Polarized Raman spectra of β-Ga_2O_3 from Ref. [28] for the same configurations shown in Figure 4.7. This picture is taken from Ref. [28].

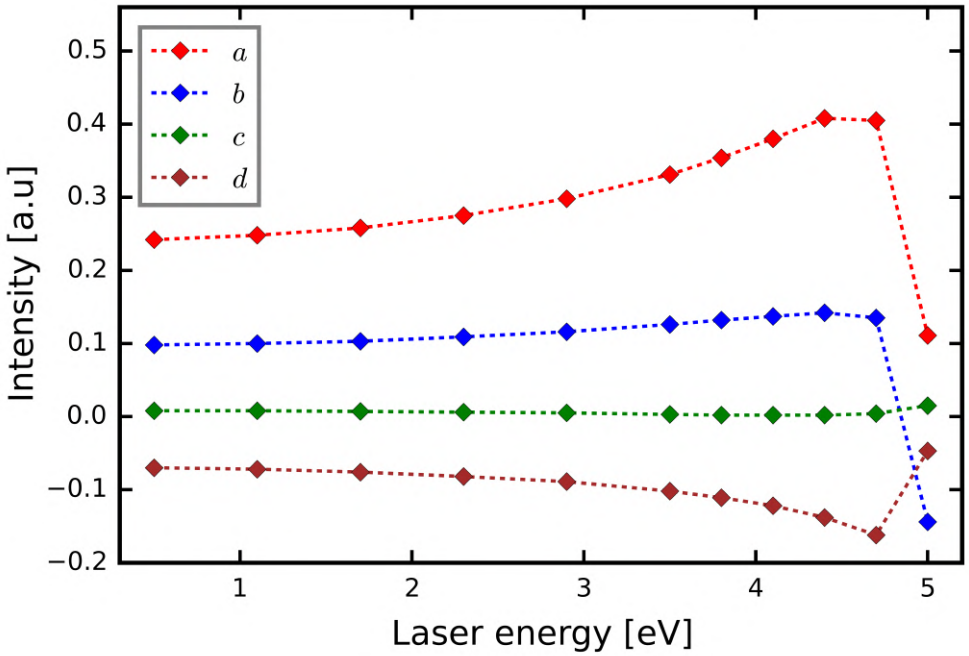

FIGURE 4.9: Dependence of the calculated Raman-tensor elements a, b, c, and d of the mode $A_g^{(10)}$ on different laser energies in the region between 0.5 and 5.0 eV.

all B_g modes are suppressed and only the A_g modes appear. The x′y′ polarization is defined by the polarization vectors $\boldsymbol{e}_L = (0,1,0)$ and $\boldsymbol{e}_S = (1,0,2)$. In contrast to the yy polarization, the B_g modes are no longer suppressed by symmetry in the x′y′ configuration.

For an easier comparison with the experiment, the measured polarized spectra of Ref. [28] are presented in Figure 4.8, too. In general, our calculated spectra show an overall good agreement with the experiment, considering both the positions of the peaks and their relative intensities. Moreover, polarized Raman spectra were also measured by Dohy *et al.* [30]. These measurements are in quite good accordance with our results for the yy polarization, considering the appearing phonon modes and their frequencies, but exhibit differences for the absolute peak intensities. Furthermore, experimental results of Ref. [29] show similar agreement for the yy configuration.

In their work, Kranert *et al.* [28] additionally measured the Raman spectra at a laser frequency of 3.8 eV and obtained the same results as in the case of 2.33 eV. In order to investigate the dependence of the Raman tensors on the laser energy, we focus our attention on the mode $A_g^{(10)}$ and vary the laser energy between 0.5 and 5 eV.[12] The results of the four non-zero tensor elements for this mode are shown in Figure 4.9. In general, all non-zero tensor elements (a, b, c, and d) show a similar behaviour in dependence on the laser energy. In the region far below the experimental bandgap

[12] This energy range includes the far off-resonant, as well as the band-gap region and even above.

of about 4.9 eV, all tensor elements show very slow variations. For laser energies between 3.5 and 4.5 eV, the variations, in particular for the a and d tensor elements, are significantly growing. For instance, the tensor element a increases of about 20% in the energy interval from 2.33 to 3.8 eV. However, the relative intensities between the four elements remains similar. Therefore, no noticeable changes could be observed in the experiment, since only relative intensities are measured. By approaching and exceeding the fundamental gap, the magnitude and the relative weight of the tensor elements a, b, and d changes drastically.

4.4.2 α-Ga_2O_3

In this section, we present and discuss our results of the Raman tensors and spectra of α-Ga_2O_3. We used the same computational procedure as for the Raman calculation of the β phase. In previous experimental works, laser energies of 2.33 [23, 31] and 2.41 eV [22] were employed. We chose 2.33 eV as laser energy to be consistent with the calculations of the β phase. Furthermore, both values of 2.33 and 2.41 eV are well below the fundamental gap of the α phase, then, we do not expect significant changes of the Raman tensors for these laser energies.

The calculated Raman tensors of the A_{1g} and E_g modes are shown in Table 4.11. Experimental and theoretical values of the Raman tensor elements are lacking and only experimental polarized Raman spectra are available. In our calculations, the $A_{1g}^{(2)}$ modes exhibits the highest intensity and the $E_g^{(1)}$ and $E_g^{(3)}$ modes are the lowest in magnitude. This has direct impact on the calculated polarized Raman spectra shown in Figure 4.10. For these spectra, we chose the polarization conditions already used in the experiments of Refs. [23, 31]. The calculated Raman spectra in Figure 4.10 include the xx, yy, and zz polarizations. Due to symmetry reasons, the xx and yy polarizations yield the exact same spectra, in which all 7 modes occur. In these configurations, only the tensor elements a and c contribute to the Raman efficiency. The intensity of the $A_{1g}^{(2)}$ is by far the highest and the $E_g^{(1)}$ mode is almost not visible, which is related to the magnitude of the corresponding tensor elements. In the zz spectrum, the E_g modes are

TABLE 4.11: Calculated Raman-tensor elements for the 2 A_{1g} and 5 E_g modes of α-Ga_2O_3. The tensor elements are normalized in such a way that the element b of the mode $A_{1g}^{(2)}$ is set to 1000 and the other elements are accordingly scaled. The notation of Eq. (4.2.4) is used.

Mode	$A_{1g}^{(1)}$	$A_{1g}^{(2)}$	$E_g^{(1)}$	$E_g^{(2)}$	$E_g^{(3)}$	$E_g^{(4)}$	$E_g^{(5)}$
a	610	-544	-	-	-	-	-
b	253	1000	-	-	-	-	-
c	-	-	49	242	115	-440	-516
d	-	-	77	505	115	16	110

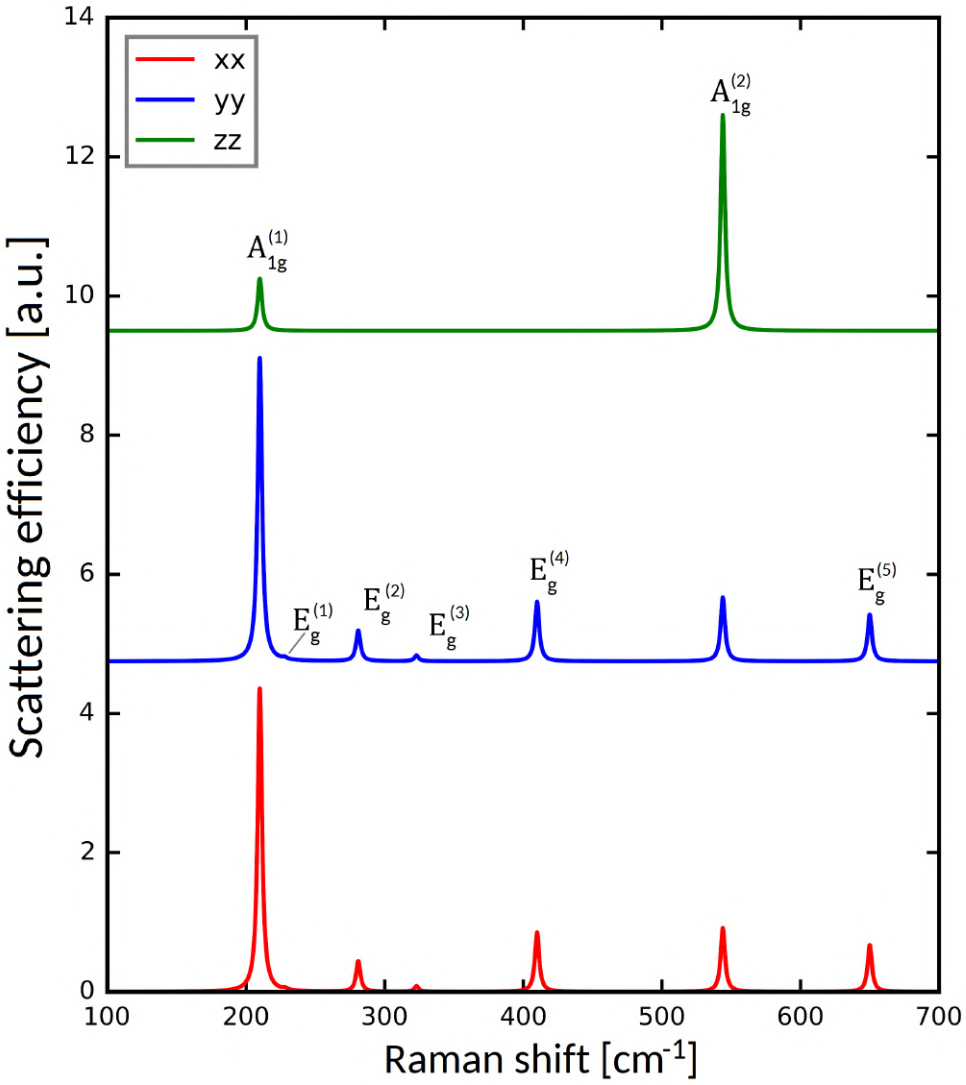

FIGURE 4.10: Calculations of Raman-scattering efficiency spectra of α-Ga_2O_3 for the polarizations xx (red), yy (blue), and zz (green). A Lorentzian broadening and an offset of 4.75 [a.u.] between the spectra are included.

suppressed by symmetry and only the modes $A_{1g}^{(1)}$ and $A_{1g}^{(2)}$ appear. This is confirmed by the experimental spectra [23, 31].[13] The calculated spectra for the xy and yz polarization are presented in Figure 4.11. Here, the A_{1g} modes are forbidden by symmetry and, therefore, only the E_g modes appear. The spectrum of the xy polarization shows five peaks corresponding to the five E_g modes. In the yz configuration, the $E_g^{(4)}$ is not visible. This is related to its very small tensor element d for this mode. Comparison to the experiments of Refs. [23, 31] shows also overall good agreement with our results for these two polarizations.

[13] For the sake of an easier comparison, the measured spectra [23, 31] are displayed in Appendix B.

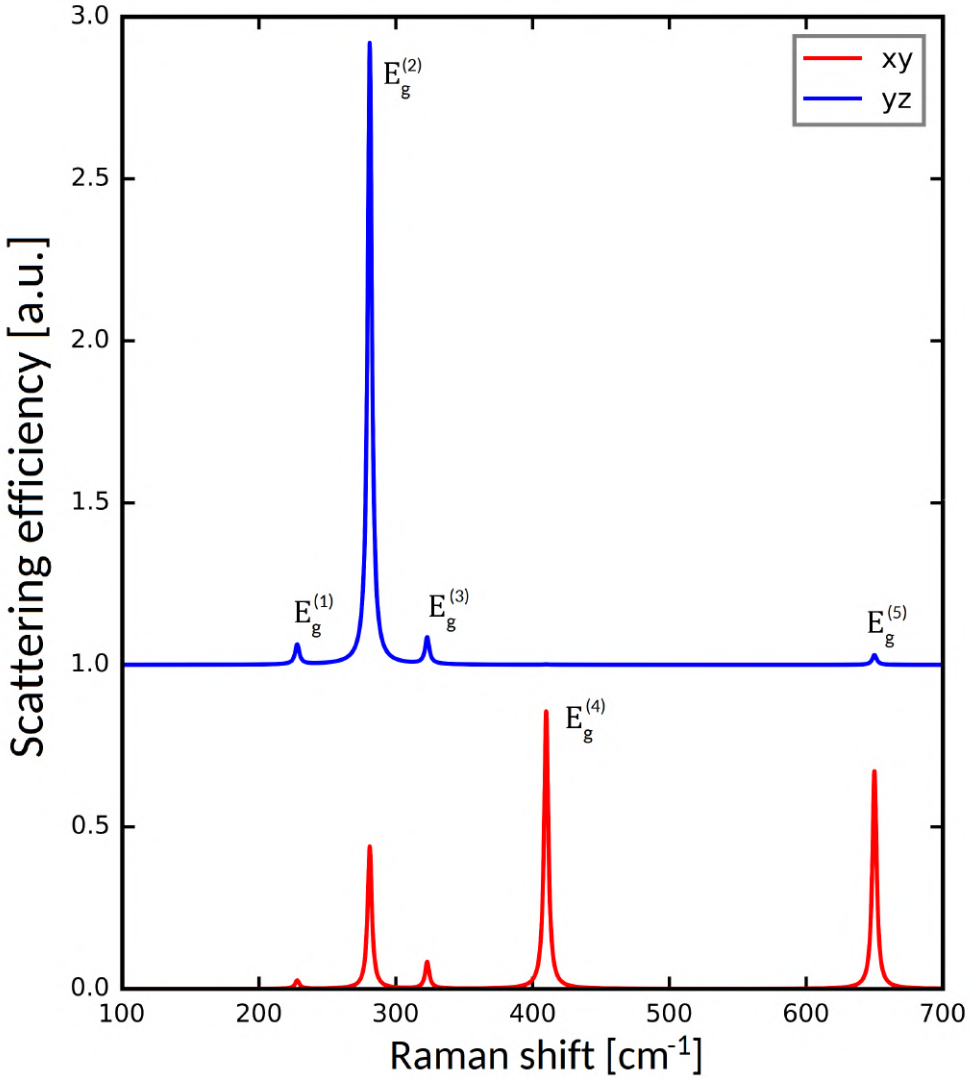

FIGURE 4.11: Same as Figure 4.10 for the polarizations (xy) (red) and (yz) (blue).

5. Conclusions and Outlook

In this thesis, we investigated the Raman tensors and spectra of β- and α-Ga_2O_3 by means of first-principles calculations. We started from the determination of the equilibrium crystal structure of both polymorphs. Then, we explored the lattice dynamics of the two phases, owing special attention to the characterization of the phonons at the Γ point. The peculiar properties of the polar phonon modes of the β phase were addressed, including LO-TO splitting and reflectivity spectra. Our results for the phonon frequencies were found in overall good agreement with experiments and other available calculations. For the optical properties, we focussed on the frequency-dependent dielectric tensor. As a result of the difference in the crystal structure, the two polymorphs have distinct values of the bandgap and the high-frequency dielectric tensor, and behave differently at the absorption onset.

The lattice-dynamical properties and the dielectric tensors were used as key ingredients for the Raman calculations. Polarized Raman spectra for α- and β-Ga_2O_3 were computed for several polarization configurations and compared to experimental results and previous calculations. We additionally studied the dependence of the Raman tensor of the β phase on the applied laser energies and found only weak dependence up to an energy of 3.5 eV. The explicit calculation of the Raman tensors allows us the computation of accurate Raman spectra for any desired polarization configuration for both of the studied polymorphs.

Our Raman calculations were performed using the random-phase approximation for the computation of the frequency-dependent dielectric tensor. This approximation does not include the electron-hole interaction, which is the necessary ingredient for the treatment of excitons. In fact, the impact of excitonic effects on our Raman calculations in the off-resonant region should not play a significant role. The overall good agreement between our results and the experiments for β- and α-Ga_2O_3 can be considered as an indication for the accuracy of the approximations used in this calculation.

Beyond the present approach, the inclusion of excitonic effects in the calculation of the frequency-dependent dielectric tensor could be an interesting topic of further investigations. Possible approaches are solving the Bethe-Salpeter equation or using the time-dependent density-functional theory including an exchange-correlation kernel that captures excitonic effects [69]. Then, the impact of excitons on the Raman tensors of Ga_2O_3 in the resonant region can be examined. These investigations can be important for a fundamental understanding of this material, since excitonic effects were shown to be very strong in the vicinity of the absorption edge [66, 67, 48]. However, the high computational costs of these approaches have to be taken into account.

The results of this work can also be considered as a starting point for studying the effects of doping, impurities, and defects in Ga_2O_3. The first-principles investigation of these effects on the vibrational and optical properties, and, therefore, the Raman spectra poses several challenges, *e.g.*, related to the treatment of charged systems and/or arising from the complexity and size of the unit cells which are required in these cases.

A. exciting input and species files

A.1 Input files

Input file for a ground-state relaxation

```
<input>
  <title>Ga2O3 beta phase prim cell optimized</title>
  <structure speciespath="~/species">
    <crystal>
    <basevect>   0.00000000      11.62094001    -2.88079323 </basevect>
    <basevect>   0.00000000      11.62094001     2.88079323 </basevect>
    <basevect>  10.67952905      -2.604670354    0.00000000 </basevect>
    </crystal>
    <species speciesfile="Ga.xml" rmt="1.7500">
      <atom coord="-0.65808000   0.34192000   0.68559000 "/>
      <atom coord="-0.34192000   0.65808000   0.31441000 "/>
      <atom coord="-0.90984000   0.09016000   0.79492000 "/>
      <atom coord="-0.09016000   0.90984000   0.20508000 "/>
    </species>
    <species speciesfile="O.xml" rmt="1.5000">
      <atom coord="-0.82656000   0.17344000   0.56411000 "/>
      <atom coord="-0.17344000   0.82656000   0.43589000 "/>
      <atom coord="-0.83671000   0.16329000   0.10955000 "/>
      <atom coord="-0.16329000   0.83671000   0.89045000 "/>
      <atom coord="-0.50426000   0.49574000   0.25595000 "/>
      <atom coord="-0.49574000   0.50426000   0.74405000 "/>
    </species>
  </structure>
  <groundstate xctype="GGA_PBE_SOL" maxscl="50" gmaxvr="20.0"
               ngridk="6 6 6" rgkmax="9.0" tforce="true">
  </groundstate>
  <relax endbfgs="stop" maxbfgs="20" taubfgs="5.0" history="true"/>
</input>
```

Input file for a Γ-phonon calculation

```
<input>
  <title>Ga2O3 beta phase Gamma phonons</title>
  <structure speciespath="~/species">
    <crystal>
    <basevect>   0.00000000      11.62094001     -2.88079323 </basevect>
    <basevect>   0.00000000      11.62094001      2.88079323 </basevect>
    <basevect>  10.67952905      -2.604670354     0.00000000 </basevect>
    </crystal>
    <species speciesfile="Ga.xml" rmt="1.7500">
      <atom coord="-0.65808000 0.34192000 0.68559000 "/>
      <atom coord="-0.34192000 0.65808000 0.31441000 "/>
      <atom coord="-0.90984000 0.09016000 0.79492000 "/>
      <atom coord="-0.09016000 0.90984000 0.20508000 "/>
    </species>
    <species speciesfile="O.xml" rmt="1.5000">
      <atom coord="-0.82656000 0.17344000 0.56411000 "/>
      <atom coord="-0.17344000 0.82656000 0.43589000 "/>
      <atom coord="-0.83671000 0.16329000 0.10955000 "/>
      <atom coord="-0.16329000 0.83671000 0.89045000 "/>
      <atom coord="-0.50426000 0.49574000 0.25595000 "/>
      <atom coord="-0.49574000 0.50426000 0.74405000 "/>
    </species>
  </structure>
  <groundstate xctype="GGA_PBE_SOL" maxscl="50" gmaxvr="20.0"
               ngridk="6 6 6" rgkmax="9.0" tforce="true">
  </groundstate>
  <phonons do="skip" ngridq="1 1 1">
      <qpointset>
         <qpoint> 0.0  0.0  0.0 </qpoint>
      </qpointset>
      <reformatdynmat/>
  </phonons>
</input>
```

Input file for a TDDFT calculation

```
<input>
  <title>Beta-Ga2O3, TDDFT </title>
  <structure speciespath="~/species">
    <crystal>
    <basevect>   0.00000000      11.62094001    -2.88079323 </basevect>
    <basevect>   0.00000000      11.62094001     2.88079323 </basevect>
    <basevect>  10.67952905      -2.604670354    0.00000000 </basevect>
    </crystal>
    <species speciesfile="Ga.xml" rmt="1.7500">
      <atom coord="-0.65808000   0.34192000   0.68559000 "/>
      <atom coord="-0.34192000   0.65808000   0.31441000 "/>
      <atom coord="-0.90984000   0.09016000   0.79492000 "/>
      <atom coord="-0.09016000   0.90984000   0.20508000 "/>
    </species>
    <species speciesfile="O.xml" rmt="1.5000">
      <atom coord="-0.82656000   0.17344000   0.56411000 "/>
      <atom coord="-0.17344000   0.82656000   0.43589000 "/>
      <atom coord="-0.83671000   0.16329000   0.10955000 "/>
      <atom coord="-0.16329000   0.83671000   0.89045000 "/>
      <atom coord="-0.50426000   0.49574000   0.25595000 "/>
      <atom coord="-0.49574000   0.50426000   0.74405000 "/>
    </species>
  </structure>
  <groundstate xctype="GGA_PBE_SOL" maxscl="50" gmaxvr="20.0"
               ngridk="6 6 6" rgkmax="9.0" tforce="true">
  </groundstate>
  <xs xstype="TDDFT"  ngridk="8 8 8"  vkloff="0.0625 0.1875 0.3125"
      ngridq="8 8 8"  rgkmax="7.0"  nempty="65"  gqmax="3.0"
      broad="0.001837"  scissor="0.0957" tevout="true"  nosym="true"
      dfoffdiag="true">
      <energywindow  intv="0.0 0.5"  points="1000"/>
      <tddft  fxctype="RPA"/>
      <qpointset>
         <qpoint>0.0  0.0  0.0</qpoint>
      </qpointset>
  </xs>
</input>
```

Input file for a BSE calculation

```
<input>
  <title>Beta-Ga2O3, BSE</title>
  <structure speciespath="~/species">
    <crystal>
    <basevect>   0.00000000      11.62094001     -2.88079323 </basevect>
    <basevect>   0.00000000      11.62094001      2.88079323 </basevect>
    <basevect>  10.67952905      -2.604670354     0.00000000 </basevect>
    </crystal>
    <species speciesfile="Ga.xml" rmt="1.7500">
      <atom coord="-0.65808000 0.34192000 0.68559000 "/>
      <atom coord="-0.34192000 0.65808000 0.31441000 "/>
      <atom coord="-0.90984000 0.09016000 0.79492000 "/>
      <atom coord="-0.09016000 0.90984000 0.20508000 "/>
    </species>
    <species speciesfile="O.xml" rmt="1.5000">
      <atom coord="-0.82656000 0.17344000 0.56411000 "/>
      <atom coord="-0.17344000 0.82656000 0.43589000 "/>
      <atom coord="-0.83671000 0.16329000 0.10955000 "/>
      <atom coord="-0.16329000 0.83671000 0.89045000 "/>
      <atom coord="-0.50426000 0.49574000 0.25595000 "/>
      <atom coord="-0.49574000 0.50426000 0.74405000 "/>
    </species>
  </structure>
  <groundstate xctype="GGA_PBE_SOL" maxscl="50" gmaxvr="20.0"
               ngridk="6 6 6" rgkmax="9.0" tforce="true">
  </groundstate>
  <xs xstype="BSE"  ngridk="8 8 8"  vkloff="0.0625 0.1875 0.3125"
      ngridq="8 8 8"  rgkmax="7.0"  nempty="100"  gqmax="1.0"
      broad="0.001837"  scissor="0.0957"  tevout="true"
      nosym="true"  dfoffdiag="true">
      <energywindow  intv="0.0 0.5"  points="1000"/>
      <screening screentype="full"/>
      <BSE  bsetype="singlet"  nstlbse="51 60 1 2"/>
      <qpointset>
          <qpoint>0.0  0.0  0.0</qpoint>
      </qpointset>
  </xs>
</input>
```

Input file for a Raman-scattering calculation

```
<input>
  <title>Beta-Ga2O3, Raman-calculation</title>
  <structure speciespath="~/species">
    <crystal>
    <basevect>   0.00000000      11.62094001    -2.88079323 </basevect>
    <basevect>   0.00000000      11.62094001     2.88079323 </basevect>
    <basevect>  10.67952905      -2.604670354    0.00000000 </basevect>
    </crystal>
    <species speciesfile="Ga.xml" rmt="1.7500">
      <atom coord="-0.65808000  0.34192000  0.68559000 "/>
      <atom coord="-0.34192000  0.65808000  0.31441000 "/>
      <atom coord="-0.90984000  0.09016000  0.79492000 "/>
      <atom coord="-0.09016000  0.90984000  0.20508000 "/>
    </species>
    <species speciesfile="O.xml" rmt="1.5000">
      <atom coord="-0.82656000  0.17344000  0.56411000 "/>
      <atom coord="-0.17344000  0.82656000  0.43589000 "/>
      <atom coord="-0.83671000  0.16329000  0.10955000 "/>
      <atom coord="-0.16329000  0.83671000  0.89045000 "/>
      <atom coord="-0.50426000  0.49574000  0.25595000 "/>
      <atom coord="-0.49574000  0.50426000  0.74405000 "/>
    </species>
  </structure>
  <groundstate xctype="GGA_PBE_SOL" maxscl="50" gmaxvr="20.0"
               ngridk="6 6 6" rgkmax="9.0" tforce="true">
  </groundstate>
  <properties>
      <raman getphonon="fromfile" mode="30" nstep="5" displ="0.01"
         degree="2" elaser="2.33" elaserunit="eV" temp="298.15" broad="3.0">
         <energywindow intv="0.0 0.006" points="4000" />
      </raman>
  </properties>
  <xs xstype="TDDFT"  ngridk="8 8 8"  vkloff="0.0625 0.1875 0.3125"
      ngridq="8 8 8"  rgkmax="7.0"  nempty="65"  gqmax="3.0"
      broad="0.001837"  scissor="0.0957" tevout="true"  nosym="true"
      dfoffdiag="true">
      <energywindow  intv="0.0 0.5"  points="1000"/>
      <tddft  fxctype="RPA"/>
      <qpointset>
         <qpoint>0.0  0.0  0.0</qpoint>
      </qpointset>
  </xs>
</input>
```

A.2 Species files

A.2.1 β phase

Species file for the element gallium

```
<?xml version="1.0" encoding="UTF-8"?>
<spdb xsi:noNamespaceSchemaLocation="../../xml/species.xsd"
      xmlns:xsi="http://www.w3.org/2001/XMLSchema-instance">
  <sp chemicalSymbol="Ga" name="gallium" z="-31.0000" mass="127097.2538">
    <muffinTin rmin="0.100000E-04" radius="1.9000"
               rinf="28.4824" radialmeshPoints="400"/>
    <atomicState n="1" l="0" kappa="1" occ="2.00000" core="true"/>
    <atomicState n="2" l="0" kappa="1" occ="2.00000" core="true"/>
    <atomicState n="2" l="1" kappa="1" occ="2.00000" core="true"/>
    <atomicState n="2" l="1" kappa="2" occ="4.00000" core="true"/>
    <atomicState n="3" l="0" kappa="1" occ="2.00000" core="false"/>
    <atomicState n="3" l="1" kappa="1" occ="2.00000" core="false"/>
    <atomicState n="3" l="1" kappa="2" occ="4.00000" core="false"/>
    <atomicState n="3" l="2" kappa="2" occ="4.00000" core="false"/>
    <atomicState n="3" l="2" kappa="3" occ="6.00000" core="false"/>
    <atomicState n="4" l="0" kappa="1" occ="2.00000" core="false"/>
    <atomicState n="4" l="1" kappa="1" occ="1.00000" core="false"/>
    <basis>
      <default type="lapw" trialEnergy="0.1500" searchE="false"/>
      <custom l="0" type="apw+lo" trialEnergy="0.1500" searchE="false"/>
      <lo l="0">
        <wf matchingOrder="0" trialEnergy="0.1500" searchE="false"/>
        <wf matchingOrder="0" trialEnergy="-5.02" searchE="false"/>
      </lo>
      <lo l="0">
        <wf matchingOrder="0" trialEnergy="-5.02" searchE="false"/>
        <wf matchingOrder="1" trialEnergy="-5.02" searchE="false"/>
      </lo>
      <custom l="1" type="apw+lo" trialEnergy="0.1500" searchE="false"/>
      <lo l="1">
        <wf matchingOrder="0" trialEnergy="0.1500" searchE="false"/>
        <wf matchingOrder="0" trialEnergy="-3.20" searchE="false"/>
      </lo>
     <lo l="1">
        <wf matchingOrder="0" trialEnergy="-3.20" searchE="false"/>
        <wf matchingOrder="1" trialEnergy="-3.20" searchE="false"/>
      </lo>
      <custom l="2" type="apw+lo" trialEnergy="-0.30" searchE="false"/>
     <lo l="2">
        <wf matchingOrder="0" trialEnergy="-0.30" searchE="false"/>
        <wf matchingOrder="2" trialEnergy="-0.30" searchE="false"/>
      </lo>
    </basis>
  </sp>
</spdb>
```

Species file for the element oxygen

```
<?xml version="1.0" encoding="UTF-8"?>
<spdb xsi:noNamespaceSchemaLocation="../../xml/species.xsd"
      xmlns:xsi="http://www.w3.org/2001/XMLSchema-instance">
  <sp chemicalSymbol="O" name="oxygen" z="-8.00000" mass="29165.12203">
    <muffinTin rmin="0.100000E-04" radius="1.5000"
               rinf="17.0873" radialmeshPoints="300"/>
    <atomicState n="1" l="0" kappa="1" occ="2.00000" core="true"/>
    <atomicState n="2" l="0" kappa="1" occ="2.00000" core="false"/>
    <atomicState n="2" l="1" kappa="1" occ="2.00000" core="false"/>
    <atomicState n="2" l="1" kappa="2" occ="2.00000" core="false"/>
    <basis>
      <default type="lapw" trialEnergy="0.1500" searchE="false"/>
      <custom l="0" type="apw+lo" trialEnergy="-0.50" searchE="false"/>
      <lo l="0">
        <wf matchingOrder="0" trialEnergy="-0.50" searchE="false"/>
        <wf matchingOrder="2" trialEnergy="-0.50" searchE="false"/>
      </lo>
      <custom l="1" type="apw+lo" trialEnergy="0.1500" searchE="false"/>
      <lo l="1">
        <wf matchingOrder="0" trialEnergy="0.1500" searchE="false"/>
        <wf matchingOrder="2" trialEnergy="0.1500" searchE="false"/>
      </lo>
      <custom l="2" type="apw+lo" trialEnergy="0.1500" searchE="false"/>
      <lo l="2">
        <wf matchingOrder="0" trialEnergy="0.1500" searchE="false"/>
        <wf matchingOrder="2" trialEnergy="0.1500" searchE="false"/>
      </lo>
    </basis>
  </sp>
</spdb>
```

A.2.2 α phase

Species file for the element gallium

```
<?xml version="1.0" encoding="UTF-8"?>
<spdb xsi:noNamespaceSchemaLocation="../../xml/species.xsd"
      xmlns:xsi="http://www.w3.org/2001/XMLSchema-instance">
  <sp chemicalSymbol="Ga" name="gallium" z="-31.0000" mass="127097.2538">
    <muffinTin rmin="0.100000E-04" radius="1.9000"
               rinf="28.4824" radialmeshPoints="400"/>
    <atomicState n="1" l="0" kappa="1" occ="2.00000" core="true"/>
    <atomicState n="2" l="0" kappa="1" occ="2.00000" core="true"/>
    <atomicState n="2" l="1" kappa="1" occ="2.00000" core="true"/>
    <atomicState n="2" l="1" kappa="2" occ="4.00000" core="true"/>
    <atomicState n="3" l="0" kappa="1" occ="2.00000" core="false"/>
    <atomicState n="3" l="1" kappa="1" occ="2.00000" core="false"/>
    <atomicState n="3" l="1" kappa="2" occ="4.00000" core="false"/>
    <atomicState n="3" l="2" kappa="2" occ="4.00000" core="false"/>
    <atomicState n="3" l="2" kappa="3" occ="6.00000" core="false"/>
    <atomicState n="4" l="0" kappa="1" occ="2.00000" core="false"/>
    <atomicState n="4" l="1" kappa="1" occ="1.00000" core="false"/>
    <basis> <default type="lapw" trialEnergy="0.1500" searchE="false"/>
      <custom l="0" type="apw+lo" trialEnergy="0.15" searchE="false"/>
      <lo l="0">
        <wf matchingOrder="0" trialEnergy="0.15" searchE="false"/>
        <wf matchingOrder="2" trialEnergy="0.15" searchE="false"/>
      </lo>
      <lo l="0">
        <wf matchingOrder="0" trialEnergy="0.15" searchE="false"/>
        <wf matchingOrder="0" trialEnergy="-5.02" searchE="false"/>
      </lo>
      <custom l="1" type="apw+lo" trialEnergy="0.15" searchE="false"/>
      <lo l="1">
        <wf matchingOrder="0" trialEnergy="0.15" searchE="false"/>
        <wf matchingOrder="2" trialEnergy="0.15" searchE="false"/>
      </lo>
      <lo l="1">
        <wf matchingOrder="0" trialEnergy="0.15" searchE="false"/>
        <wf matchingOrder="0" trialEnergy="-3.20" searchE="false"/>
      </lo>
      <custom l="2" type="apw+lo" trialEnergy="-0.30" searchE="false"/>
      <lo l="2">
        <wf matchingOrder="0" trialEnergy="-0.30" searchE="false"/>
        <wf matchingOrder="2" trialEnergy="-0.30" searchE="false"/>
      </lo>
    </basis>
  </sp>
</spdb>
```

Species file for the element oxygen

```
<?xml version="1.0" encoding="UTF-8"?>
<spdb xsi:noNamespaceSchemaLocation="../../xml/species.xsd"
      xmlns:xsi="http://www.w3.org/2001/XMLSchema-instance">
  <sp chemicalSymbol="O" name="oxygen" z="-8.00000" mass="29165.12203">
    <muffinTin rmin="0.100000E-04" radius="1.5000"
               rinf="17.0873" radialmeshPoints="300"/>
    <atomicState n="1" l="0" kappa="1" occ="2.00000" core="true"/>
    <atomicState n="2" l="0" kappa="1" occ="2.00000" core="false"/>
    <atomicState n="2" l="1" kappa="1" occ="2.00000" core="false"/>
    <atomicState n="2" l="1" kappa="2" occ="2.00000" core="false"/>
    <basis>
      <default type="lapw" trialEnergy="0.1500" searchE="false"/>
      <custom l="0" type="apw+lo" trialEnergy="-0.50" searchE="false"/>
      <lo l="0">
        <wf matchingOrder="0" trialEnergy="-0.50" searchE="false"/>
        <wf matchingOrder="2" trialEnergy="-0.50" searchE="false"/>
      </lo>
      <custom l="1" type="apw+lo" trialEnergy="0.1500" searchE="false"/>
      <lo l="1">
        <wf matchingOrder="0" trialEnergy="0.15" searchE="false"/>
        <wf matchingOrder="2" trialEnergy="0.15" searchE="false"/>
      </lo>
    </basis>
  </sp>
</spdb>
```

B. Reference data for α-Ga_2O_3

B.1 Polarized Raman spectra

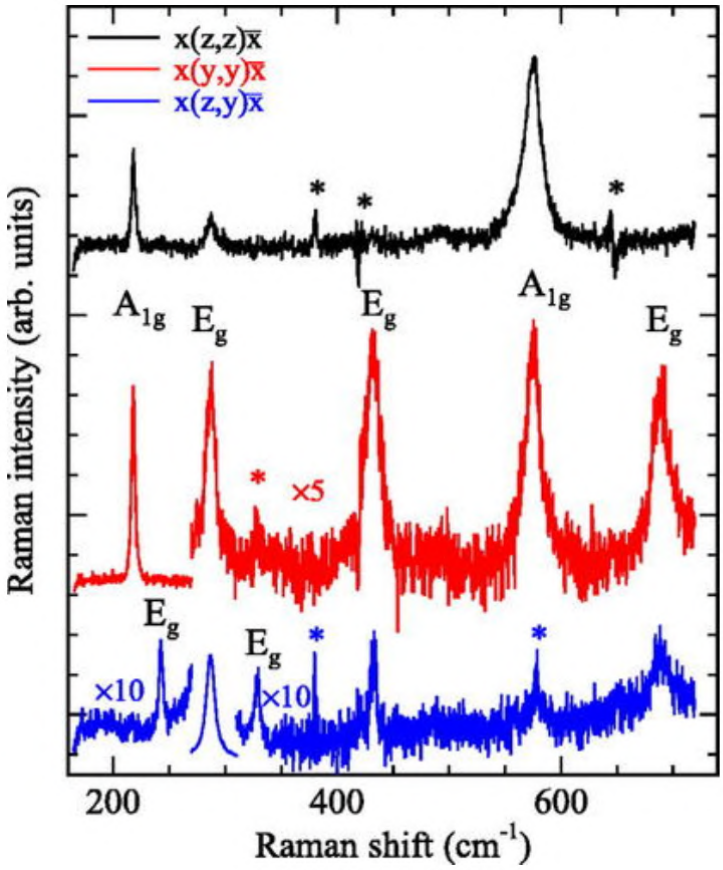

FIGURE B.1: Polarized Raman spectra for the (yy), (zz), and (zy) polarization [31].

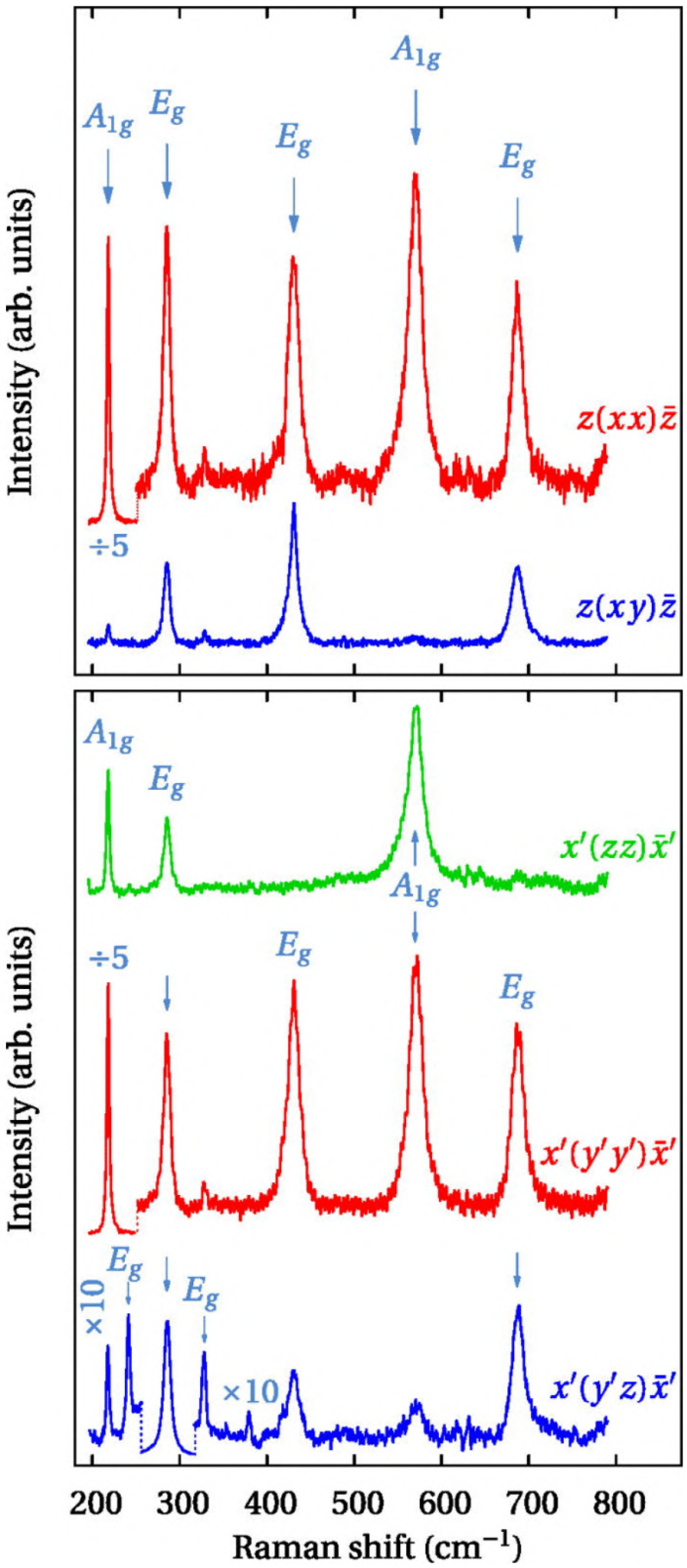

FIGURE B.2: Polarized Raman spectra for the (xx) and (xy) (top) and (zz), (y′y′), and (y′z) (bottom) polarization. Due to the choice of x′ and y′ in the experimental setup, these spectra correspond to our (yy) polarization (same for (y′z)). The figures are taken from Ref. [23] and edited for the sake of clarity.

B. Bibliography

[1] M. Grundmann et al. "Transparent semiconducting oxides: Materials and devices". In: *Physica status solidi (a)* 207.6 (2010), pp. 1437–1449.

[2] J. F. Wager, D. A. Keszler, and R. E. Presley. *Transparent electronics*. Vol. 112. Springer, 2008.

[3] H. Kumomi et al. "Materials, devices, and circuits of transparent amorphous-oxide semiconductor". In: *Journal of Display Technology* 5.12 (2009), pp. 531–540.

[4] P. Wellenius et al. "An amorphous indium–gallium–zinc–oxide active matrix electroluminescent pixel". In: *Journal of display technology* 5.12 (2009), pp. 438–445.

[5] T. Riedl, P. Gorrn, and W. Kowalsky. "Transparent electronics for see-through AMOLED displays". In: *Journal of Display Technology* 5.12 (2009), pp. 501–508.

[6] C Guillén and J Herrero. "TCO/metal/TCO structures for energy and flexible electronics". In: *Thin Solid Films* 520.1 (2011), pp. 1–17.

[7] S. Cui et al. "Room-Temperature Fabricated Amorphous Ga2O3 High-Response-Speed Solar-Blind Photodetector on Rigid and Flexible Substrates". In: *Advanced Optical Materials* 5.19 (2017), p. 1700454.

[8] Z. Galazka et al. "On the bulk β-Ga_2O_3single crystals grown by the Czochralski method". In: *Journal of Crystal Growth* 404 (2014), pp. 184–191.

[9] Z Galazka et al. "Czochralski growth and characterization of β-Ga_2O_3single crystals". In: *Crystal Research and Technology* 45.12 (2010), pp. 1229–1236.

[10] S. R. Thomas et al. "High electron mobility thin-film transistors based on Ga_2O_3 grown by atmospheric ultrasonic spray pyrolysis at low temperatures". In: *Applied Physics Letters* 105.9 (2014), p. 092105.

[11] M. Higashiwaki et al. "Gallium oxide (Ga_2O_3) metal-semiconductor field-effect transistors on single-crystal β-Ga_2O_3(010) substrates". In: *Applied Physics Letters* 100.1 (2012), p. 013504.

[12] S. Ohira et al. "Fabrication of hexagonal GaN on the surface of β-Ga_2O_3 single crystal by nitridation with NH3". In: *Thin Solid Films* 496.1 (2006), pp. 53–57.

[13] K. Matsuzaki et al. "Growth, structure and carrier transport properties of Ga_2O_3 epitaxial film examined for transparent field-effect transistor". In: *Thin solid films* 496.1 (2006), pp. 37–41.

[14] K. Zeng, A. Vaidya, and U. Singisetti. "1.85 kV breakdown voltage in lateral field-plated Ga_2O_3 MOSFETs". In: *IEEE Electron Device Letters* 39.9 (2018), pp. 1385–1388.

[15] F Ren et al. "Demonstration of enhancement-mode p-and n-channel GaAs MOSFETs with Ga_2O_3 (Gd_2O_3) as gate oxide". In: *Solid-State Electronics* 41.11 (1997), pp. 1751–1753.

[16] M. H. Wong et al. "Field-plated Ga_2O_3 MOSFETs with a breakdown voltage of over 750 V". In: *IEEE Electron Device Letters* 37.2 (2015), pp. 212–215.

[17] M. Higashiwaki et al. "Recent progress in Ga_2O_3 power devices". In: *Semiconductor Science and Technology* 31.3 (2016), p. 034001.

[18] K. Sasaki et al. "Ga_2O_3 Schottky Barrier Diodes Fabricated by Using Single-Crystal *beta*-Ga_2O_3(010) Substrates". In: *IEEE electron device letters* 34.4 (2013), pp. 493–495.

[19] S. Pearton et al. "A review of Ga2O3 materials, processing, and devices". In: *Applied Physics Reviews* 5.1 (2018), p. 011301.

[20] R. Roy, V. Hill, and E. Osborn. "Polymorphism of Ga_2O_3 and the system $Ga_2O_3H_2O$". In: *Journal of the American Chemical Society* 74.3 (1952), pp. 719–722.

[21] S. Yoshioka et al. "Structures and energetics of Ga_2O_3 polymorphs". In: *Journal of Physics: Condensed Matter* 19.34 (2007), p. 346211.

[22] D. Machon et al. "High-pressure study of the β-to-α transition in Ga_2O_3". In: *Physical Review B* 73.9 (2006), p. 094125.

[23] R. Cuscó et al. "Lattice dynamics of a mist-chemical vapor deposition-grown corundum-like Ga_2O_3 single crystal". In: *Journal of Applied Physics* 117.18 (2015), p. 185706.

[24] M. Feneberg et al. "Ordinary dielectric function of corundumlike α-Ga_2O_3 from 40 meV to 20 eV". In: *Physical Review Materials* 2.4 (2018), p. 044601.

[25] J Furthmüller and F Bechstedt. "Quasiparticle bands and spectra of Ga_2O_3 polymorphs". In: *Physical Review B* 93.11 (2016), p. 115204.

[26] Y. Wang et al. "Properties and photocatalytic activity of β-Ga 2 O 3 nanorods under simulated solar irradiation". In: *Journal of Nanomaterials* 16.1 (2015), p. 126.

[27] M. Cardona and R. Merlin. *Light scattering in solids IX*. Springer, 2006, pp. 1–14.

[28] C. Kranert et al. "Raman tensor elements of β-Ga_2O_3". In: *Scientific reports* 6 (2016), p. 35964.

[29] T Onuma et al. "Polarized Raman spectra in β-Ga2O3 single crystals". In: *Journal of Crystal Growth* 401 (2014), pp. 330–333.

[30] D Dohy, G Lucazeau, and A Revcolevschi. "Raman spectra and valence force field of single-crystalline β Ga_2O_3". In: *Journal of Solid State Chemistry* 45.2 (1982), pp. 180–192.

[31] M. Feneberg et al. "Anisotropic phonon properties and effective electron mass in α-Ga_2O_3". In: *Applied Physics Letters* 114.14 (2019), p. 142102.

[32] A. Gulans et al. "exciting: a full-potential all-electron package implementing density-functional theory and many-body perturbation theory". In: *Journal of Physics: Condensed Matter* 26.36 (2014), p. 363202.

[33] P. Y. Yu and M. Cardona. *Fundamentals of semiconductors: physics and materials properties*. Springer, 2010.

[34] C. Ambrosch-Draxl et al. "Raman scattering in $YBa_2Cu_3O_7$: A comprehensive theoretical study in comparison with experiments". In: *Phys. Rev. B* 65 (6 2002), p. 064501. DOI: 10.1103/PhysRevB.65.064501.

[35] A. C. Ferrari and D. M. Basko. "Raman spectroscopy as a versatile tool for studying the properties of graphene". In: *Nature nanotechnology* 8.4 (2013), p. 235.

[36] C Ambrosch-Draxl, R Abt, and P Knoll. "Raman Scattering of Atomic Vibrations In Anharmonic Potentials". In: (1995).

[37] G. Czycholl. *Theoretische Festkörperphysik: von den klassischen Modellen zu modernen Forschungsthemen*. Springer-Verlag, 2007.

[38] P. Hohenberg and W. Kohn. "Inhomogeneous electron gas". In: *Physical review* 136.3B (1964), B864.

[39] W. Kohn and L. J. Sham. "Self-consistent equations including exchange and correlation effects". In: *Physical review* 140.4A (1965), A1133.

[40] J. P. Perdew et al. "Restoring the density-gradient expansion for exchange in solids and surfaces". In: *Physical review letters* 100.13 (2008), p. 136406.

[41] M. Born and K. Huang. *Dynamical theory of crystal lattices*. Clarendon press, 1954.

[42] X. Gonze and C. Lee. "Dynamical matrices, Born effective charges, dielectric permittivity tensors, and interatomic force constants from density-functional perturbation theory". In: *Physical Review B* 55.16 (1997), p. 10355.

[43] S. Sagmeister and C. Ambrosch-Draxl. "Time-dependent density functional theory versus Bethe–Salpeter equation: an all-electron study". In: *Physical Chemistry Chemical Physics* 11.22 (2009), pp. 4451–4457.

[44] E. Runge and E. K. Gross. "Density-functional theory for time-dependent systems". In: *Physical Review Letters* 52.12 (1984), p. 997.

[45] W. Nolting. *Grundkurs Theoretische Physik 7: Viel-Teilchen-Theorie*. Springer-Verlag, 2014.

[46] L. Hedin. "New method for calculating the one-particle Green's function with application to the electron-gas problem". In: *Physical Review* 139.3A (1965), A796.

[47] C. Cocchi. "Many-body perturbation theory for electronic structure methods". In: **University Lecture**, 2018/2019.

[48] F. Bechstedt and J. Furthmüller. "Influence of screening dynamics on excitons in Ga_2O_3 polymorphs". In: *Applied Physics Letters* 114.12 (2019), p. 122101.

[49] C. Draxl, D. Nabok, and K. Hannewald. "Organic/inorganic hybrid materials: Challenges for ab initio methodology". In: *Accounts of chemical research* 47.11 (2014), pp. 3225–3232.

[50] M Marezio and J. Remeika. "Bond Lengths in the α-Ga_2O_3 Structure and the High-Pressure Phase of Ga_2-xFe_xO_3". In: *The Journal of Chemical Physics* 46.5 (1967), pp. 1862–1865.

[51] R. Waldenfels et al. "In preparation".

[52] F Litimein et al. "FPLAPW study of the structural, electronic, and optical properties of Ga2O3: Monoclinic and hexagonal phases". In: *Journal of Alloys and Compounds* 488.1 (2009), pp. 148–156.

[53] J. L. Lyons. "Electronic Properties of Ga2O3 Polymorphs". In: *ECS Journal of Solid State Science and Technology* 8.7 (2019), Q3226–Q3228.

[54] J. Åhman, G. Svensson, and J. Albertsson. "A reinvestigation of β-gallium oxide". In: *Acta Crystallographica Section C: Crystal Structure Communications* 52.6 (1996), pp. 1336–1338.

[55] B. Liu, M. Gu, and X. Liu. "Lattice dynamical, dielectric, and thermodynamic properties of β-Ga_2O_3 from first principles". In: *Applied Physics Letters* 91.17 (2007), p. 172102.

[56] K. Yamaguchi. "First principles study on electronic structure of β-Ga_2O_3". In: *Solid state communications* 131.12 (2004), pp. 739–744.

[57] M. S. Dresselhaus, G. Dresselhaus, and A. Jorio. *Group theory: application to the physics of condensed matter*. Springer Science & Business Media, 2007.

[58] K. Mengle and E Kioupakis. "Vibrational and electron-phonon coupling properties of β-Ga_2O_3 from first-principles calculations: Impact on the mobility and breakdown field". In: *AIP Advances* 9.1 (2019), p. 015313.

[59] M. Schubert et al. "Anisotropy, phonon modes, and free charge carrier parameters in monoclinic β-gallium oxide single crystals". In: *Physical Review B* 93.12 (2016), p. 125209.

[60] S. Tillack. "private communication".

[61] R. Resta and D. Vanderbilt. *Theory of Polarization: A Modern Approach (in Physics of Ferroelectrics A Modern Perspective)*. Topics in Applied Physics Volume 105, 2007.

[62] E. Víllora et al. "Infrared Reflectance and Electrical Conductivity of β-Ga_2O_3". In: *physica status solidi (a)* 193.1 (2002), pp. 187–195.

[63] M Rebien et al. "Optical properties of gallium oxide thin films". In: *Applied physics letters* 81.2 (2002), pp. 250–252.

[64] J. B. Varley and A. Schleife. "Bethe-Salpeter calculation of optical-absorption spectra of In_2O_3 and Ga_2O_3". In: *Semiconductor Science and Technology* 30.2 (2015), p. 024010.

[65] H. He et al. "First-principles study of the structural, electronic, and optical properties of Ga_2O_3 in its monoclinic and hexagonal phases". In: *Physical Review B* 74.19 (2006), p. 195123.

[66] A. Mock et al. "Band-to-band transitions, selection rules, effective mass, and excitonic contributions in monoclinic β- Ga_2O_3". In: *Physical Review B* 96.24 (2017), p. 245205.

[67] C. Sturm et al. "Dielectric tensor of monoclinic Ga_2O_3 single crystals in the spectral range 0.5-8.5 eV". In: *APL Materials* 3.10 (2015), p. 106106.

[68] L. Maschio et al. "Ab initio analytical Raman intensities for periodic systems through a coupled perturbed Hartree-Fock/Kohn-Sham method in an atomic orbital basis. I. Theory". In: *The Journal of chemical physics* 139.16 (2013), p. 164101.

[69] A. Marini, R. Del Sole, and A. Rubio. "Bound excitons in time-dependent density-functional theory: Optical and energy-loss spectra". In: *Physical review letters* 91.25 (2003), p. 256402.